ISSN 0915-633X

NATIONAL INSTITUTE FOR FUSION SCIENCE

Contributions to 28th European Physical Society Conference on Controlled Fusion and Plasma Physics (Madeira Tecnopolo, Funchal, Portugal, 18-22 June 2001) from LHD Experiment

LHD Experimental Group

(Received - July 18, 2001)

NIFS-709 July 2001

RESEARCH REPORT
NIFS Series

TOKI, JAPAN

Contributions to 28th European Physical Society Conference on Controlled Fusion and Plasma Physics (Madeira Tecnopolo, Funchal, Portugal, 18-22 June 2001) from LHD experiment

LHD Experimental Group

Abstract

The LHD experimental group has presented nineteen papers at the 28th European Physical Society Conference on Controlled Fusion and Plasma Physics (Madeira Tecnopolo, Funchal, Portugal, 18-22 June 2001). The contributed papers are collected in this report.

IT.05 "Configuration flexibility and extended regimes in Large Helical Device" H.Yamada *et al.*
P1.107 "Pulsed radar refrectometer for density profile and fluctuation measurements of Large Helical Device" T.Tokuzawa *et al.*
P1.108 "Radial profile measurements of electron temperature and metallic impurity lines using X-ray pulse height analyzer in LHD" S.Muto *et al.*
P1.113 "A multichannel 118.8 micro m-CH3OH laser interferometer for electron density profile measurements in LHD" K. Kawahata *et al.*
P2.094 "High Power ICRF Heating in LHD in the 4th Campaign" T.Watari *et al.*
P3.100 "Bolometric imaging of radiative structures on LHD" N.Ashikawa *et al.*
P3.102 "Tangential Polarimeter for Electron Density Diagnostics on LHD" T.Akiyama *et al.*
P4.041 "Impurity behavior in LHD long pulse discharges" Y. Nakamura *et al.*
P4.042 "Measurement of Shafranov shift with soft x-ray CCD camera on LHD"
Y. Liang *et al.*
P4.043 "Effective charge dependence of confinement improvement factor in LHD" J.Miyazawa *et al.*
P4.044 "Role of changing transport in "breathing" oscillations in LHD" B.J. Peterson *et al.*
P4.045 "5-D simulation study of energetic tail ion transport during ICRF heating in LHD" S. Murakami *et al.*
P4.046 "Investigation of symmetric thermal decay and asymmetric radiative collapse of NBI heated plasma on LHD" Yuhong Xu *et al.*
P4.047 "Effect of magnetic islands on LHD plasma performance" A. Komori *et al.*
P4.048 "Confinement of fast ions produced by NBI on LHD" M.Osakabe *et al.*
P4.049 "Characteristics of reheat-mode discharges in Large Helical Device" S.Morita *et al.*
P4.050 "Characteristics of MHD instabilities excited in core and edge regions of the LHD Plasmas" K. Toi *et al.*
P4.051 "Low frequency oscillations induced by ice pellet injection on the Large Helical Device" S.Ohdachi *et al.*
P4.052 "Plasma and impurity transport modeling of NBI-heated LHD and helical reactor systems" K. Yamazaki *et al.*

Keywords : Large helical device, 28th European physical society conference on controlled fusion and plasma physics, 4th experimental campaign, contributed papers

Configuration Flexibility and Extended Regimes in Large Helical Device

H.Yamada, A.Komori, N.Ohyabu, O.Kaneko, K.Kawahata, K.Y.Watanabe, S.Sakakibara, S.Murakami, K.Ida, R.Sakamoto, Y.Liang, J.Miyazawa, K.Tanaka, Y.Narushima, S.Morita, S.Masuzaki, T.Morisaki, N.Ashikawa[1], L.R.Baylor[3], W.A. Cooper[5], M.Emoto, P.W.Fisher[3], H.Funaba, M.Goto, H.Idei, K.Ikeda, S.Inagaki, N.Inoue, M.Isobe, K.Khlopenkov, T.Kobuchi[1], A.Kostrioukov, S.Kubo, T. Kuroda, R.Kumazawa, T.Minami, S.Muto, T.Mutoh, Y.Nagayama, N.Nakajima, Y.Nakamura, H.Nakanishi, K.Narihara, K.Nishimura, N.Noda, T.Notake[2], S.Ohdachi, Y.Oka, M.Osakabe, T.Ozaki, B.J.Peterson, G.Rewoldt[4], A.Sagara, K.Saito[2], H.Sasao[1], M.Sasao, K.Sato, M.Sato, T.Seki, H.Sugama, T.Shimozuma, M.Shoji, H.Suzuki, Y.Takeiri, N.Tamura[1], K.Toi, T.Tokuzawa, Y.Torii[2], K.Tsumori, T.Watanabe, I.Yamada, S.Yamamoto[2], M.Yokoyama, Y.Yoshimura, T.Watari, Y.Xu, K.Itoh, K.Matsuoka, K.Ohkubo, T.Satow, S.Sudo, T.Uda, K.Yamazaki, O.Motojima, M.Fujiwara

National Institute for Fusion Science, Toki, Gifu 509-5292, Japan
1 Department of Fusion Science, School of Mathematical and Physical Science,
Graduate University for Advanced Studies, Hayama, 240-0193, Japan
2 Department of Energy Engineering and Science, Nagoya University, 464-8603, Japan
3 Oak Ridge National Laboratory, Oak Ridge, TN 37831, USA
4 Princeton Plasma Physics Laboratory, Princeton, NJ 08544, USA
5 CRPP, Lausanne, Switzerland

Abstract

Recent experimental results in the Large Helical Device have indicated that a large pressure gradient can be formed beyond the stability criterion for the Mercier (high-*n*) mode. While stability against an interchange mode is violated in the inward shifted configuration due to enhancement of magnetic hill, in contrast neoclassical transport and confinement of high energetic particle are improved by this inward shift. Mitigation of the unfavorable effects of MHD instability has led to a significant extension of the operational regime. Achievements of the stored energy of 1 MJ and the volume averaged beta of 3 % are representative results from this finding. A confinement enhancement factor above the international stellarator scaling ISS95 is also maintained around 1.5 towards $\langle\beta\rangle$ of 3%. Configuration studies on confinement and MHD characteristics emphasize superiority of the inward shifted geometry to other geometries. The emergence of coherent modes looks consistent with the linear ideal MHD theory, however, the inward shifted configuration has reduced heat transport in spite of a larger amplitude of magnetic fluctuation than the outward shifted configuration. While neoclassical helical ripple transport becomes visible for the outward shifted configuration in the collisionless regime, the inward shifted configuration does not show degradation of confinement deep in the collisionless regime ($\nu^*<0.1$). Distinguished characteristics observed in the inward shifted configuration help to create a new perspective of MHD stability and related transport in net current-free plasmas. The first result of the pellet launching at different locations is also reported as a topic.

1. Introduction

The Large Helical Device (LHD) project [1] is aimed at clarification of physical mechanisms in net current-free plasmas close to reactor conditions and demonstration of the technology required for steady-state operation [2] by the heliotron concept [3]. The large dimensions of a nominal major radius *R* and a minor radius *a* of 3.9 m and 0.6 m, respectively, and the strong magnetic field (≈ 3 T) have extended the operational envelopes in non-dimensional physical parameters as well as in absolute values from the medium-sized helical experiments. Physics achievements have been steadily obtained along with the progress in heating power and reliable operation of the superconducting magnets [4-7]. The most important achievement to date is the outstanding management of confinement with MHD stability. The magnetic configuration with the inward shifted magnetic axis had been considered to lie in an unfavorable regime for interchange instabilities due to a prominent magnetic hill [8] while the helical ripple structure is very favorable for fast ion confinement as well as mitigation of neoclassical transport [9]. Figure 1 schematizes the effect of magnetic axis position on MHD stability and transport. A Mercier-unstable region occupies a major region at the magnetic axis position R_{ax} of 3.6 m. While this analysis has been based on a model pressure profile, a local pressure gradient was supposed to be determined by a combination of MHD instability and related transport. Neoclassical transport is greatly mitigated by combination of multi-helicity [10] and the theoretical model of ballooning/interchange mode turbulence also predicts a geometrical effect on anomalous transport [11,12]. A compromise between the MHD stability and transport, and suppression of unfavorable helical ripple transport in a collisionless regime have been the most important concerns in the recent experimental campaign in LHD. The experimental observation has indicated that the plasma in the inward shifted configuration represents neither any global destruction nor any significant degradation of confinement even in the Mercier unstable region although the resonant fluctuations emerge as expected from the ideal MHD theory [13]. The energy confinement in this inward shifted configuration has been proved to be 50 % larger than the international stellrator scaling 95 (ISS95) [14,15]. Consequently, two major achievements in performance have been obtained in the recent experimental campaign. The one is that the stored energy has exceeded 1 MJ and the other is that the volume averaged beta value $<\beta>$ has ranged to 3 %. The achieved maximum values in the experiment are summarized in Table 1. The primary interest in this study lies in the plasma performance in the extended regimes in high beta and low collisionality.

The LHD has configuration flexibility by tailoring poloidal magnetic field, which plays a role in scanning the magnetic axis position R_{ax} for 3.55 $\mathrm{m} \leq R_{ax} \leq 4.0$ m and the toroidally averaged ellipticity κ for $0.92 \leq \kappa \leq 1.17$. These configurational investigations highlight the effects of magnetic well and shear, the orbits of high-energetic particles, and neoclassical transport. The ellipticity which can be controlled by the quadrupole component of the poloidal field affects Pfirsh-Schlueter currents and the fraction of trapped particles.

In Section 2, geometrical effect on confinement is discussed with attention to dependence on collisionality and beta. Section 3 is devoted to the MHD characteristics and documentation of a high beta discharge. Pellet injection from different locations, which is the first trial in net current-free plasmas, is reported in Section 4. The topical recent experiments including extended stored energy are described in Section 5. Section 6 is allocated to conclusions.

3. Geometrical and finite-beta effect on confinement characteristics

A previous study on energy confinement in LHD has indicated that confinement improvement in the standard configuration with R_{ax}=3.75m over the medium-sized helitoron/torsatron is attributed to the significant contribution of high edge pressure and that the core confinement inside ρ=0.9 is comparable to the medium-size heliotron/torsatron [16]. It should be note that the LHD plasma in that study did not enter the collisionless regime deeply ($\nu^* \sim 1$). Here collisionality ν^* is defined by $\nu^* = \sqrt{2} Rq\nu_{ei} / v_{th}^{e} \varepsilon^{1.5}$ for electrons, and the ion collisionality is similar to this since generally $T_e \sim T_i$ in NBI heated plasmas. While the nature of the confinement in the case with R_{ax}=3.6 m is located between Bohm and gyro-Bohm, which is similar to that described in the ISS95 scaling, it has shown a further systematic improvement by a factor of 1.5-1.6 on the ISS95 scaling [15]. Although the anomaly of local electron heat conduction with respect to an estimate from neoclassical theory has been on the order of 10 to 100 in NBI heated plasmas in the past medium-sized experiments, the anomaly in LHD plasmas is reduced to the order of unity.

Neoclassical transport itself is of importance in the collisionless regime and its qualitative evaluation is also prerequisite to an investigation of anomalous transport. The helical ripple transport is enhanced in the collisionless regime in inverse proportion to ν^*, however, it can be controlled by tailoring multi-helicity [10]. As seen in Fig.1, the inward shifted configuration reduces the neoclassical transport by localizing helical ripples on the inboard side. A reduction of one order of magnitude is expected between the available configurations for R_{ax}= 3.55 m and R_{ax}= 4.0 m. Although the neoclassical transport exists invariably, it was not reflected by the data yielding the ISS95 scaling where plasmas are collisional and anomalous transport predominates confinement. In the present study, the plasmas which enter deep in the collisionless regime ($\nu^* << 1$) are investigated. The data have been taken from NBI heated plasmas at the quasi-steady state phase satisfying $\mathrm{d}W/\mathrm{d}t < 0.1 P_{abs}$.

Figure 2(a) shows the dependence of the confinement enhancement factor on collisionality. The ISS95 scaling itself does not have collisionality dependence like $\tau_E \Omega \propto \rho^{*-2.71} \nu^{*-0.04} \beta^{-0.16}$ where ρ^* and Ω are the normalized gyro radius and the ion gyro-fequency, respectively. The inward shifted configuration with $R_{ax} \leq 3.6$ m has no significant or even slight negative dependence on ν^* even in deep a collisionless regime. In contrast, the outward shifted configuration clearly shows declination in low collisionality. The data of the case with R_{ax} =3.6 m alone gives the scaling shows the density dependence $\tau_E \propto P_{abs}^{-0.60\pm0.01} \overline{n}_e^{0.47\pm0.02} B^{0.75\pm0.02}$ which is similar to the ISS95 scaling. Here P_{abs} $\overline{n}_e$,B are the absorbed heating power, the line averaged density, and the magnetic field strength, respectively. This expression can be rephrased in $\tau_E \Omega \propto \rho^{*-2.44\pm0.08} \nu^{*-0.12\pm0.02} \beta^{-0.04\pm0.05}$. Even if the data in the collisionless regime ($\nu^*<1$) are processed, this expression does not show any significant change: $\tau_E \Omega \propto \rho^{*-2.44\pm0.14} \nu^{*-0.13\pm0.08} \beta^{-0.03\pm0.09}$. As predicted from the tendency seen in Fig.2(a), the ν^* dependence comes out for the outward shifted configuration. The dependence $\tau_E \Omega \propto \nu^{*0.20\pm0.03}$ is obtained for $\nu^* < 2$ in the case with R_{ax}= 3.75 m and it becomes stronger for the case with R_{ax} = 3.9 m: $\tau_E \Omega \propto \nu^{*0.57\pm0.10}$. The local power balance analysis indicates that the neoclassical heat conduction is more than a half of the experimental value in the plasmas with $\nu^* \sim 1$ in the case with R_{ax}= 3.75 m [16]. Although clear views of quantitative estimate of neoclassical transport as well as accuracy of experimental measurements are not complete, the observed degradation of confinement in the collisionless regime which is enhanced in the outward shifted configuration may be attributed to a neoclassical helical ripple transport. In other words, no effect of neoclassical helical ripple transport has been observed and anomalous transport still dominates energy confinement in the inward shifted configuration down to $\nu^*<0.1$. The geometrical optimization for neoclassical helical ripple transport has been successfully demonstrated.

The next question is whether difference in neoclassical transport can explain superiority of the inward shifted configuration to the outward one or not. Certainly the neoclassical transport expands the gap between them in the collisionless regime. However, better confinement can be seen as well in the collisional regime where the helical ripple transport becomes small and an anomalous transport determines confinement. The example of reduce heat conduction will be shown in the later section (to appear in Table 3).

A finite beta effect on confinement, in particular, in the magnetic configuration with R_{ax}= 3.6 m is also a major issue since this geometry has unfavorable characteristics from the aspect of MHD stability and the outward Shafranov shift changes magnetic geometry. Although the MHD characteristics are discussed in the next section, the dependence of global energy confinement on beta is plotted in Fig.2(b) for the case with R_{ax}= 3.6 m. A systematic degradation has not been observed up to $<\beta>$ of 3 %. A time evolution of a single high beta discharge, which will be shown in the next section, also supports this feature.

The dependence of global confinement on the magnetic axis position has been surveyed while keeping an ellipticity of unity. The confinement enhancement over the ISS95 scaling with different magnetic axes is shown in Fig.3 (a). Performance of global confinement deteriorates monotonically from the inward shifted configuration to the outward shifted configuration. It should be noted that this trend is emphasized in the collisionless regime. Although the configuration with R_{ax}=3.55m is the best when the energy confinement time is normalized by ISS95, the configuration with R_{ax}=3.6m has the best performance in the absolute value because of 12 % larger volume than the case with R_{ax}=3.55m. Figure 3(b) shows the dependence of the confinement enhancement factor on the plasma ellpticity. Here the magnetic axis is fixed at 3.6 m. This geometry scan also supports the claim that the standard configuration with toroidal averaged circular cross-section has the best performance in absolute value as well as in a normalized evaluation.

There exist a hypothesis that the predominant transport mechanism is different in the core and the edge since the high edge temperature gradient [17,18] distinguishes LHD plasmas from the medium-sized experiments. The enhancement factor of a core confinement time derived from W_{core}/P_{abs} where $W_{core} = \int_{\rho=0}^{\rho=0.9} (p(\rho) - p(0.9))dV$ are also plotted in Fig.3. The dependence of the core confinement time on the magnetic geometry follows the trend of the entire confinement time in trend. This also means that the remainder, i.e., the pedestal part expediently defined by ρ=0.9 shows a dependence similar to those in the core and the entire treatment. However, a quantitative difference is observed depending on the configuration. As shown in Table 2, the ratio of the stored energy in the core to the total stored energy, W_{core}/W_{tot}, indicates that the core part for the case with R_{ax}=3.6m has a larger improvement than those in the cases of the outward shifted configurations. When the energy confinement is compared for the cases with R_{ax}= 3.6 m and 3.75 m, the case with R_{ax}= 3.6m shows enhancements of 1.48, 1.68, and 1.27 for the total, core and pedestal parts, respectively. Remarkable confinement improvement in the inward shifted configuration owes to the improvement in the core region and the improvement in the edge has less contribution. The dependence on an ellipticity shows that the vertically elongated configuration (k=1.17) has less contribution from the pedestal part, while no difference is observed between the cases with k=1.02 and 0.92.

3. High beta discharge and MHD characteristics

3.1 High beta discharge

A high beta attempt has been done in the configuration of R_{ax}=3.6m and κ=1.02 at low magnetic field of 0.5 T. Although the orbit loss of high energy ions from NBI (~150keV) is estimated to be several percent at more than 1 T from the Monte Carlo simulation code GNET [19], this loss is enhanced greatly by lowering the magnetic field even in this configuration with a good drift orbit. The magnetic field of 0.5 T is a tolerable limit of compromise between power deposition and an expected beta value.

Figure 4 (a) shows the waveforms of the discharge pushed to $<\beta>$ of 3.0%. The beta value increases to 2.6% along with the density ramp by gas puffing. Additional fueling is done by pellet injection at t=1.6 s. Although addiabatic condition is usually satisfied just at the pellet injection in higher temperature plasmas, a prompt energy loss is observed in this case. However, the energy recovers quickly and is raised to $<\beta>$ of 3% for a short time. Although the magnetic fluctuation measured apart from the outermost surface by 18 cm at the poloidal angle from the separatrix of 90 degrees reaches 0.1% of the equilibrium field when $<\beta>$ ranges to 3%, the energy confinement time normalized by the ISS95 scaling is maintained around 1.4 throughout the discharge. Coherent modes account for almost all the fluctuation amplitude. The m/n= 2/3 and 1/1 modes, the resonance surfaces of which exist near the plasma surface, are predominant when $<\beta> > 2.2\%$. In contrast, the $m/n = 2/1$ mode appears once when $<\beta> > 0.5\%$ and then disappears when $<\beta> > 2.2\%$.

Radiation collapse limits the operational density, subsequently the beta value. The critical density by the radiation collapse can be scaled empirically by $\bar{n}_c = C\sqrt{P_{abs}B/V}$, where V is the plasma volume in m^3 and the unit of $\bar{n}_c$ is $10^{19}m^{-3}$ [20] and the constant C lies between 1.1 and 1.5 [21] in LHD. The density at the $<\beta>$ of 3 % is $\bar{n}_e=2.5\times10^{19}$ m^{-3} which is close to the critical density $\bar{n}_c=2.4\text{-}3.3\times10^{19}m^{-3}$. The reason why the waveform of the stored energy is not very smooth and the enhancement factor is a little bit smaller than that of the regular performance may not be attributed to MHD instability but to enhancement of edge radiation.

A large Shafranov shift has been observed in a variety of diagnostics. Figure 4 (b) shows the temperature profile at $<\beta>$ of 3.0% projected onto the flux coordinate of the vacuum magnetic field. The shift has reached 40 % of the minor radius which still leaves margin to the equilibrium beta limit. It also can be pointed out in this figure that the temperature profile which is most sensitive to destruction of the magnetic surfaces keeps a smooth profile to the expected outermost surface. Although the fine structure at the plasma boundary should be investigated in detail, this observation supports the suitability of the definition of the plasma boundary by the vacuum surface, which is used in estimates of $<\beta>$.

3.2 Evolution of local pressure gradient

Since the heliotron configuration is characterized by freedom from net currents and magnetic hill, a concern for MHD instability is the pressure-driven interchange mode. Although the magnetic hill exists inevitably in the peripheral region, the stability against the ideal interchange mode is guaranteed by the strong magnetic shear. The interior region can be unstable due to loss of stabilization effect of the magnetic shear. This trend is highlighted in the configuration with the inward shifted magnetic axis which has enhanced magnetic hill.

Figure 5 shows the evolution of the pressure gradient at $\rho=0.5$ which roughly corresponds to the location of the $\iota\!\!\!-=1/2$ rational surface as a function of a volume averaged beta in the NBI heated plasmas with $R_{ax}=3.6$m. The Mercier unstable regime as well as the low-n mode unstable regime are also illustrated. The stability of low-n mode is calculated by the 3-dimensional MHD stability analysis code TERPSICHORE[22]. The remarkable point is that the pressure gradient larger than the Mercier criterion has been realized and that no major destruction has been observed to date. Also the pressure gradient seems to hesitate to increase further beyond $|d\beta/d\rho|=0.02\text{-}0.025$. This region is overlapped with an unstable region of the low-n ideal interchange mode. When a large pressure gradient deep in the low-n mode unstable region is formed temporally by pellet injection, minor relaxation phenomena have been sometimes observed [23] at a major rational surface. Many experimental points with quite low $|d\beta/d\rho|$ are seen around $<\beta>$ of 2% in Fig.5(a). These points correspond to occasional local flattening which suggests formation of an $m/n=2/1$ island [13]. The magnetic probes can identify the mode structure of a fluctuation with $m<10$. Observed magnetic fluctuation with a resonance of $\iota\!\!\!-=1/2$ is plotted in Fig.5(b). The amplitude of a resonant mode at $\iota\!\!\!-=1/2$ increases with beta and its evolution declines around the point corresponding to $|d\beta/d\rho|=0.02\text{-}0.025$ (see Fig.5(b)). The total beta value can develop further even with the hesitation of increase in the local pressure gradient. It should be also pointed out that there exists the threshold at $<\beta>=0.3\%$ in appearance of a coherent mode with $m/n=2/1$.

A time trace of the high beta discharge shown in Fig.4 indicates that the pressure gradient evolves roughly along with the envelope of a set of data up to $<\beta>$ of 2 %. The $m/n=2/1$ mode disappears above $<\beta>$ of 2.2 %. This plasma is supposed to enter the second stability regime against the interchange mode around $\rho=0.5$. If the pressure gradient is suppressed by the interchange mode, the pressure gradient should recover and grow further in the second stability regime. However, the experimental observation shows that the pressure gradient does not develop further. In addition to detailed investigation about stability, the transport and power deposition in this particular low magnetic field operation should be considered.

Regarding the edge point of $\rho=0.9$ which roughly corresponds to the $\iota\!\!\!-=1$ surface, both the local pressure gradient and the amplitude of coherent resonant mode evolve monotonically with $<\beta>$ as shown in Fig.6. Although this radius often has been discussed with relation to the generation of a magnetic island [18], the flattening has not been observed at low magnetic field operation within the spatial resolution of the Thomson scattering (~2.5cm). A larger pressure gradient than the Mercier criterion has been obtained here as well as in the case of $\rho=0.5$. A time trace of the high beta discharge shows that the plasma steps in the unstable region against the low-n mode instability. In contrast to the observation at $\rho=0.5$, a development of the local pressure gradient does not seem to be limited even in the low-n mode unstable region.

A monotonic increase in the local pressure gradient indicates that the observed fluctuation does not limit the local confinement. The magnetic fluctuation is detected from quite low $<\beta>$ and might be attributed to a resistive interchange mode on which a magnetic shear is not effective. Another interesting observation is that higher-n mode appears at lower $<\beta>$, which may reflect the characteristics of a pressure driven-mode that a higher-n mode has a larger growth rate.

Stability against the interchange mode is greatly improved in the configuration with R_{ax}=3.75m. Two comparisons of plasma parameters in the cases with R_{ax}=3.6m and 3.75m are described in Table 3. Both cases have approximately the same non-dimensional parameters, i.e., ρ^*,ν^* and $<\beta>$. The small pressure gradient at ρ=0.5 in the cases of 1.5 T is due to hollow density profile which may be attributed to neoclassical off-diagonal particle flux enhanced in a collisionless regime and not due to MHD instability. Evidence indicating no direct effect of MHD instability can be seen in the comparison of the pressure gradient at ρ=0.5 in the cases of higher magnetic field. Although the region around ρ=0.5 in the case with R_{ax}=3.6 m is located in the Mercier unstable region (see Fig.7), the similar pressure gradient (1.62×10^4J/m^3) to that in R_{ax}=3.75 m (1.72×10^4J/m^3) is realized simultaneously with a reduced electron heat conduction (1.40 m^2/s versus 2.37 m^2/s). Here it should be noted that the dominant loss channel of energy is considered to be an electron heat conduction as in the medium-sized experiments since the beam energy in the LHD experiment (150 keV) is much higher than the electron temperature. Pressure gradients are similar in both configuration at other radii. They are larger at ρ=0.9 than at ρ=0.5, which indicates a broad pressure profile. Since the NBI power deposition is more peaked in the case with R_{ax}=3.75 m than that with R_{ax}=3.6m, heat flux is reduced at ρ=0.5 in the case with R_{ax}=3.6m when the total deposition power is the same. The magnetic fluctuation spectrum in these two cases is shown in Fig. 7(c). There exists several peaks corresponding to low-n coherent modes in the case with R_{ax}=3.6m. The case with R_{ax}=3.6m accompanies larger fluctuation amplitudes and better confinement than the case with R_{ax}=3.75m. These two comparisons in Table 3 also indicate that the superiority of thermal transport in the case with R_{ax}=3.6 m to that with R_{ax}=3.75 m is retained in a wide collisional region (ν^*~1-5).

The Shafranov shift in heliotrons is well described by the 3-dimensional computation [24] and also a simple analysis of stellarator averaging scheme gives a reasonable qualitative agreement with experimental observation. When the ellipticity of the plasma is enlarged by the quadrupole component, i.e., in the case of $\kappa > 1$, the Shafranov shift is predicted to be reduced since the Shafranov shift normalized by the minor radius outside on the mid-plane is roughly conserved. Figure 8 (a) shows the Shafranov shift estimated from the tangential imaging of soft X-ray [25,26] as a function of an equilibrium beta for the three magnetic configuration with κ = 0.92,1.02 and 1.17. The equilibrium beta includes contribution of the beam pressure. Larger and smaller shifts are observed systematically in the cases with κ=0.92 and κ =1.17 than in the case of circle (κ =1.02), respectively. Figure 8 (b) shows a typical pressure profile in the hatched area in Fig.8 (a). The central electron temperature is 3.5 keV in this series of plasmas at 1×10^{19}m^{-3} with the NBI port-through power of 4 MW. When a general situation is the same for all three cases, the deposition power is larger and the profile is more peaked in the case of κ= 1.17 than in other two cases which have very similar profiles to each other. The vertically elongated configuration (κ=1.17) shows the reduced shift although a peaked pressure profile is expected due to the beam.

4. Pellet injection from different locations

Core fueling has been investigated intensively with regard to improvement of confinement as well as fueling efficiency. Pellet launching from the high magnetic field side has been attracting interest in recent tokamak experiments [27,28]. A significant shift of density redistribution from the particle deposition towards the outboard side in the major radius direction has been reported in these experiments. Therefore the high-field side launching, that is injection from the inboard in tokamaks, greatly enhances core fueling. The physical picture of the E × B drift of a high-beta plasmoid seems to successfully explain these phenomena [29] as far as small aspect-ratio tokamaks. Core fueling is an important issue in helical systems as well since a particle pinch has not been observed widely. The pellet launching from different location has been investigated in LHD. This is the first investigation in net current-free plasmas. Access to a plasma from a port is easier in LHD than tokamaks because of no central structure and a large aspect ratio (6~7 in LHD while ~3 in tokamaks). Figure 9 illustrates the two cases of launching from the top and the outboard side. The case of launching from the top corresponds to a local high-field side. The other case of launching from the outboard corresponds to the low-field side from the aspect of both local helical modulation and toroidicity. Figure 10 shows a particle deposition estimated from Hα emission during the ablation process and density redistribution in different launching locations. The condition of the target plasma is fixed. Although the peak of particle deposition is located at ρ=0.5, the peak of the increment of density moves outwards to ρ=0.9 in the case of the outboard launch. This significant shift is similar to the observation in the outboard injection in tokamaks. Rapid particle evacuation should be related to the deterioration of fueling efficiency and 30 % of supplied particles are lost promptly in this case. An outward shift of particles is also seen in the other case of launching from the top although pellet penetration is shallow because of the low velocity needed to maintain an intact pellet in the curved guide tube. The estimates of density deposit and redistribution do not make any significant difference in the time frame of 20 ms which is the repetition rate of the density profile measurement. Confinement characteristics after the pellet injection look the same for both cases. The inboard launching also gives a similar result. The ablated plasmoid is exposed to the E×B force as it diffuses along a field line. Since the rotational transform is larger in LHD than that in tokamaks, a plasmoid tube shifts round from the inside to the outside (or the other way round) more rapidly. Therefore this drift seems to be cancelled out to some extent in addition to less toroidal effect than in tokamaks. The E × B motion estimated by $(\nabla B/B)\cdot\nabla\rho$ is plotted along the field line in Fig.11. The start point of ϕ =0 corresponds to the ablated position in the case of outboard launching shown in Fig.9(a). The positive sign means inward motion in the minor radius direction. The case in LHD suggests inward motion in toroidal average although the predicted motion is complicated by the helical magnetic field. A tokamak with the same aspect ratio shows a small outward shift. Observed significant outward shift in the minor radius in LHD poses a question on the applicability of the E×B drift model.

5. Discussions

The configuration with the magnetic axis position, R_{ax} of 3.6m, which is shifted inward by 0.3 m from the nominal center of LHD and the toroidal averaged ellipticity, κ, of 1.02 has shown the best confinement performance in absolute value in this configuration study. The energy confinement in this configuration is scaled by $\tau_E \propto P_{abs}^{-0.60}\bar{n}_e^{0.47}B^{0.75}$. Therefore, an increase of density is a key issue in maximizing the stored energy. Figure 12 shows the typical waveform in the high density and stored energy attempts. The magnetic field is 2.8 T, and the port-through power of NBI and launching power of ICRF are 5 MW and 2 MW, respectively. While the loss of NBI power is estimated to be up to several percent, ICRF heating efficiency is unclear since the fundamental harmonic condition of minority hydrogen ions is much deteriorated due to a large concentration of hydrogen due to the pellet fueling. An increment of stored energy by ICRF of about 0.1 MJ suggests an absorbed power of 0.9 MW with the assumption of a regular energy confinement. The five pellets are injected from 0.4 s to 0.7s, which increases $\bar{n}_e$ beyond the $1\times10^{20}\mathrm{m}^{-3}$ in this short time [30,31]. While the stored energy behaves adiabatic during the pellet injection, it rises slowly due to confinement improvement by density increase [32] and reaches to 1.03 MJ at $\bar{n}_e$ of $8.5\times10^{19}\mathrm{m}^{-3}$ by P_{abs} of 6.5 MW. A confinement enhancement factor on the ISS95 is 1.4. Here two operational tools are successfully applied, i.e, a methane puff and an external magnetic perturbation by the local island divertor (LID) coil [33]. Since the key mechanism of favorable functions of both has not been clarified, the detailed description awaits a future work.

Although the operational magnetic field in a helical system is usually restricted by the resonance conditions of wave heating to generate the target plasmas, the establishment of a plasma-production scheme by NBI alone removes this restriction [34]. This technique has made possible a high beta study in low magnetic field and promoted an investigation of the magnetic field dependence substantially. The new pumping system which has tripled the pumping speed up to $85\mathrm{m}^3/\mathrm{s}$, the unique feature of freedom from disruption and the availability of a steady-state magnetic field have enabled a several -seconds long plasma discharge to be repeated every 3 minutes. This high repetition rate has enhanced experimental efficiency.

While the NBI heated plasmas are the primary subjects of this study, other notable achievements have been made by ICRF heating. In particular, the facts that ICRF heating alone (2.3 MW) has realized 240 kJ at moderate density ($1.7\times10^{19}\mathrm{m}^{-3}$) and indicates sufficient confinement of highly energetic trapped particles are notable[35]. Long pulse operation has been prolonged to 127 s by ICRF heating of 0.4 MW. These subjects related to ICRF heating will be reported elsewhere.

Since the basic transport characteristics are gyro-Bohm in NBI heated plasmas in LHD, micro-turbulence due to electro-static modes can be a candidate of anomalous transport. Figure 15 shows the linear growth rate of the ion-temperature-gradient and trapped-electron modes for the two cases described in Table 3. This is a result from the FULL code [36] which calculates the linear growth rate of a microinstability in a 3-dimensional geometry. The inner part is stable for both cases since the pressure gradient is below the threshold. Stability of the ITG mode in LHD can be attributed to shortening the connection length between adjacent good and bad curvature by the magnetic field modulation by helical and the negative magnetic shear[37]. Since the curvature is less preferable in the inward shifted configuration, the ITG mode can be excited more clearly than in the outward shifted configuration. The differences in microinstability result for this comparison do not explain the experimentally observed difference in transport.

6. Conclusions

The design study in LHD had indicated that a linear stability of an interchange mode is violated in the inward shifted configuration which has preferable characteristics for both neoclassical transport and confinement of high energetic particles. Therefore either saturation of the pressure gradient or major destruction of a profile had been predicted for the experiment. However, the actual experiment has indicated that the pressure gradient can be raised beyond the Mercier criterion. Representative achievements described in this article are the stored energy of 1MJ and the volume averaged beta of 3 %. The inward shifted configuration shows a 50 % enhancement on the ISS95 scaling up to $<\beta>$ of 3%. The superiority of the inward shifted configuration is distinguished in the comparison with the outward shifted configuration. The larger pressure gradient has been realized with reduced heat conduction in the case with R_{ax}=3.6m in spite of larger amplitude of magnetic fluctuation than in the case with R_{ax}=3.75m where the Mercier mode is stable. The appearance of the coherent mode with $m<10$ seems to be consistent with the prediction of the ideal linear MHD theory. Stability analysis suggests the high beta discharges beyond 2.2% enter the second stability regime around ρ=0.5. Although magnetic fluctuations of the resonant modes located there disappear indeed, the development of the pressure gradient has not been observed. The geometrical effect on the suppression of neoclassical transport is demonstrated by this inward shifted configuration as well. Any significant deviation from the ISS95 has not been observed deep in the collisionless regime down to ν^* of 0.05 while the outward shifted configuration which is not optimized to mitigation of the neoclassical transport has indicated significant degradation of confinement in the collisionless regime.

Distinguished characteristics observed in the inward shifted configuration in LHD give a new perspective of MHD stability and related transport in net current-free plasmas.

Acknowledgements

The authors acknowledge the continuous effort of all members of the device engineering group to reliably operate LHD.

References

[1] Iiyoshi A *et al* 1999 *Nucl. Fusion* **39**,1245
[2] Motojima O *et al* 2000, *Nucl. Fusion* **40**, 599
[3] Uo K 1971 *Plasma Phys.* **13**, 243
[4] Fujiwara M *et al* 1999 *Nucl. Fusion* **39**, 1659
[5] Motojima O *et al* 1999 *Phys. Plasmas* **6**, 1843
[6] Fujiwara M *et al* 1999 *Plasma. Phys. Contol. Fusion* **41**, B157
[7] Fujiwara M *et al* 2001 *Nucl. Fusion* (in press)
[8] Ichiguchi K *et al* 1993 *Nucl. Fusion* **33**, 481
[9] Ogawa Y *et al* 1992 *Nucl. Fusion* **32**, 119
[10] Mynick H E *et al* 1982 *Phys. Rev. Lett.* **48**, 322
[11] Itoh K *et al* 1994 *Plasma Phys. Control. Fusion* **36**,1501
[12] Fukuyama A et al 1994 *Plasma Phys. Control. Fusion* **37**,611
[13] Sakakibara S *et al* 2001 *Nucl. Fusion* in press
[14] Stroth U *et al* 1996 *Nucl. Fusion* **36**,1063
[15] Yamada H *et al* 2001 *Nucl. Fusion* in press
[16] Yamada H *et al* 2000 *Phys. Rev. Lett.* **84**, 1216
[17] Ohyabu N *et al* 2000 *Phys. Rev. Lett.* **84**,103
[18] Ohyabu N *et al* 2000 *Phys. Plasmas* **7**, 1802
[19] Murakami S *et al* 1995 *Trans. Fusion Technol.* **27**, 256
[20] Sudo S *et al* 1990 *Nucl. Fusion* **30**, 11
[21] Xu Y et al 2001 to appear in *Proc.28th EPS Conf. Controlled Fusion Plasma Phys. (Funchal, Portugal)*
[22] Cooper W A *et al* 1992 *Plasma Phys. Control. Fusion* **34**, 1011
[23] Toi K *et al* to appear in *Proc.28th EPS Conf. Controlled Fusion Plasma Phys. (Funchal, Portugal)*
[24] Yamada H *et al* 1992 *Nucl. Fusion* **32**, 25
[25] Liang Y *et al* 2001 *Rev. Sci. Instrum.* **72**, 717
[26] Liang Y *et al* to appear in *Proc.28th EPS Conf. Controlled Fusion Plasma Phys. (Funchal, Portugal)*
[27] Lang P *et al* 1997 *Phys. Rev. Lett.* **79**, 1487
[28] Baylor L R *et al* 1998 *Fusion Technol.* **34**, 425
[29] Parks P B *et al* 2000 *Phys. Plasmas* **7**, 1968
[30] Sakamoto R *et al* 2001 *Nucl. Fusion* **41**, 381
[31] Yamada H *et al* 2000 *Fusion Engineering Design* **49-50**, 915
[32] Yamada H *et al* 2000 *Proc. 27th EPS Conf. Controlled Fusion Plasma Phys. (Budapest, Hungary)* Vol.24B,p.1320
[33] Komori A *et al* 2001 *Phys. Plasmas* **8**, 2002
[34] Kaneko K *et al* 1999 *Nucl. Fusion* **39**, 1087
[35] Watari T *et al* to appear in *Proc.28th EPS Conf. Controlled Fusion Plasma Phys. (Funchal, Portugal)*
[36] Rewoldt G *et al* 2000 *Phys. Plasmas* **7**, 4942
[37] Kuroda T *et al* 2000 *J.Phys.Soc.Japan* **69**, 2485

Line-averaged density	$\overline{n}_e$	$1.5\times10^{20}\mathrm{m}^{-3}$
Energy confinement time	τ_E	0.36 s
Plasma stored energy	W_p	1.03 MJ
Electron temperature	$T_e(0)$	4.4 keV
Ion temperature	$T_i(0)$	3.5 keV
Volume-average beta	$<\beta>$	3.0 %
Discharge duration		127 s

Table 1 Maximum plasma parameters achieved in LHD

R_{ax}(m)	3.6			3.75	3.9
κ	0.92	1.02	1.17	1.03	1.01
W_{core}/W_{total}	0.58±0.05	0.58±0.07	0.72±0.07	0.51±0.07	0.53±0.07

Table 2 Ratio of the stored energy in the core to the total stored energy.

shot #	#11369	#16727	#25664	#25708
Global parameters				
R_{ax} (m)	3.6	3.75	3.6	3.75
B (T)	1.5	1.5	2.8	2.64
W (MJ)	0.192	0.130	0.371	0.335
$<\beta>$ (%)	0.65	0.48	0.36	0.37
$\overline{n}_e$ ($10^{19}\mathrm{m}^{-3}$)	2.36	2.35	4.97	4.62
P_{abs} (MW)	1.19	1.73	1.67	3.17
τ_E (s)	0.162	0.074	0.222	0.108
$\tau_E/\tau_E^{\mathrm{ISS95}}$	1.69	1.15	1.10	0.94
$\rho = 0.5$ (near $\iota\!\!\!-$ =0.5)				
$-dp/d\rho$ (J/m^3)	1.20×10^3	1.43×10^3	1.62×10^4	1.72×10^4
ρ^*	2.80×10^{-3}	2.75×10^{-3}	1.31×10^{-3}	1.67×10^{-3}
ν^*	1.01	1.09	4.40	2.70
χ_e (m^2/s)	2.13	3.15	1.40	2.37
$\rho = 0.9$ (near $\iota\!\!\!-$ =1)				
$-dp/d\rho$ (J/m^3)	6.36×10^3	6.66×10^3	1.93×10^4	1.76×10^4
ρ^*	1.65×10^{-3}	4.16×10^{-3}	7.30×10^{-4}	1.05×10^{-3}
ν^*	3.12	3.31	10.3	6.60
χ_e (m^2/s)	0.99	1.59	1.03	1.79
Magnetic fluctuation				
$\tilde{B}/B_{eq}$ (10^{-5})	2.45	0.59	1.30	0.51
$\tilde{B}(m/n=2)/B_{eq}$ (10^{-5})	0.25	undetected	0.26	undetected

Table 3 Global plasma parameters and local parameters at the major rational surfaces for the dimensionally similar discharges with different magnetic axes.

Figure captions

Figure 1 Mercier unstable region and diffusion coefficients of a neoclassical transport [10] and an anomalous transport model [11] as a function of the magnetic axis position. Here pressure profile of $p=p_0(1-\rho^2)(1-\rho^8)$ with $<\beta> = 1\%$ is assumed for evaluation of the Mercier criterion.

Figure 2 Dependences of confinement enhancement factor over the ISS95 scaling on non-dimensional parameters. (a) Collisionality. (b) Beta.

Figure 3 Enhancement factor of energy confinement time on the ISS95 scaling for different magnetic configuration. Squares are derived from the total stored energy. Triangles are derived from the core part which is subtraction of pressure at $\rho=0.9$ from the entire part. (a) Scan of the magnetic axis position. Ellipticity κ is fixed at 1. (b) Scan of the ellipticity. R_{ax} is fixed at 3.6m.

Figure 4 (a) Waveforms of the discharge pushed to 3.0%. Top: volume averaged beta and absorbed NBI heating power. 2nd top: line averaged density and confinement enhancement factor on ISS95. 2nd bottom : magnetic fluctuation outside the plasma. Bottom: contour of coherent fluctuation amplitude. (b) Electron temperature profile projected on to the vacuum magnetic surfaces.

Figure 5 Evolutions of (a) pressure gradient at $\rho=0.5$ and (b) amplitude of coherent magnetic fluctuation with the resonance of 1/2 along with the volume averaged beta $<\beta>$. Mercier unstable (dotted line) and low-n mode unstable region (fat solid line) are also illustrated in (a). The areas shown by arrows are unstable. A time trace of the discharge shown in Fig.4 is illustrated by a thin solid line.

Figure 6 Evolutions of (a) pressure gradient at $\rho=0.9$ and (b) amplitude of coherent magnetic fluctuation with the resonance of 1/1. Mercier unstable (dotted line) and low-n mode unstable region (fat solid line) are also illustrated in (a). The areas shown by arrows are unstable. A time trace of the discharge shown in Fig.4 is illustrated by a thin solid line.

Figure 7 Comparison of dimensionally similar discharges with different magnetic axes, R_{ax}= 3.6 m and R_{ax}= 3.75 m. Those correspond to #25664 and #25708 in Table 2, respectively. Electron temperature, density and iota profiles are shown in (a) of the case with R_{ax}= 3.6 m and (b) of the case with R_{ax}= 3.75 m. (c) Power spectrum of the observed magnetic fluctuation.

Figure 8 (a) The observed Shafranov shift for the configuration with different ellipticity with the same R_{ax} of 3.6 m. (b) Beam and bulk pressure profiles with typical plasma parameters in the hatched region in (a).

Figure 9 Magnetic geometry at the launching cross section of the pellet. (a) Launch from the outboard. (b) Launch from the top. Contours of magnetic field strength are also plotted. The magnetic field increases in the direction of solid arrows and decreases in that of broken arrows.

Figure 10 Profiles before and after pellet injection. Top: electron density. Middle: electron temperature. Bottom: Hα intensity indicating pellet penetration, calculated deposition and measured increase of density. (a) Launch from the outside. (b) Launch from the top.

Figure 11 Distribution of the strength of E×B drift along with the magnetic field line. A half turn in the toroidal direction is plotted. Solid line : LHD. Broken line : Tokamak like field with the same aspect ratio as LHD.

Figure 12 Waveforms of the discharges for high stored energy attempt. Top: stored energy W_p and injected heating power P_{NBI} and P_{ICH}. Bottom: line averaged density $\overline{n}_e$ and confinement enhancement on the ISS95 scaling.

Figure 13 Linear growth rate of the ITG and TEM mode for different magnetic configuration described in Table 3 (R_{ax}=3.6m:#11369, R_{ax}=3.75m:#16727)

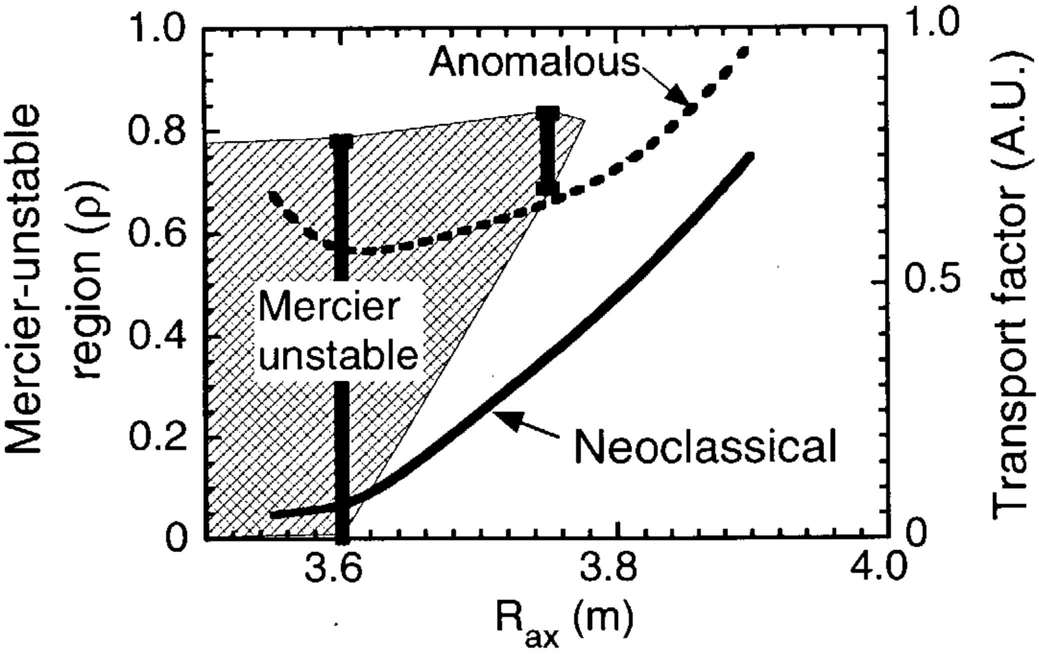

Figure 1

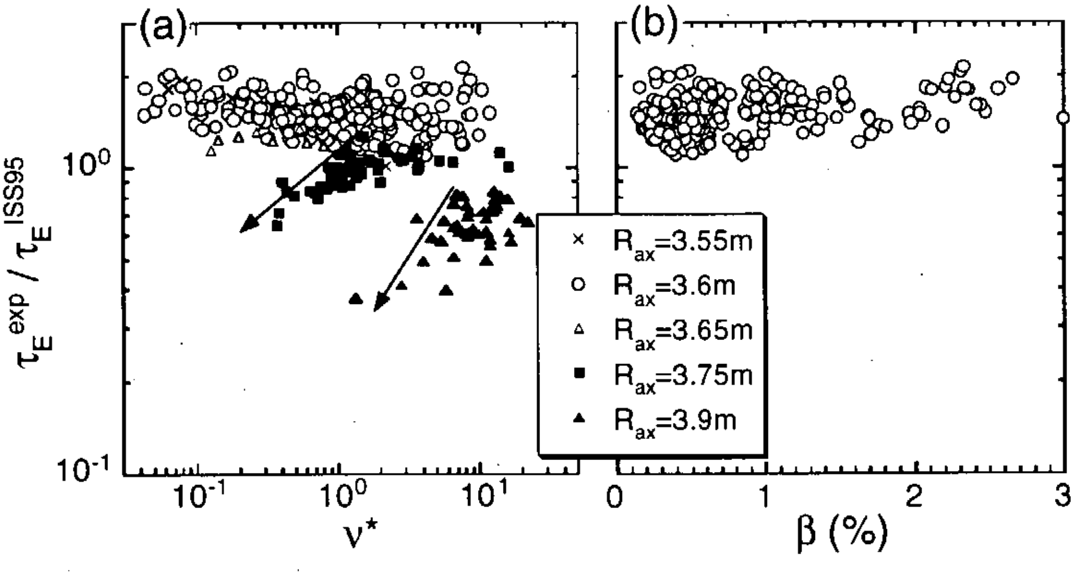

Figure 2

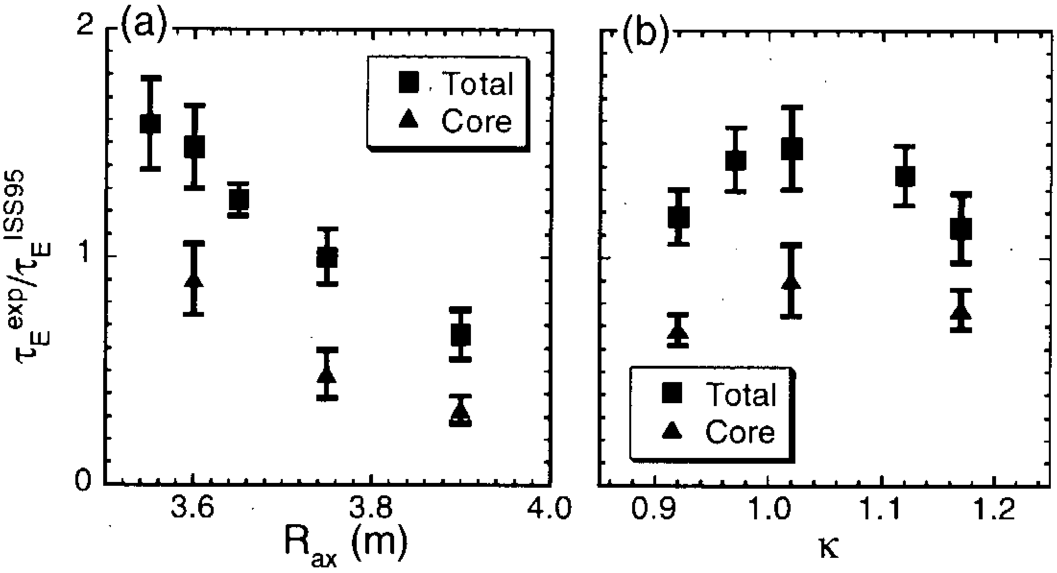

Figure 3

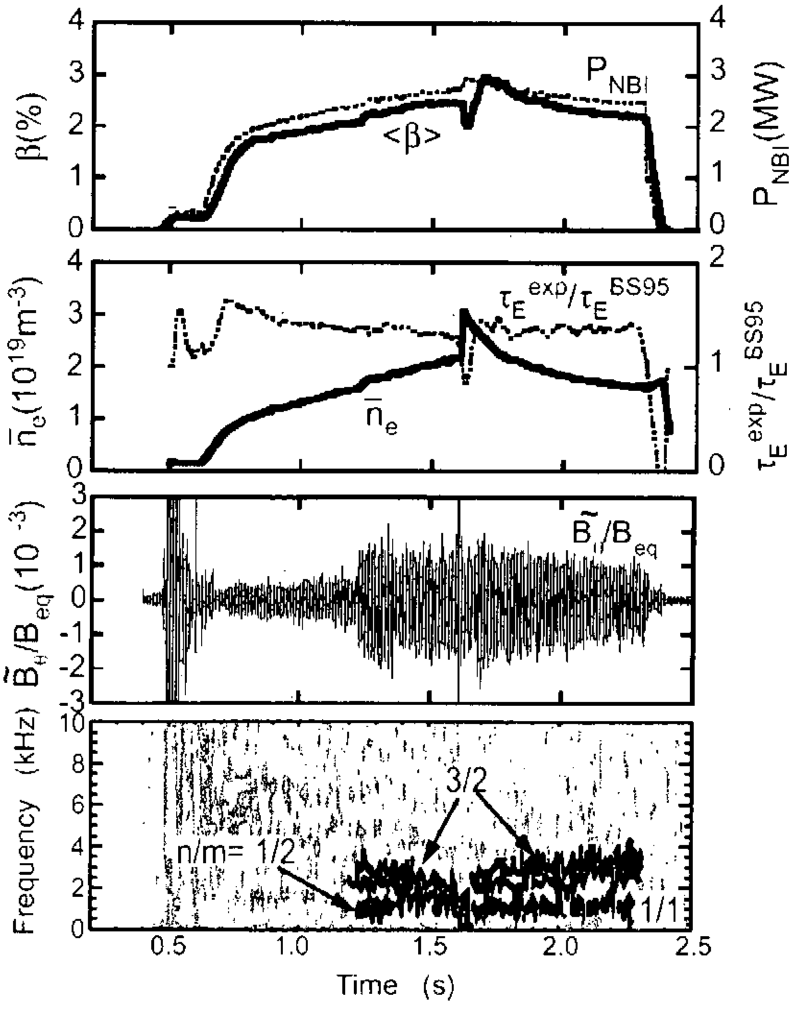

Figure 4(a)

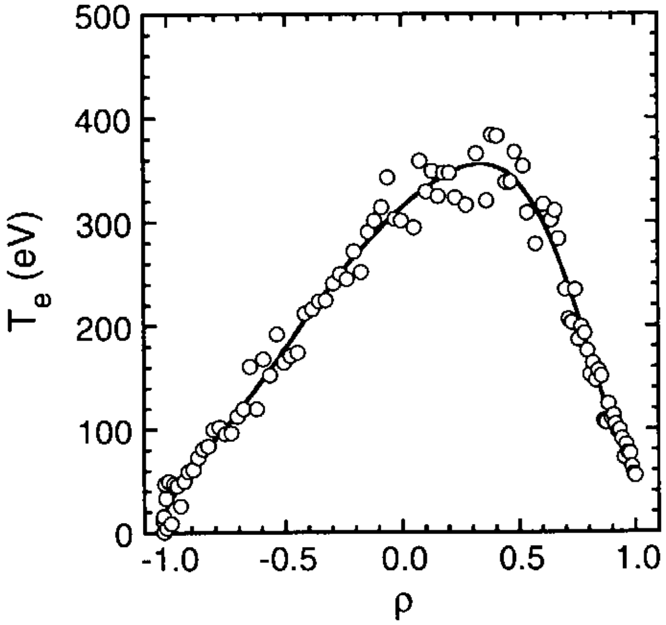

Figure 4 (b)

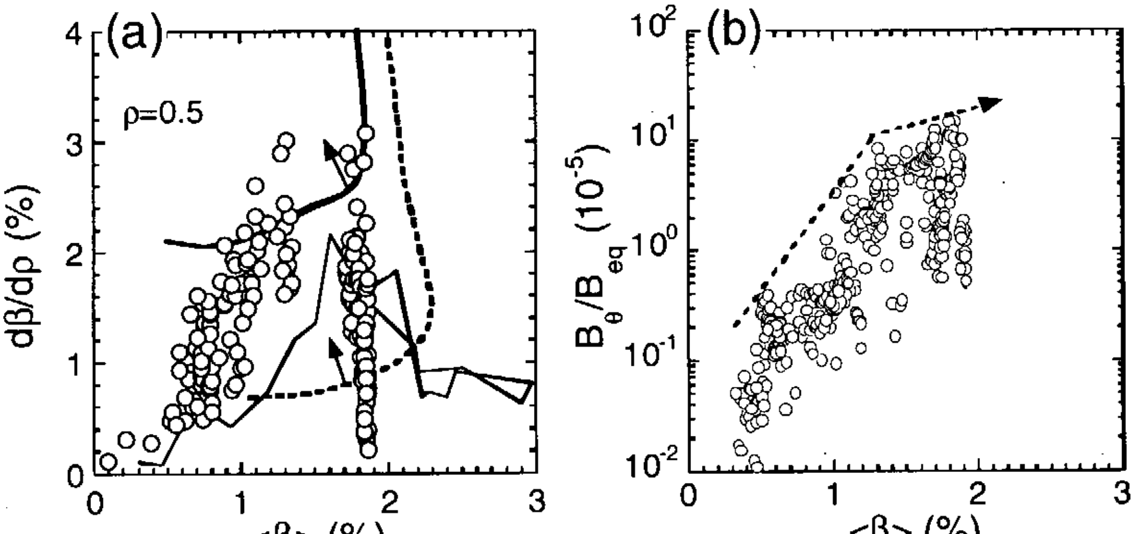

Figure 5

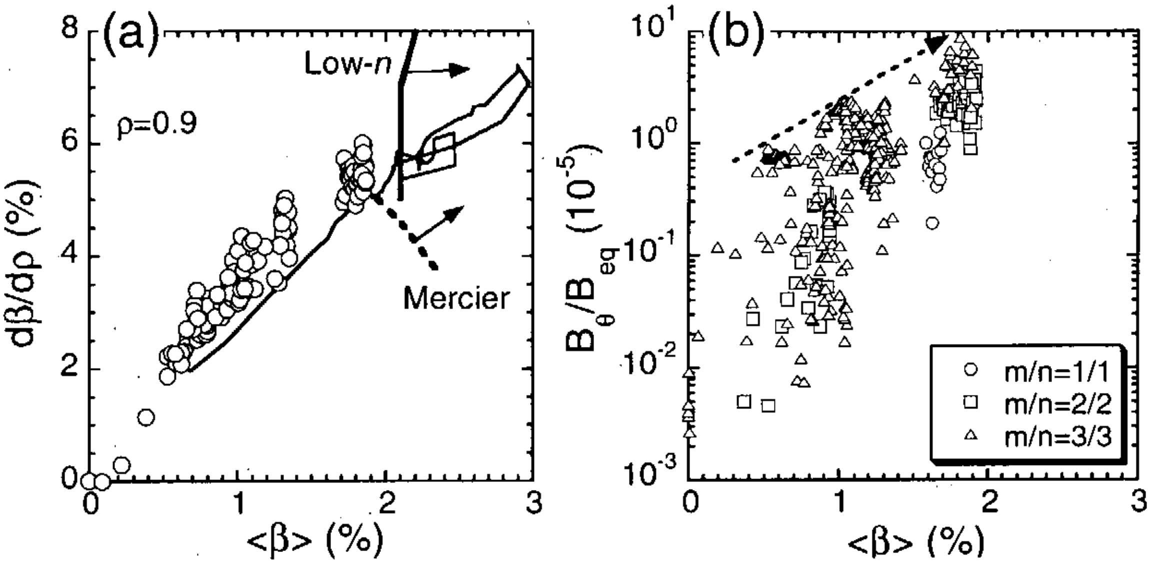

Figure 6

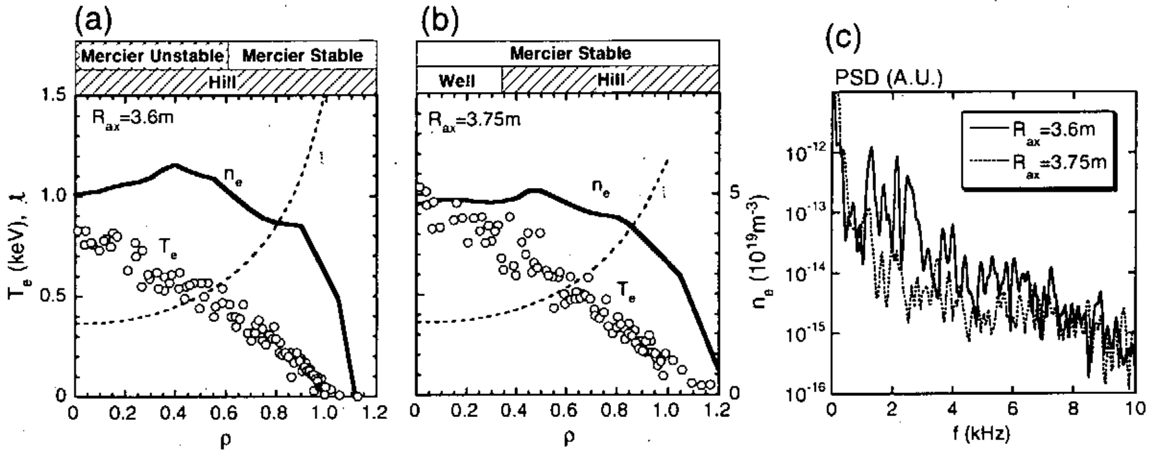

Figure 7

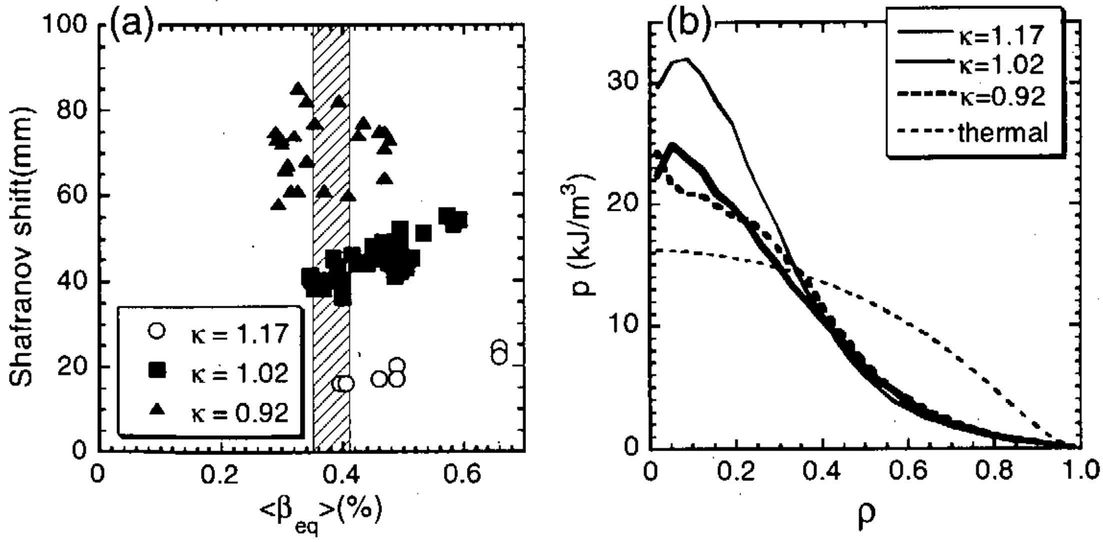

Figure 8

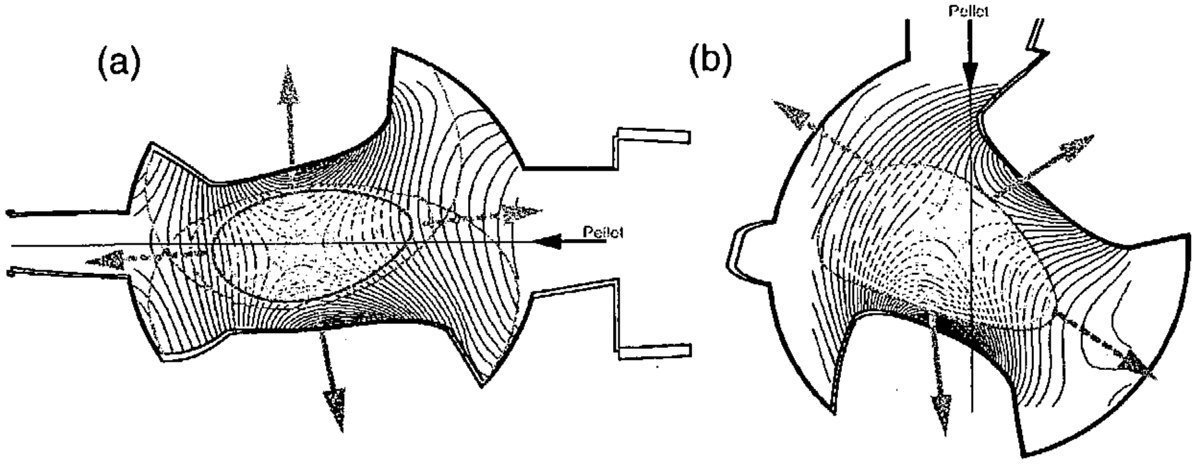

Figure 9

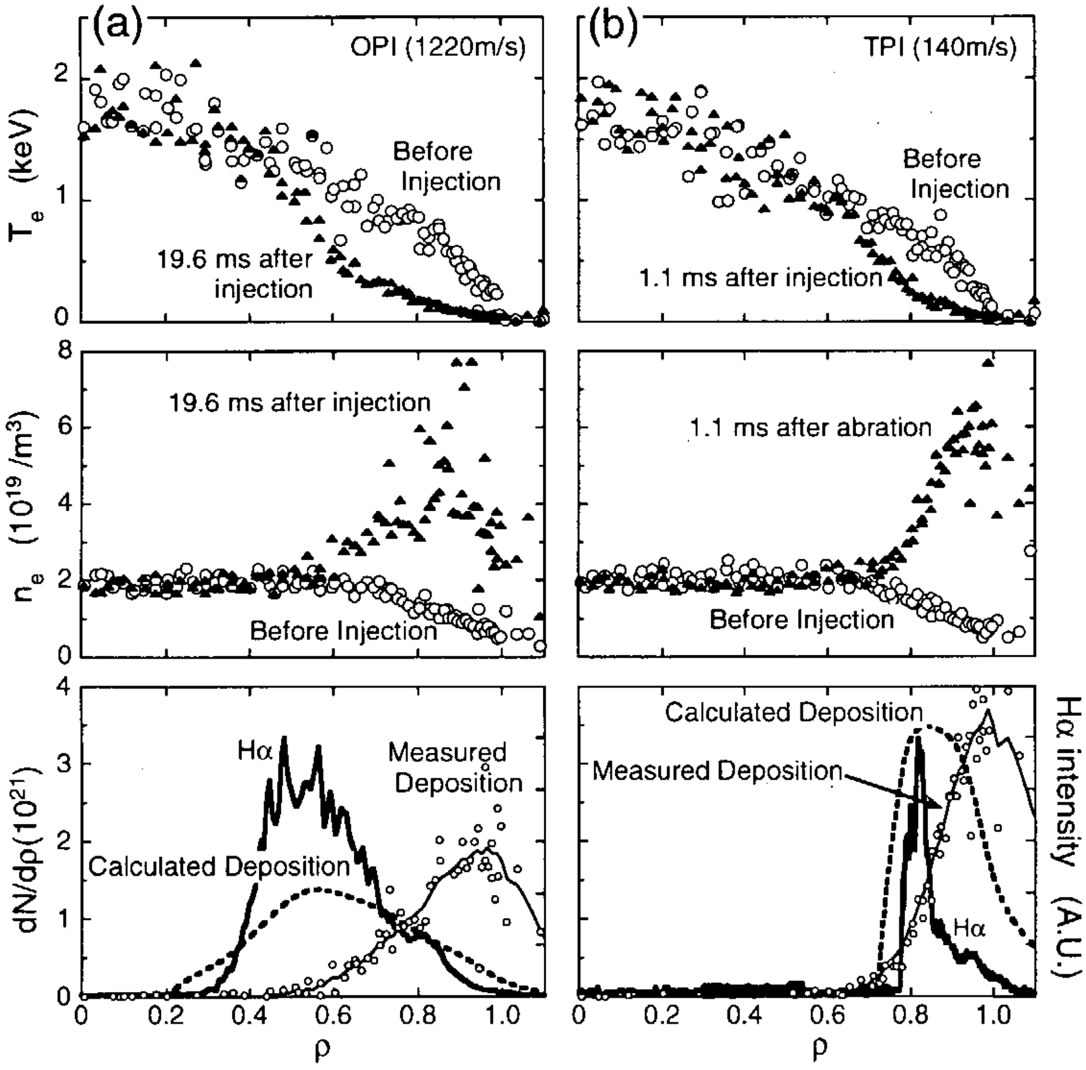

Figure 10

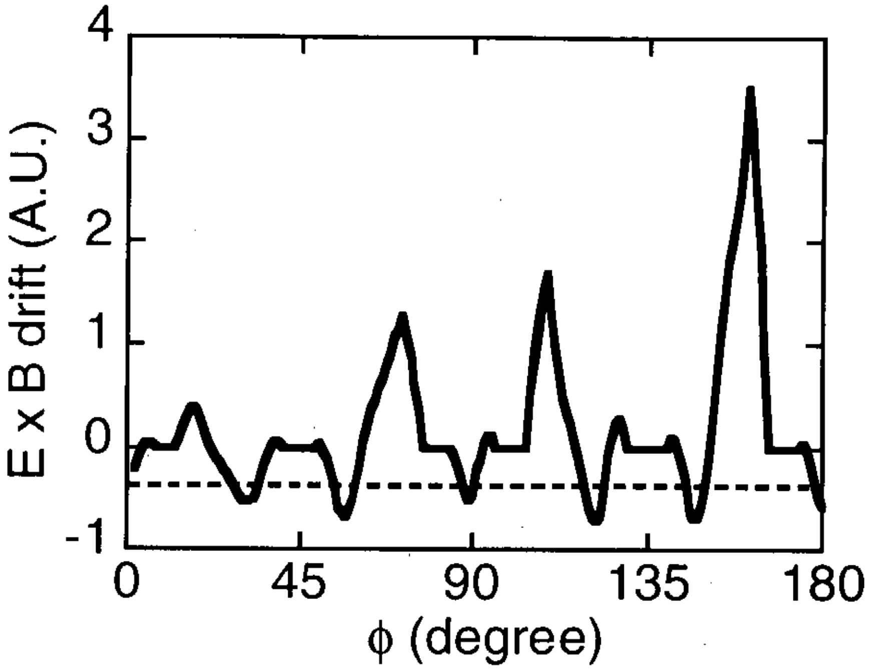

Figure 11

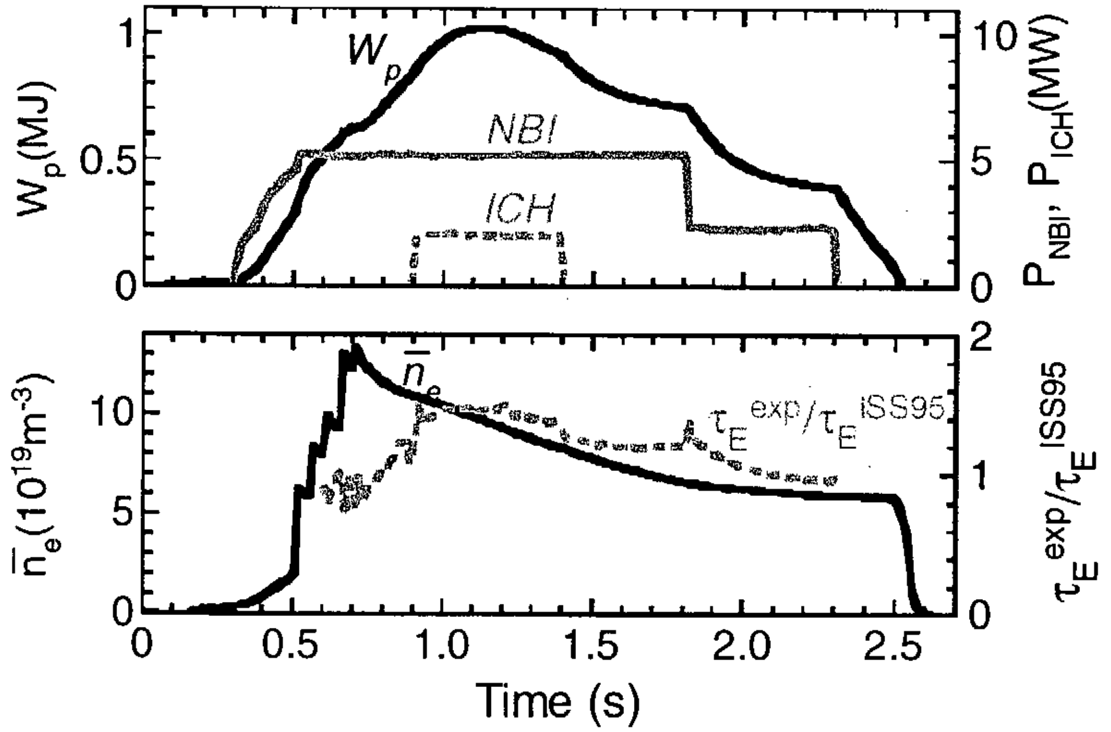

Figure 12

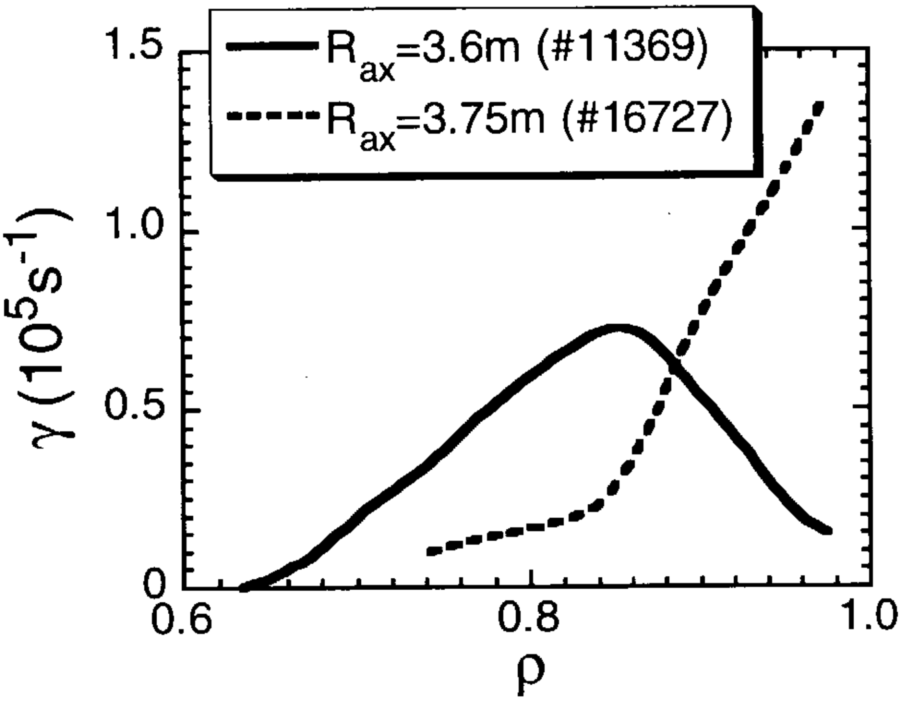

Figure 13

Pulsed Radar Reflectometer for Density Profile and Fluctuation Measurements of Large Helical Device.

T. Tokuzawa, K. Kawahata, K. Tanaka, R. O. Pavlichenko[1], A. Ejiri[2],
and LHD experimental group

National Institute for Fusion Science, Toki 509-5292, Japan,
[1]Research Center for Development of Far-Infrared Region, Fukui University,
Fukui 910-8507, Japan
[2]Graduate School of Frontier Sciences, Univ. Tokyo, 113-0033, Japan

1. Introduction

It is very important to know the edge density profile and fluctuation information for the magnetic confined plasma experiments. In order to measure these plasma parameters with high temporal and spatial resolution, we try to apply microwave reflectometer on Large Helical Device (LHD) [1, 2]. Reflectometer is a compact system, needs a small access to the device, and also has a higher resolution than conventional diagnostic methods. For these benefits, several types of reflectometer have been used in world fusion devices [3]. Since LHD has a complex magnetic field configuration and also has a large magnetic shear, the launched and the reflected microwave may have a complicated behavior such as the mode conversion or the polarization rotation [4, 5]. To study the effect of the strong magnetic shear, the pulsed radar reflectometer is a suitable reflectometric technique. Because pulsed radar reflectometry measures the delay time of the reflected wave from the cutoff layer in the plasma, it can distinguish between X-mode and O-mode polarized waves even if unexpected pulses are returned.

2. Pulsed radar reflectometer system

We construct V-band and R-band pulsed radar reflectometer systems. The schematic of V-band 2ch pulsed radar reflectometer system is shown in Fig. 1. 60GHz and 65GHz Gunn oscillators are used as sources. The output powers of both sources are 100 mW. PIN switches are used as a pulse modulator using the tuned signal of the generated impulse output. The microwave pulses pass through the oversized waveguide in order to avoid the deformation. The separate, transmitter and receiver horns are used in order to avoid the mixture of spurious reflecting components in the waveguides, vacuum window, etc. The antenna is a conical horn with a Teflon lens for focusing the microwave beam and can be moved horizontally and rotated using a remote controller. In a mixer the reflected wave picked up by the receiver horn is mixed with the local microwave, which the frequency of the local oscillator is 78 GHz. The intermediate frequency signal is divided and each signals are filtered by band-pass-filter with the bandwidth of ±1.0 GHz then detected and converted from the envelope of the reflected wave to the pulse. The reference pulse for the TOF measurement is measured using V-band detector, which is located at just after the PIN switch to avoid the jitter of the pulse generator and the PIN switch. The pulse width is around 2 ns and the repetition rate is 100 kHz in the standard operations. The detected pulses are fed to a diagnostics room using the electro-optical converters and the optical cables. Then time-of-flight (TOF) measurement is carried. A constant fraction discriminator (CFD) is used to obtain the start and the stop pulse for the time-to-amplitude converter (TAC), because the pulse amplitude is changed during the plasma discharge. The obtained data is acquired by CAMAC (Aurora 14 with 12 bits 1 Mword memory) and stored by a windows-NT based personal computer.

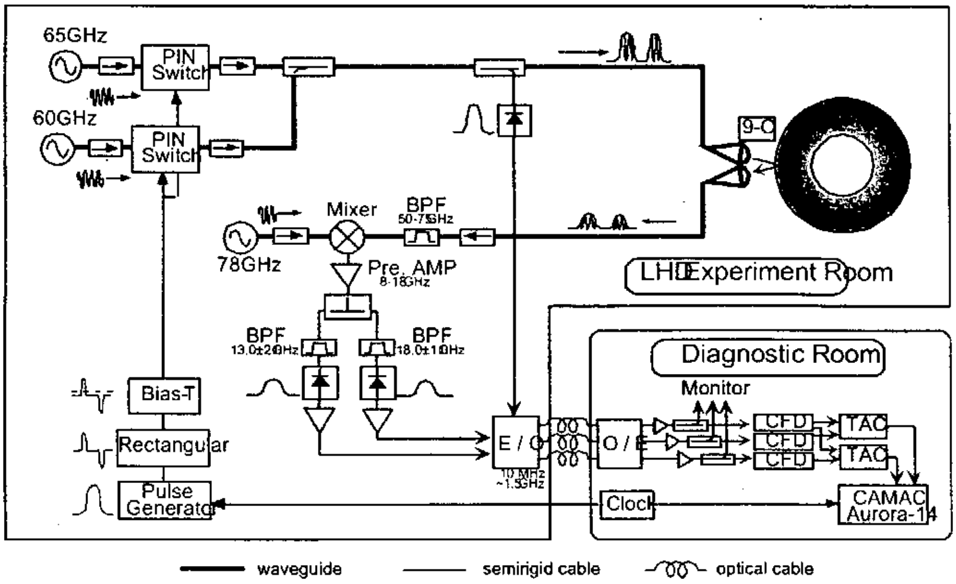

Figure 1. Schematic of 2ch U-band pulsed radar reflectometer system. The R-band system is similar; the probe frequencies are 33 and 39GHz, and the local frequency is 51GHz.

3. Experimental results

LHD plasma is usually initiated by ECH and then neutral beam is injected. Launching an X-mode microwave pulse the initial critical layer of the right-hand cutoff frequency of 60 GHz is located at R=4.3m and that of 65GHz is located at R=4.2m, where R is the major radius. Figure 2(a) shows the time evolution of the delay time. In this case both reflected pulses are appeared at the same time. When plasma is initiated by only NBI, the reflectometer signals show different behavior. In Fig. 2(b), 65 GHz reflected pulse appears at 0.415s and then 60 GHz reflected pulse appears with 20ms delay. It is clearly found that the plasma is initiated in the core region and then plasma is expanded in the case of NBI start-up plasma.

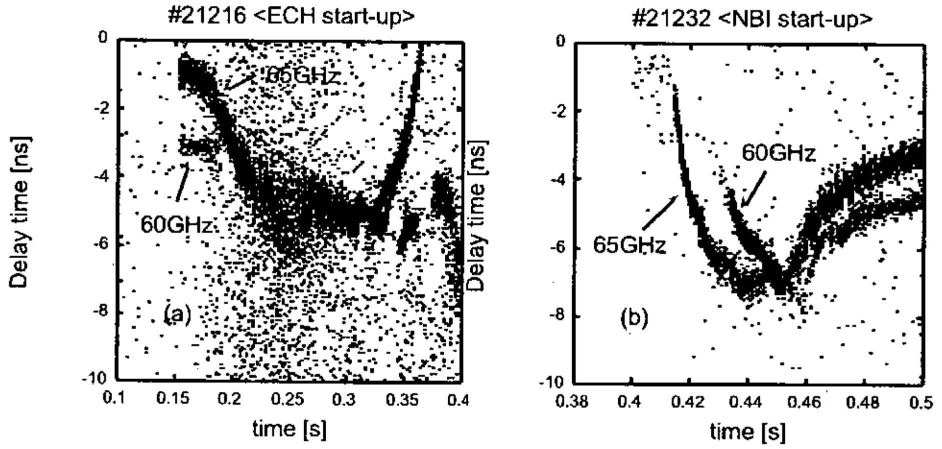

Figure 2. Time evolution of the delay time of reflected pulses. (a)ECH start-up plasma and (b) NBI start-up plasma.

Pulsed radar reflectometer has an ability to measure the density profile and density fluctuation, simultaneously. Figure 3(a) shows the time evolution of the delay time in an ECH initiated and ICH sustained plasma shot. After heating by ECH the fluctuation grows up and the core density decreases. The enlargement time evolutions are shown in Fig. 3(c) and (d). The coherent oscillation is measured by both diagnostics. This oscillation is density fluctuation with low frequency of 260 Hz.

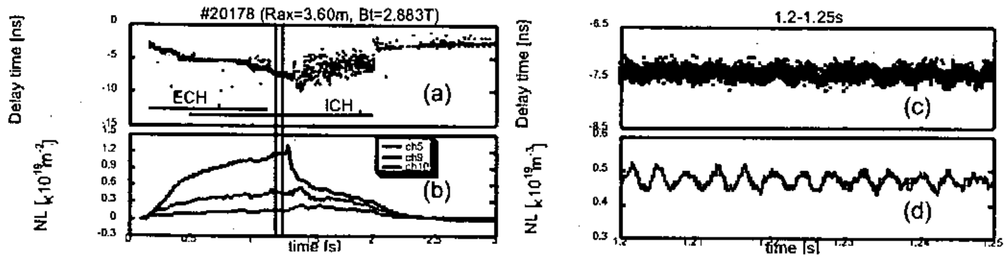

Figure 3. Time evolution of (a)the delay time of reflected pulse and (b)FIR interferometer signals. The enlargement time evolution from 1.2s to 1.25s of (c) reflectometer signal and (d)ch9 of FIR signal.

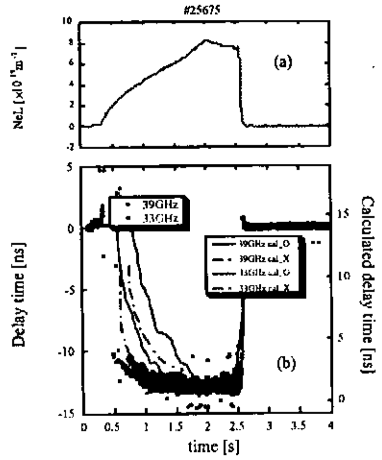

Figure 4. (a) Time evolution of the averaged density and (b) the dots are the delay time of reflected pulses, the solid lines are the calculated delay time using the density profile, and the dotted lines are the calculated delay time using the assumption that the waves propagate as X-mode.

At O-mode operation using R-band reflectometer system, two pulses are reflected from corresponding positions of each plasma frequency. The time evolution of the delay time is shown in Fig. 4(b). In this figure, the dotted lines are the delay time measured by pulsed reflectometer and the solid lines are the calculated delay time using the density profile measured by FIR interferometer. The reflected pulses are appeared when the electron density reaches to be the corresponding cutoff densities. Both values of the delay time are almost agreement in the edge region, however they are not agreement in more core region. The dotted line shows the estimation of the delay time assuming X-mode microwave pulse propagates from the edge to the O-mode cutoff layer. Nevertheless this assumption is over estimation, the measured signal is not able to be explained. This disagreement is probably caused by the ambiguity of density profile reconstruction and/or by the error of estimation for the cutoff position. We need to study the detailed effect of the magnetic shear to the wave propagation using the simulation analysis.

Acknowledgements

This work was supported in part by a Grand-in-Aid for Scientific Research from JSPS.

References

[1] M. Fujiwara et al., Nuclear Fusion, 39, 1659 (1999).
[2] O. Motojima et al., Physics of Plasmas, 6, 1843 (1999).
[3] (Ed.) K. Kawahata, Research Report NIFS-PROC-49
[4] I. Fidone and G. Granata, Nucl. Fusion 11, 133 (1971).
[5] K. Nagasaki et al., Phys. Plasmas, 6, 556 (1999)

RADIAL PROFILE OF METALLIC IMPURITIES OBTAINED FROM X-RAY PULSE HEIGHT ANALYZER IN LHD

S. Muto, S. Morita, and LHD Experimental Group
National Institute for Fusion Science, Toki, Gifu, 509-5292, Japan

1. Introduction

Measurement of x-ray spectrum is important to investigate fundamental properties of magnetically confined high temperature plasma, since it can give information on electron temperature, impurity, and nonthermal electron [1,2]. Recently, it is intended to rise up the spectral, spatial and temporal resolution in the x-ray diagnostics, because it is required to obtain important information such as the shift of magnetic axis, T_e profile, spatial distribution of metallic impurities and especially spatial distribution of nonthermal high energy electrons driven by electron cyclotron heating. However, in the energy range of x-ray it is fundamentally difficult to get simultaneously high spectral, spatial and temporal resolution. Recent technology dose not yield any applications which can fully accomplish this problem.

An assembly of pulse height analyzer (PHA) has been constructed in Large Helical Device (LHD) [3,4]. The assembly is equipped with a utility called a radial scanning system which modulates and identifies the sight line of PHA along major radius direction of LHD. It is the advantage of the system that permits adjustable acceptance of the sight line and improvement of scanning time. The scanning range of the system fully covers the plasma in the radial direction.

The radial profiles of K_α lines of metallic impurities such as titanium, chromium and iron have been successfully observed with the assembly. The energy shift of K_α line is also observed for each radial viewing chord. In addition to the experiment the radial distribution of line intensity emitted from each ionic state of metallic impurity is calculated as a function of electron temperature and density profiles. As a result, absolute density has been estimated from the comparison with the experimental result and the calculation. In the present article radial distribution of respective ionic state of metallic impurity is reported.

2. Radial scanning PHA system

The assembly is equipped with four x-ray detectors arranged along major radius direction with a space interval of 300 mm. Each detector consists of four pre-amplifiers, a portable liquid nitrogen cryostat, and four Si(Li) elements mounted inside a vacuum enclosure with a 12.5-μm-thick beryllium window. Each of the four elements is arranged on the corners of 13 mm square. The diameter of each element is 8 mm. Since the semiconductor x-ray detector is easily influenced by electromagnetic noise and mechanical vibration, the detectors are electrically and mechanically isolated from a supporting stage and fully covered with a copper shield. These special items of the isolation and shield are intrinsic to avoid a systematic error in signal. Main amplifiers are set into a copper box which is close to the detector. A calibration of the detector has been carried out using an x-ray source which emits intense lines of iron K and K . The energy resolution of the detectors has been adjusted to 170 eV at 6.5 keV.

The radial scanning system consists of four movable circular slits, and can modulate and identify the sight lines of the PHA along the major radial direction of LHD in a time interval of a few hundred msec. As a result, the data are successfully obtained with a spatial resolution of a few millimeters.

3. Experiment and discussion

Figure 1 shows typical profiles obtained with the assembly. The spatial resolution is roughly 30 mm in the major radial direction. Each point for impurity represents the integrated emission which has been observed through each sight line with a time integration of 240 msec. The radial profile of electron temperature estimated from continuous spectrum is also indicated. At present the duration of the scanning was approximately 8 s. The time resolution will be improved in next step. The plasma parameters were constant during the accumulation of the data. The assembly also makes it possible to estimate the line intensity and electron temperature near = 1.0, as is shown in the figure.

Figure 2 shows line spectra observed through two different positions of sight line. These spectra have been measured through a 1-mm-thick beryllium. In the figure reduced intensities are described. In comparison with the two lines it is remarkably indicated that there is a shift between the K lines of iron. The photon energy is different between K lines emitted from respective ionic state. It qualitatively reflects K lines from lower charge states increase at the position of = –0.54 in comparison with the case of the position of = 0.0.

Radial profile of K line emitted from metallic impurities has been analyzed to estimate the radial distribution of respective ionic state of each metallic impurity. Figure 3 shows radial profiles obtained from the experimental result and a cord calculation. In the calculation the diffusion coefficient of each impurity is assumed to be 0.2 m^2/s. Each calculated radial profile of line spectrum emitted from respective ionic state is shown in Fig.4.

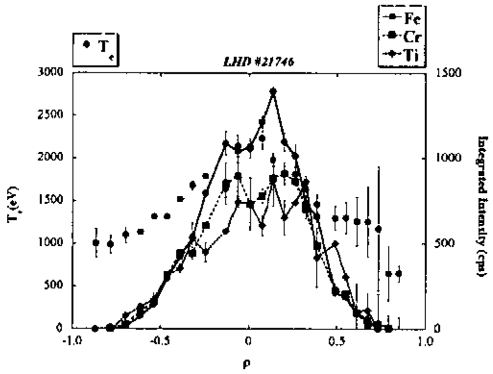

Fig.1. Radial profiles of electron temperature and each K line emitted from metallic impurities of iron, chromium, and titanium, respectively. For K lines the vertical axis means the line integral along the sightline, while the horizontal axis means the position of sightline.

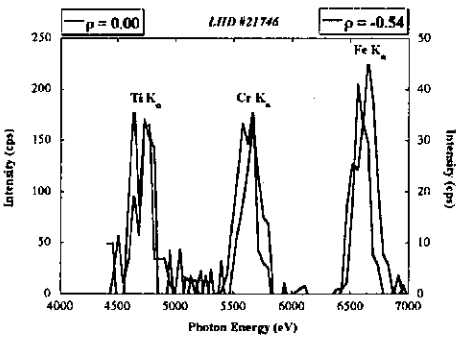

Fig.2. Each K line of titanium, chromium, and iron. The scale of vertical axis is different between the two positions of sight line. The vertical axis indicates the intensity which is line integral along the sightline. The intensity of continuous spectrum is subtracted.

In the case of the temperature, as is shown in the Fig.1, it is shown that the intensity of the line spectrum is mainly contributed from He-like, Li-like, Be-like, and B-like. In the case of iron the most intense line is emitted from Li-like ion within = 0.6. As is shown in Fig.5(a), it suggests no emission to the line from H-like ion. The concentration of iron is estimated to be approximately 0.008 % from the comparison shown in Fig.3. By the same method the concentrations of chromium and titanium are also estimated to be approximately 0.003 % and 0.001 %, respectively.

The calculation is also consistent with the experimental result on spectral profiles taken from = 0.62 (see Fig.5(b)). The photon energy of K emission depends on the ionic state as mentioned above. The detector equipped with the assembly has energy resolution enough to obtain the energy shift of the line.

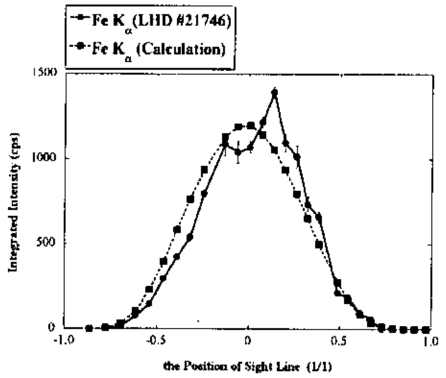

Fig.3. Comparison of radial profiles between an experimental result and a cord calculation.

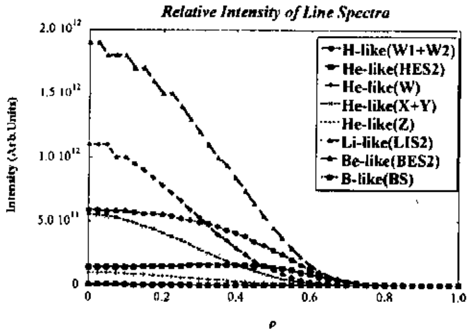

Fig.4. Calculated radial profile of respective ionic state of iron. In the calculation the diffusive coefficient is assumed to be 0.2 m^2/s. The intensity emitted from the ionic state of H-like is at zero level in the figure.

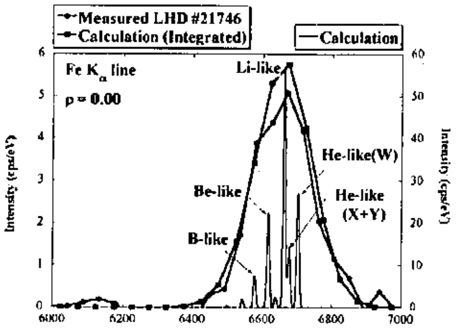

Fig.5(a). Comparison of integrated intensity profiles between the experimental result and the calculation. The intensity is integrated along sight line in a case of =0.0. The intensity of respective line structure is also indicated.

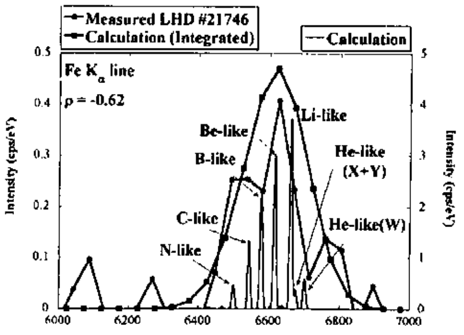

Fig.5(b). The integrated intensity along sight line in a case of = -0.62.

Figure 6 shows the radial distribution of each metallic impurity estimated from the analysis. The concentration of each metallic impurity is also indicated. The dominant ionic state is

He-like in each case around plasma center, while the concentration of bear ion and H-like ion are much lower than that of He-like ion.

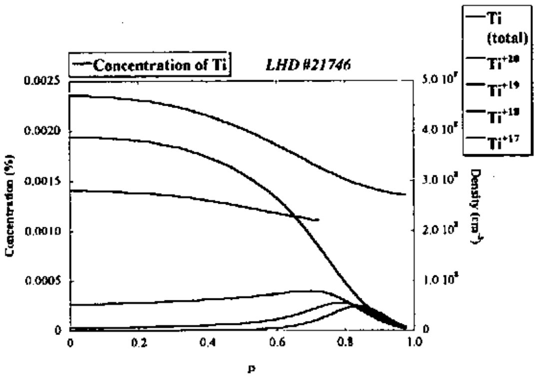

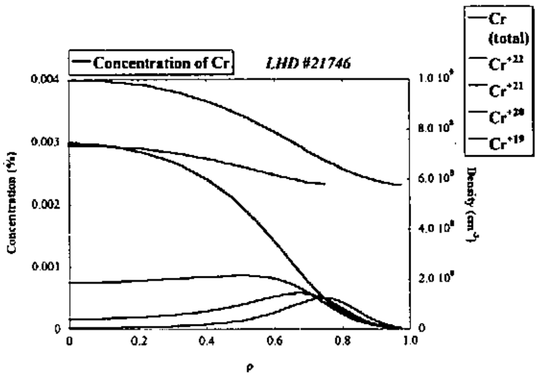

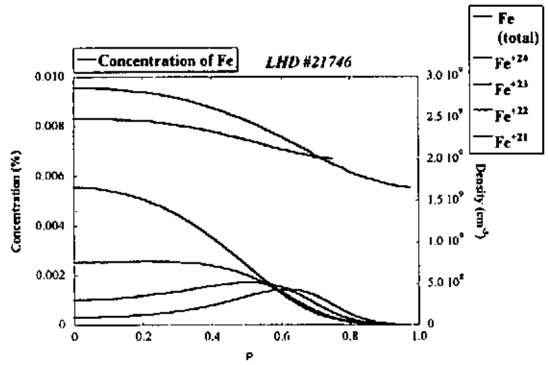

Fig.6. The estimated radial distribution of each metallic impurity. The concentration and the density are estimated from the comparison with the experimental result and the calculation. Only ionic states mainly contributing to the line intensity are shown.

3. Conclusion and future prospect

Development of an assembly equipped with a radial scanning system has attained a remarkable progress on method for radial profile of x-ray spectrum in connection with conventional utilization of PHA. The line spectra have been successfully observed with good energy resolution enough to analyze the energy shift of the K line. From the analysis of observed profiles, the radial distribution of each ionic state is estimated in the case of titanium, chromium, and iron, respectively.

Although improvement of the assembly must be made in order to achieve better counting rate, the further operation of the assembly will greatly contribute to studies on high temperature plasma concerning metallic impurities.

Mounting of a detector sensitive to hard x-ray region is currently in progress. Studies on the radial profile of high energy tail driven by electron cyclotron heating are the next target.

Reference

[1] T.Cho *et al.*, Phys. Rev. Lett. **64**, 1373(1990).
[2] T.Cho *et al.*, Phys. Rev. A **45**, 2532(1992).
[3] S.Muto and S.Morita, Fus.Eng.Des. **34-35**, 205(1997).
[4] S.Muto and S.Morita, Rev.Sci.Instrum. **72** (2001) 1206-1209

A Multichannel 118.8 μm-CH_3OH Laser Interferometer for Electron Density Profile Measurements in LHD

K. Kawahata, K. Tanaka, T. Tokuzawa, Y. Ito, A. Ejiri[1], S. Okajima[2]
and LHD Experimental Group

National Institute for Fusion Science, Toki 509-5292, Japan
[1]*Graduate School of Frontier Sciences, Univ. Tokyo, Tokyo 113-0033, Japan*
[2]College of Engineering, Chubu University, Kasugai 487-8501, Japan

Abstract

A 13-channel far infrared laser interferometer has been developed and routinely operated for the measurements of the spatial and temporal behaviors of the electron density in the Large Helical Device (LHD). The optical configuration is of the Michelson interferometer type with a heterodyne detection system. The light source is a highly stable twin 118.8-μm CH_3OH laser pumped by a cw CO_2 laser, which is developed in NIFS. All the optical components of the interferometer except laser sources are mounted on a massive stainless steel frame, which encircles the plasma vacuum vessel and is placed on three vibration-isolating mounts. The observed fringe shifts caused by the mechanical vibrations of the system is 1/100 fringes for the high frequency components of $f > 1$ Hz and 1/50 fringes for the low frequency components. The phase-shift measurement is made with an accuracy of 1/100 of a fringe, corresponding to a minimum measurable line-averaged density of 5.6×10^{16} m^{-3} at the central chord.

1. Introduction

The Large Helical Device (LHD) experiments has successfully started [1,2] after the eight-years of construction period(1990-1997). The major and minor radii of the plasma are 3.6 – 3.9 m and 0.6 – 0.65 m, respectively. The magnetic field up to 3 T is generated by a pair of superconducting helical winding of pitch parameters of $m/l = 2/10$ and three sets of superconducting poloidal coils. The plasma is generated by ECRH of 84 and 82.6 GHz, and heated up by NBI and ICRF [3]. The plasma parameters obtained to date are: the electron/ion temperature of 1.0 - 4.5/3.5 keV, the line-averaged electron density of $< 1.5 \times 10^{20}$ m^{-3} and the maximum stored energy of 1.0 MJ. A multi-channel FIR laser interferometer has been developed [4] for the density profile measurements on LHD. There are no mechanical disturbances caused by the change of the magnetic field in the laser diagnostics which usually need the exact spatial alignment. Here, we shall present the characteristics of the major components of the interferometer and typical experimental results.

2. General Layout of the System

Figure 1 shows a schematic drawing of the interferometer system [4] in the LHD experimental hall, including the other major diagnostics. The FIR lasers are installed in the laser room biologically shielded with thick concrete walls, and their beams are transmitted about 40 m through a couple of the dielectric wave guides (Acrylic resins tubes ~47 mm inner diameter) to reach the optical bench of the interferometer. The optical housing, where ~150 optical components are installed, is mounted on a massive frame. The frame encircles the plasma vacuum vessel and is placed on three pneumatic vibration isolation mounts in order to isolate it from floor vibration. This isolation stand is 18.4 meters tall and weights about 30 tons. The diameter of the three main supports is 712 mm. The upper shelf of the stand supports thirteen corner cube reflectors (75 mm aperture, 1 second accuracy), and the interferometer housing (3900 x 1500 x 4500 mm^3) is supported by the lower shelf, which is located below the floor of the LHD. The optical housing is air tight and filled with dry air in order to reduce absorption of the CH3OH laser radiation by atmospheric water vapor. Z cut crystal quartz etalons are used for the beam splitters, beam combiners and vacuum windows. The measured transmission of the windows (73 mm clear aperture, 2999 μm in thickness) is about 80 %. The each probe beam is focused to a beam waist diameter of 44 mm on the corner cube reflectors. The reflected beams are combined with the local beams and down-converted into I.F. signals (f = 1 MHz) by GaAs Schottky barrier diode mixers mounted on a corner cube reflector. For the detection of the mechanical vibration the He-Ne laser interferometer is equipped at the central chord channel.

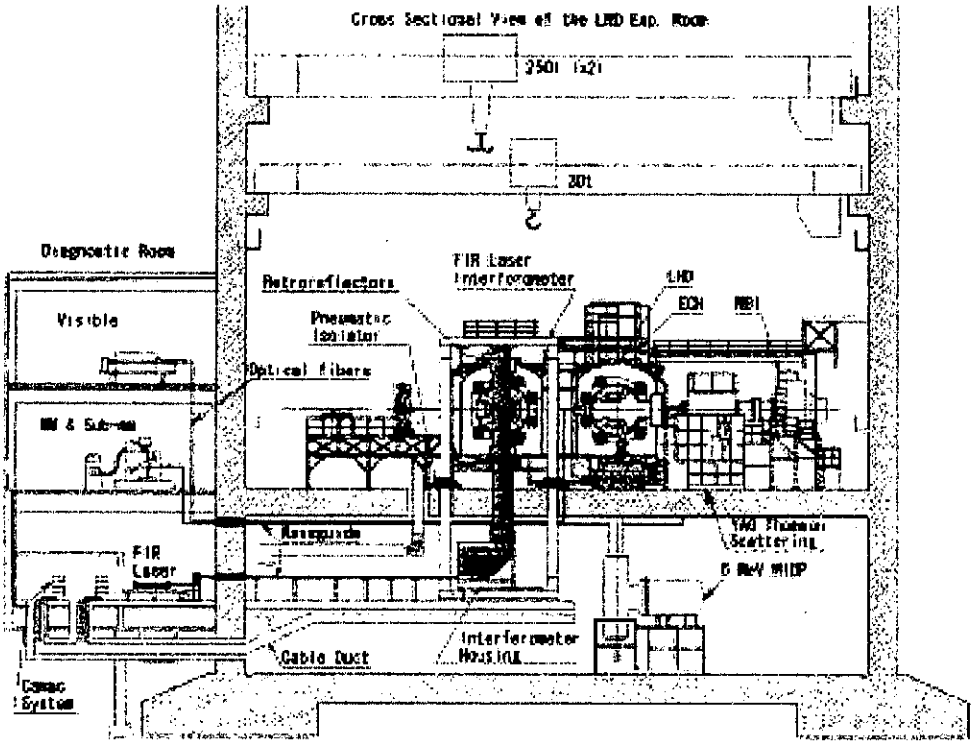

Fig. 1. Cross-Sectional view of the LHD experimental hall.

3. The Laser System

For the interferometry of the LHD plasma, the probing laser wavelength should be smaller than 200 μm in order to avoid the beam refraction effects owing to the plasma density gradient. There are two kinds of laser sources with high power in the FIR wavelength region, 119 μm CH3OH and 195 μm DCN lasers. We have chosen the 119 μm CH3OH laser from the view points of the output power (620 mW), small refraction effect, high beat frequency available and so on. Figure 2 shows the schematic drawing of the laser system we have developed. In the optically-pumped FIR laser, the pump CO2 laser plays important role for output power, laser mode, and stability of the FIR laser oscillation. In order to stabilize the CO2 laser frequency, DC and AC the stark effects of the external CH3OH Stark cell are applied. The twin FIR laser is of the waveguide type, consisting of 35 mm ID Pyrex-glass tubes of 2.2 m in length with coaxial water coolant jacket. The laser cavity are formed by gold coated Cu input couplers with a off-axis 3 mm hole and gold coated Si hybrid couplers with a 13 mm diameter clear aperture. The cavity mirrors are mounted on the base plates made of stainless steel, of which separations are fixed by using two super-invar rod of 25 mm in diameter. The position of the mirror mounts is controlled by stepping motors with the minimum step size of 0.01 μm, which enable us to control the beat frequency within an accuracy of 5 kHz, 0.5 % of the beat frequency (1MHz). The output power can be as high as 680 mW in total, but a typical operation power at the experiments is 250 mW (150 mW for a probe beam and 100 mW for a local beam).

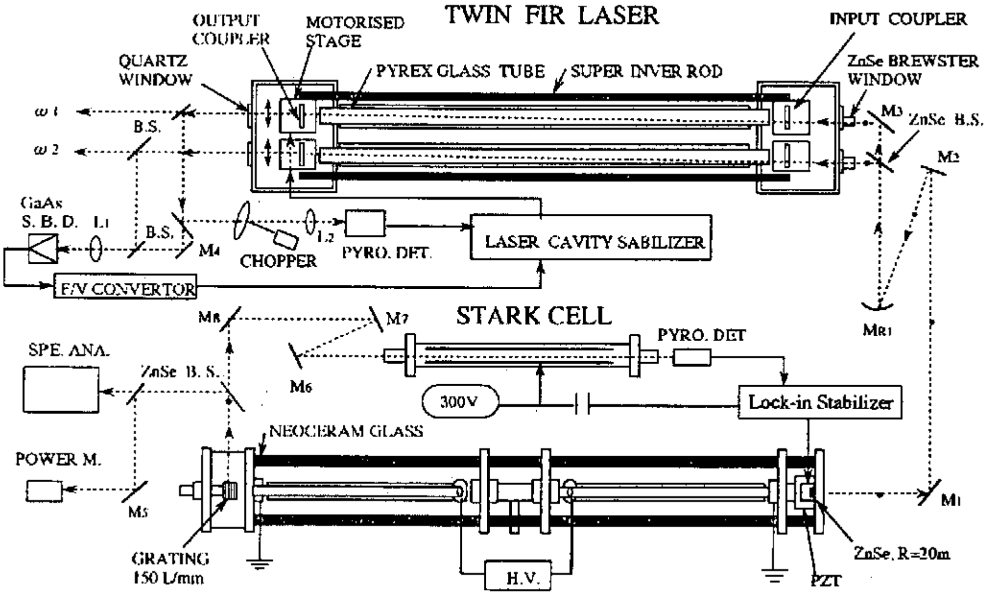

Fig. 2. Schematic drawing of the optically pumped twin FIR laser with a feedback control system

4. Data Acquisition System and Results

The 1 MHz beat signals from the detectors are amplified and converted to TTL signals in the electro-optical converters. For the measurement of the phase difference between the probe signal and the reference one a new type of digital phase linearizer has been developed [5]. The phase linearizer can measure phase shifts up to 640 fringes with an accuracy of 1/100 of a fringe. The size of internal memory is 16 bits – 2 Mwords and the sampling frequency of the waveform data is up to 1 MHz. For real-time phase measurements the phase linearizer has a digital-to-analog converter output, and its output signal has been used for the density feedback control.

Figure 3 shows typical direct output signals of 12 channels when an ice pellet was injected into the LHD plasma. The amplitude of the phase shift due to the mechanical vibrations was measured to be less than 1/100 fringes during the standard duration discharges, so that the compensating interferometer is unnecessary at the present. In order to obtain density distribution, we applied the simple slice and stuck technique for the Abel inversion procedure [6]. Figure 4 shows the time evolution of inverted chordal data for a pellet injected discharge. The observed density profile is hollow one before the pellet injection, and becomes relatively flat just after the injection. The profile keeps the same one for ~100 ms after the pellet is injected, and then changes to the peaked one. A steep density gradient is observed at the peripheral region of the plasma, which often causes the fringe jumps at the corresponding channels when a large sized pellet is injected. In order to solve this problem, shorter wavelength laser sources are under development [7].

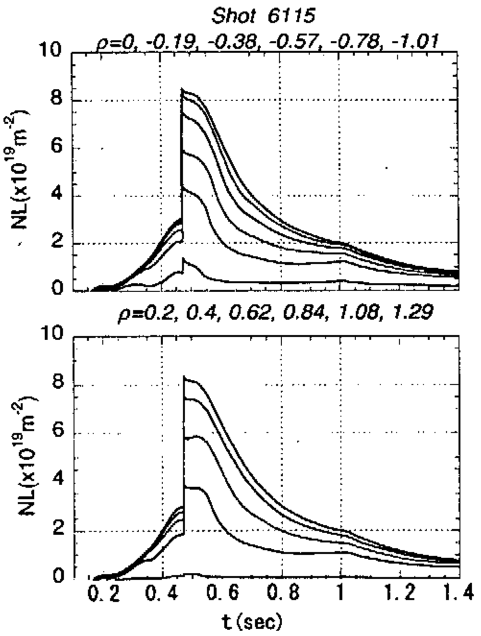

Fig.3. Time behaviors of the line integrated densities.

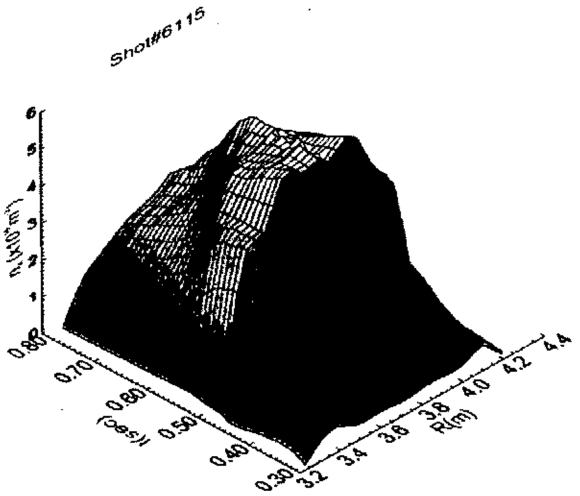

Fig.4. Time evolution of the density profile during ice pellet fuelled discharge.

References

[1] Iiyoshi A., et al., Nuclear Fusion **39** (1999) 1245.

[2] Fujiwara M., et al., Nuclear Fusion **39** (1999) 1659.

[3] Kawahata K., Ohyabu N., et al., Plasma Phys. Control. Fusion **42** (2000) B51.

[4] Kawahata K., Tanaka K., Ito Y., et al., Rev. Sci. Instrum. **70** (1999) 707.

[5] Tokuzawa T., Kawahata K., et al., Rev. Sci. Instrum. **72** (2001) 1103.

[6] Tanaka K., et al. , Proc. of the 26th EPS conference, 1999, Maastricht, 1329.

[7] Okajima S., Nakayama K., et al., Rev. Sci. Instrum. **72** (2001) 1094.

High Power ICRF Heating in LHD in the 4-th Campaign

T. Watari, T.Yamamoto 1), T. Mutoh, R. Kumazawa, T. Seki, K. Saito 1), Y. Torii 1), N. Takeuchi 1), Z.Chen 2), M. Sasao, M. Isobe, M. Osakabe, T. Ozaki, T. Morisaki, , T. Watanabe, S. Murakami, F. Shimpo, G. Nomura, A. Kato, M. Yokota, H. Idei, S. Kubo, K. Ohkubo, M. Sato, T. Shimozuma, Y. Yoshimura, K. Ikeda, O. Kaneko, Y. Oka, Y. Takeiri, K. Tsumori, N.Ashikawa 3), P.C.deVries, M. Emoto, A.Fukuyama 4), H. Funaba, M. Goto, K. Ida, S. Inagaki, N. Inoue, K. Itoh, S. Kado, K. Kawahata, T. Kobuchi, K.Khlopenkov, A. Komori, A. Krasilnikov 5), Y. Liang 3), S. Masuzaki, K. Matsuoka, T. Minami, J. Miyazawa, S. Morita, S. Muto, Y. Nagayama, Y. Nakamura, H. Nakanishi, K. Narihara, K. Nishimura, N. Noda, A. T.Notake 1),S. Ohdachi, N. Ohyabu, H. Okada 4), M. Okamoto, R.O.Pavlichenko, B.J. Peterson, A. Sagara, S. Sakakibara, R. Sakamoto, H. Sasao, , K. Sato, S. Satoh, T. Satow, M. Shoji, S. Sudo, H. Suzuki, M.Takechi, N.Tamura 3), S. Tanahashi, K. Tanaka, K. Toi, T. Tokuzawa, K.Y. Watanabe, H. Yamada, I. Yamada, S. Yamaguchi, S.Yamamoto1), K. Yamazaki, M.Yokoyama, Y. Hamada, O. Motojima, M. Fujiwara

National Institute for Fusion Science, 322-6 Oroshi-cho, Toki, 509-5292 Japan
1) Department of Energy Engineering and Science, Nagoya University, 464-8603, Japan
2) Institute of Plasma Physics, Academia Scinica, 230031, Hefei, Anhui, China
3) Department of Fusion Science, School of Mathematical and Physical Science, Graduate University for Advanced Studies, Hayama, 240-0193, Japan
4) Kyoto University, 606-8187, Kyoto, Japan
5) Troisk Institute for Innovating and Fusion Research(TRINITI), Troisk, Russia

Abstract

This paper reports the results of high power ICRF heating experiments in the LHD conducted in the 4th campaign in 2000. During this campaign 2.7 MW of ICRF power injection became possible with increased numbers of ICRF antennas and reinforcement of the RF power amplifiers. ICRF heating power was added to NBI heating power and expanded the range of operational power. ICRF heating was also applied to low BT plasmas in high beta experiments where principles of second harmonic heating was proved. In the long pulse experiment, a 2-minutes duration of ICRF was attained.

Introduction

The ICRF heating experiment in the 3rd campaign in 1999 demonstrated its viability in helical systems by successful 1.35MW power injections [1-4] and by a 1 minute long pulse operation [2]. The importance of high energy particle confinement in ICRF heating being well realized [5,6], these results are taken as suggesting that the heliotron devices are furnished with good confinement properties of trapped ions. A specific interest arising here is to what power the high performance of the ICRF heating is maintained. The power sources were reinforced in the 4-th campaign to facilitate an examination of the ICRF heating in a higher power regime. The experiment began with survey of the heating performance in various magnetic configurations, by means of changing magnetic field strength, gamma value, magnetic axis position, and quadrupole component. Finally, the injection power reached maximum of 2.7MW and significant deterioration has not been observed. ICRF heating contributed in various LHD experiments as useful power added to NBI, and new regimes of ICRF heating were explored.

1) Highest Stored Energy

ICRF heating was conducted in minority heating regime with H minority ions and He bulk ions. In Fig.1, the locations of cyclotron layer, cut-off layer and two- ion-hybrid layer are shown. It was confirmed in the experiment that the best heating is obtained at BT =2.75T with fixed frequency of 38.47MHz as confirmed in the previous experiment [4]. The dependence of the performance of ICRF heating on the magnetic axis was investigated in this campaign. The heating result with R=3.6m was found better than that obtained with R=3.75m, which agree with the previously report. Due to the improvement of the antennas and power sources, ICRF injection of 2MW power level was realized with good reproducibility.

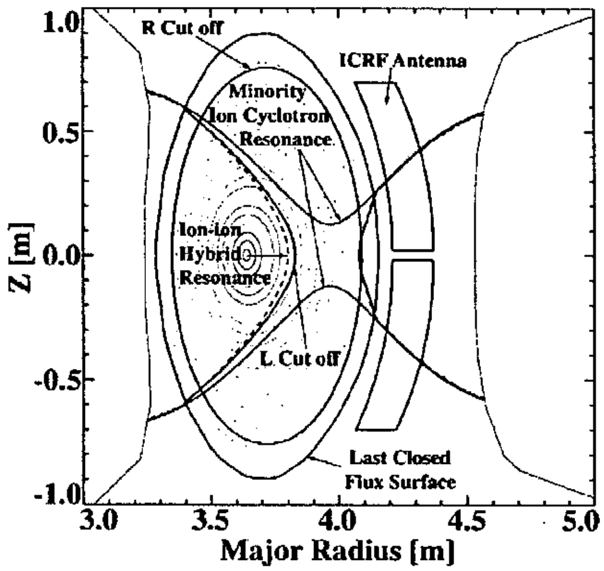

Fig.1 The resonance and cutoff diagram in the optimum heating regime. The antenna is located in the toroidal section where plasma cross section is vertically elongated. In front of the antenna, there is a region where magnetic field has weak non-uniformity.

In the shots with ICRF power only, a new record stored energy of 240kJ was obtained and maximum operational density of $3\times10^{19}m^{-3}$ was attained.

In the highest stored energy shot shown in Fig.2, ICRF power was added to 5 MW NBI power. The stored energy was boosted up above 1 MJ by addition of 100 kJ. The shot was obtained with pellet injection and at the maximum energy the density is around $1\times10^{20}m^{-3}$ indicating that ICRF heating works well at such very high plasma density. In this shot with pellet injection, He ions may be mostly replaced by H ions and, therefore, ICRF heating is supposed to be working at heavy minority ion heating regime.

2. Long Pulse Operation

In the long pulse experiment, ICRF power sustained the plasma for two minutes. It is a new record doubling previous one obtained in the 3rd campaign. As shown in Fig.3, operational plasma density is $0.9\times10^{19}m^{-3}$ and applied power is 0.4MW. Electron and ion temperatures are same, 1.3keV. The radiation loss was kept to low level facilitating the long pulse shot. Feed back control of gas puffing was applied for it is important to keep the plasma density in proper range.

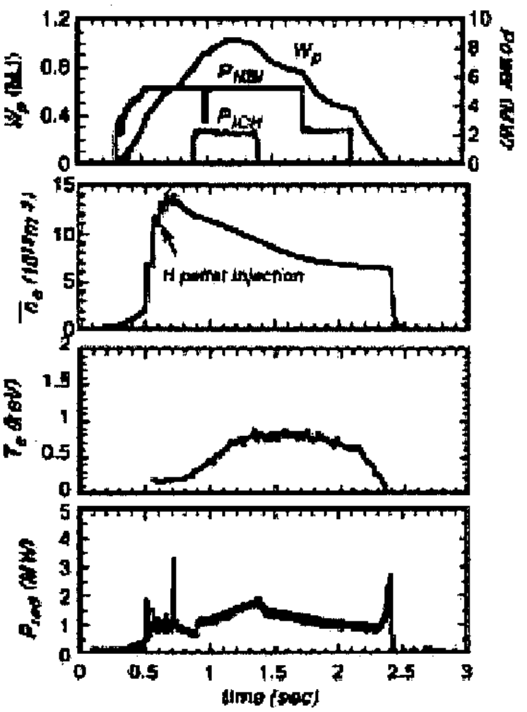

Fig.2 The highest energy shot.

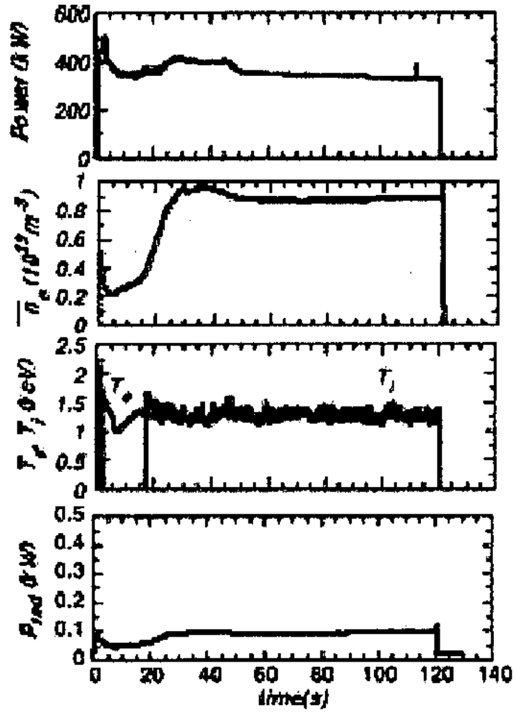

Fig.3 The longest pulse shot.

3. Second Harmonic Heating

ICRF heating was used in high beta experiments added to NBI. With frequency of 38.47 MHz, the ICRF heating is in the second harmonic heating regime with BT~1.3T. As shown in Fig. 4, operational plasma density is about $4\times10^{19}m^{-3}$ and electron temperature is about 0.6keV. The stored energy increases by about 50 kJ with the superposition of ICRF. High energy protons up to 150keV have been observed as measured with diamond FNA detector [7,8]. This shot demonstrates utility of second harmonic heating. Heating efficiency is around 0.5 and it increases with increasing beta value as theories predict. Therefore, this heating regime will improve its performance in experiments with higher power particularly in use in high beta experiments.

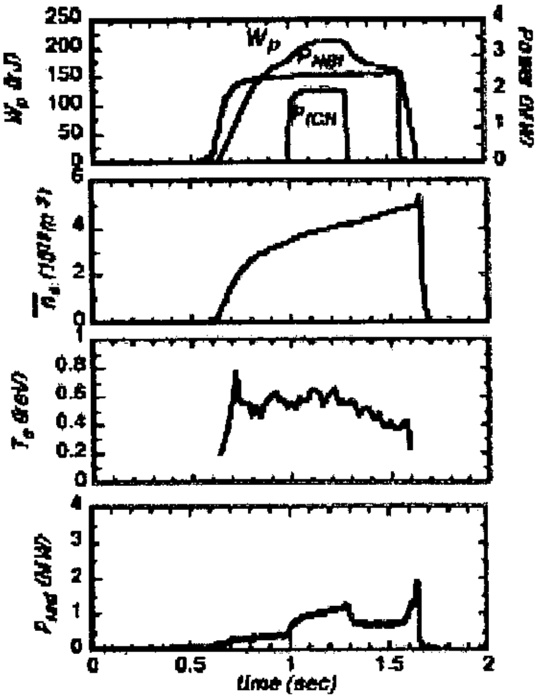

extremely high energy ions, this shot may signify favorable high energy particle confinement. Since second harmonic heating is known to create t of LHD adding to the previous results obtained for fundamental heating [1].

Fig.4 ICRF applied to high beta experiment: The best performance of 2nd harmonic heating is obtained with BT=1.375T, half the optimum BT(=2.75T) for the fundamental heating. The second harmonic layer has the same shape as the fundamental layer shown in Fig.1.

References

[1]MUTOH, T., et al., Phys. Rev. Letters,85(2000)4530
[2] KUMAZAWA, et al., Physics of Plasmas, 8(2001)2139
[3]SEKI, T., et al., J. Plasma and Fusion Research (Proc. 10th Toki Conf., 2000), JSPS&NFR,
[4]SAITOH, K. et al., ""Ion and Electron Heating in ICRF Heating Experiments on LHD", Nuclear Fusion, in print
[5]WATARI, T., , Plasma Phys. Control.Fusion, 40(1998)A13
[6]MURAKAMI, S., et al., Nucl. Fusion, 39(1999)1165
[7]KRASILNIKOV, A.V., et al., Nuclear Fusion, 39(1999)1111
[8]SASAO, M., "Study of Energetic Ion Transport in the Large Helical Device", IAEA Conference, 2000, Sorento, (EX9/1)

Bolometric Imaging of Radiative Structures on the Large Helical Device

N. Ashikawa*, B. J. Peterson[a], S. Sudo[a], A. Yu. Kostrioukov[a], Yuhong Xu[a],
M. Shoji[a], M. Osakabe[a] , T. Watanabe[a] and the LHD Experimental Group[a]

Graduate University for Advanced Studies, Toki-shi, 240-0193, Japan
[a]National Institute for Fusion Science, Toki-shi, Gifu-ken 509-5292, Japan

1. Introduction

The infrared (IR) imaging bolometer (IRIB) is a new type of plasma radiation measurement system, which uses an IR camera [1, 2]. The IRIB uses a foil sandwiched between two identical masks to absorb the plasma radiation. The increase in the foil temperature due to the radiation is measured with an IR camera. The key feature of the IRIB is that using readily available IR imaging technology, a measurement of 2-dimensional spatial radiation profiles is very easy. Previously two types of IRIB ware tested on the Large Helical Device (LHD) which are the Segmented Mask Imaging Bolometer (SIB) [3] and the Infrared Imaging Video Bolometer (IRVB) [4]. In this paper we demonstrate the ability of the IRVB to display the helical structure of the plasma radiation in LHD by comparing an IRVB image with a corresponding image of CIII light and the structure of the chaotic magnetic field lines in the ergodic region.

2. IR Bolometer system on LHD

The Large Helical Device(LHD) is a large-scale superconducting heliotron system with a set of l/m =2/10 helical coils [5]. The data shown in this paper comes from a discharge with the parameters R_{axis} = 3.6 m, B_t=2.88 T, and $n_e = 9 \times 10^{19}/m^3$. The IRVB used in this study provides a 10 x 14 pixel image of the plasma radiation with a sensitivity of 0.5 mW/cm^2 and a time resolution of 67 ms [4]. Figure 1 shows the field of view (FOV) of the IRVB installed at a tangential port on LHD. The yellow line indicates the horizontally elongated cross-section and the red line shows the more distant vertically elongated cross-section. The light blue rectangle shows the FOV of the IRVB determined from the pinhole position and size of the foil. The FOV is slightly blocked by the vacuum vessel and another diagnostic shown in black and light blue. Comparison with the IRVB emissivity image in Fig. 2 shows plasma radiation coming from the unblocked portions of the FOV.

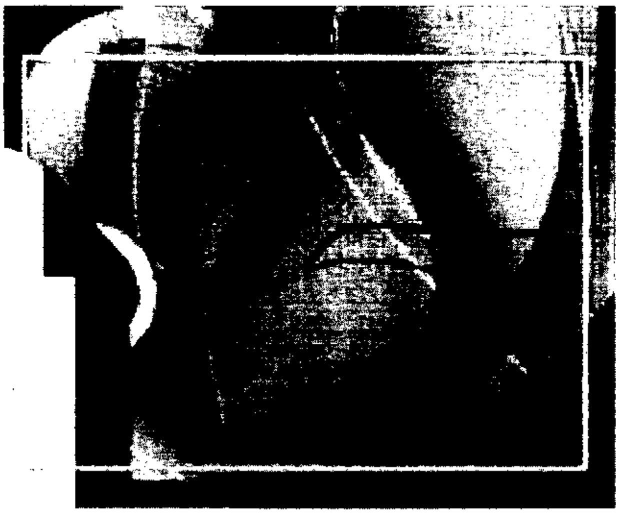

Figure 1 CAD drawing of field of view(inside blue line) of IRVB at tangential port on LHD.

3. Comparison of edge magnetic field lines and IRVB data

In the absence of heavy impurities the radiation profiles should be hollow and the bulk of the radiated power should come carbon radiating from the ergodic region of the plasma outside the last closed flux surface. Figure 3 shows the field line calculation as viewed from the tangential port on LHD [6]. Each blue point indicates a field line launched in the region just outside the last closed magnetic surface ($\rho = 1$). Therefore brighter blue regions indicate regions where the IRVB has a more

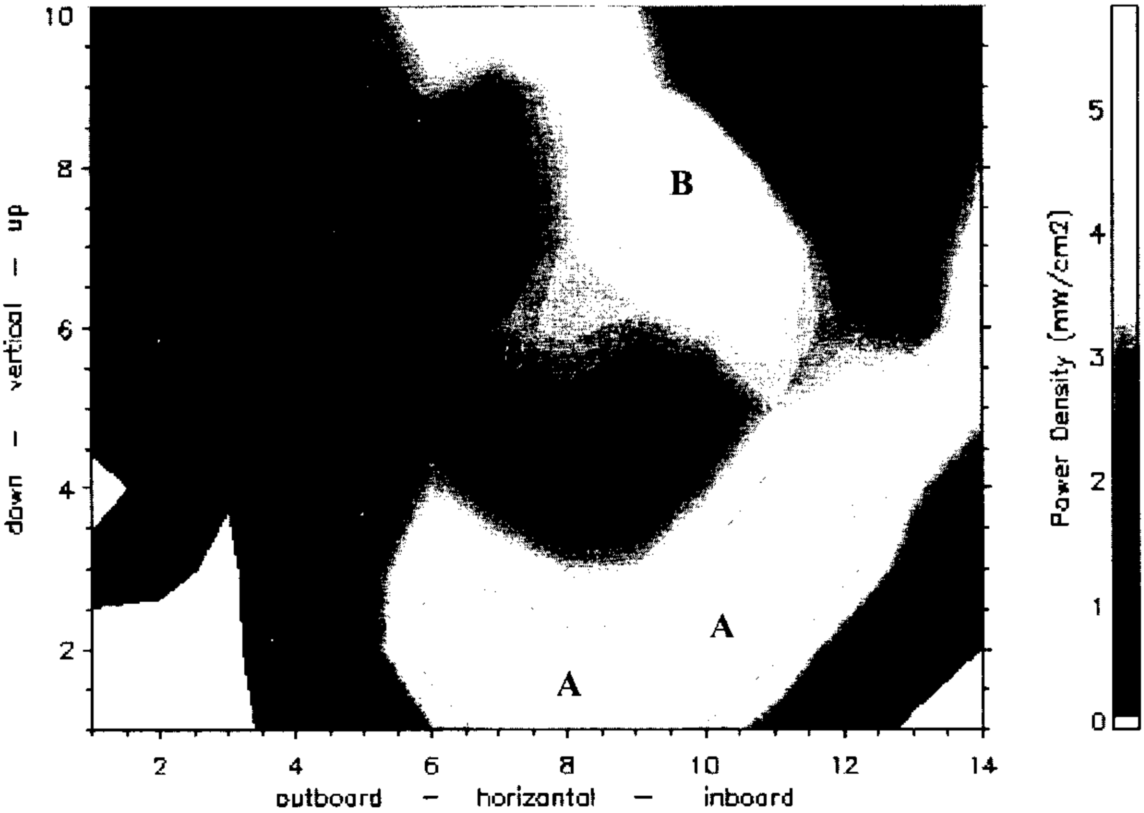

Figure 2 Image of two-dimensional radiation from tangentially viewing IRVB at t = 0.99 s for LHD shot # 20744.

tangential view of the edge chaotic region and should correspond to areas of more intense radiation. However the effects of solid angle are not included in the calculation, therefore the portions of the plasma which are far from the detector and would radiate less brightly are given the same weight as those near the detector that radiate more strongly. But Fig.3 very clearly shows the helical structure of the chaotic edge region as viewed by the IRVB.

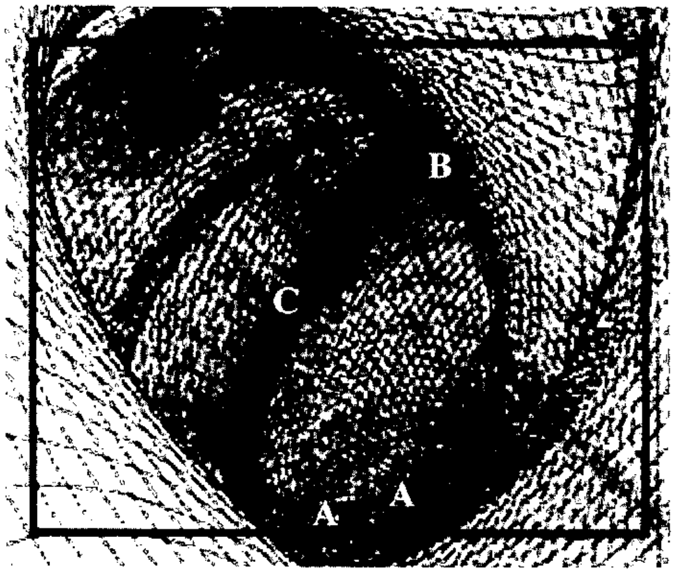

Figure 3 Magnetic field lines (light blue) in the ergodic region (with IRVB field of view indicated by dark blue line).

Comparison between the IRVB data and these magnetic field lines shows the strong helical structure of the plasma radiation predicted by the magnetic structure. In particular the broad radiative structure observed in the lower portion of the field of view (indicated by A) is very bright partly due to the fact that it lies in the near field of the IRVB. The bright region in the upper portion of the IRVB image corresponds to the location where two dense regions in the magnetic field line calculation overlap as indicated by point B. The structure seen in the center of the field of view in Fig. 3 (indicated by C) is not so clear in the IRVB image in Fig. 2, which may be understood by comparison with the image from a CCD camera filtered for CIII radiation.

4. Comparison of the imaging bolometer data and the CIII radiation image

A simultaneous image from a CCD camera using a CIII filter and having nearly the same view of the

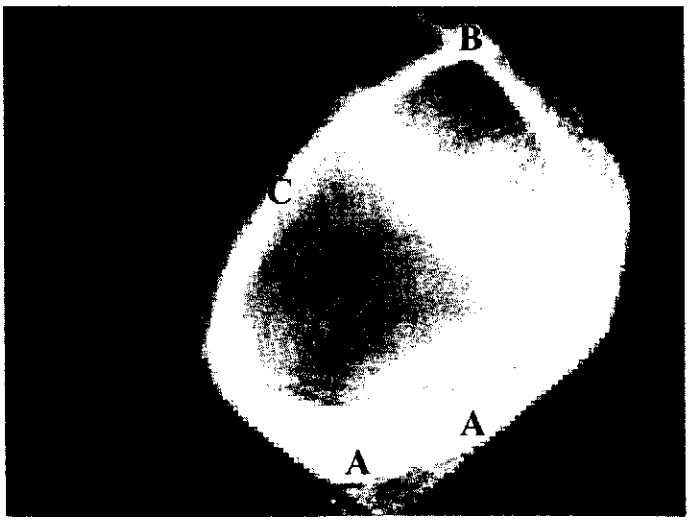

Figure 4 Image of CIII radiation from tangentially viewing CCD camera at t = 0.99 s for LHD shot # 20744.

plasma is shown in Fig. 4. Since carbon is the main impurity and mainly radiates from the edge, it should give an image similar to that of the IRVB. Comparison of the images shown in Figs. 2 and 4 show very similar features. The structures indicated by A and B are both clearly seen in both images. However the structure indicated by C is not so clear in the bolometer image as was mentioned above. This may be due to the thinness of the structure and the relatively poor spatial resolution of the IRVB compared to the CCD camera.

5. Summary

Good qualitative agreement is observed in the comparison of the bolometric image with a corresponding image from a CCD camera filtered for CIII light and with the magnetic field lines of the chaotic edge region outside of the last closed magnetic surface. This demonstrates that the IRVB can clearly show a two-dimensional image of the three-dimensional helical structure of the radiation from LHD. The next step in this research and development program is to carefully calibrate, install and bring into operation two additional imaging bolometers at upper and lower ports viewing the same plasma volume as that seen with the tangential IRVB. The data from these three imaging bolometers will then be used to attempt the first three-dimensional tomography of plasma radiation.

Acknowledgements

This work is supported by Hayashi Memorial Foundation for Female Natural Scientists.
The authors would like to thank Director General M. Fujiwara and Prof. O. Motojima for their continuing support and encouragement of this work.

References

[1] G. A. Wurden, B. J. Peterson and S. Sudo, *Rev. Sci. Instrum.* **68** (1997) 766.

[2] B. J. Peterson, *Rev. Sci. Instrum.* **71** (2000) 3696.

[3] N. Ashikawa, B. J. Peterson *et al., J. Plasma Fusion Res. SERIES* **3** (2000) 436.

[4] B. J. Peterson, N. Ashikawa *et al., Rev. Sci. Instrum* **72** (2001) 923.

[5] O. Motojima *et al., Phys. Plasmas* **6** (1999) 1843.

[6] T. Watanabe and H. Akao, *J. Plasma and Fusion Res.* **73** (1997) 186 (in Japanese).

TANGENTIAL POLARIMETER
FOR ELECTRON DENSITY DIAGNOSTICS ON LHD

T. Akiyama[1], S. Tsuji-Iio[1], R. Shimada[1], K. Nakayama[2], S. Okajima[2],
K. Tanaka[3], K. Watanabe[3], and K. Kawahata[3]

[1]*Research Laboratory for Nuclear Reactors, Tokyo Institute of Technology*
2-12-1 O-okayama, Meguro-ku, Tokyo 152-8550, Japan
[2]*Chubu University,* [3]*National Institute for Fusion Science*

1. Introduction

In a magnetized plasma the Faraday rotation angle, α, in radians is given in SI units by

$$\alpha = 2.62\times10^{-13}\lambda^2 \int n_e B_{//} dl$$

where λ is the wavelength of the probing beam, n_e is the electron density, $B_{\|}$ is the magnetic strength parallel to the probing beam axis. While polarimeters were originally developed for magnetic strength measurements, in recent years polarimeters for density monitor were proposed and demonstrated [1, 2] because of its several advantages over intereferometers. The mechanical vibrations principally less affect polarimeters, so that it is suited for long-pulsed operation. In addition, by selecting CO_2 laser it is possible to suppress the refraction of the probing beam and to avoid "fringe jump" errors even in the high density plasma with a simple optical setup. Hence CO_2 laser polarimeter is a robust and promising electron density measurement method. Furthermore we aim at the polarimeter not only to monitor an electron density but also to measure the density profile. For these purposes we developed a tangential 3-channel CO_2 laser polarimeter based on the polarization rotation method using frequency-shift heterodyne technique [3].

2. Optical layout

Figure 1 shows the illustration of the optical setup of the polarimeter on the Large Helical Device (LHD). The laser beam is split into two and they are modulated by two acousto-optics modulators (AOMs) at different drive frequencies. As a result they have a modulated frequency difference of 90 kHz. A half-wave plate in the one of beam path make the two beams perpendicularly to each other and then they are re-combined. Then a quarter-wave plate makes the orthogonal beams counter-rotating circularly polarized ones. As illustrated in Fig. 1 the combined beam becomes linearly polarized beam rotating at a half of

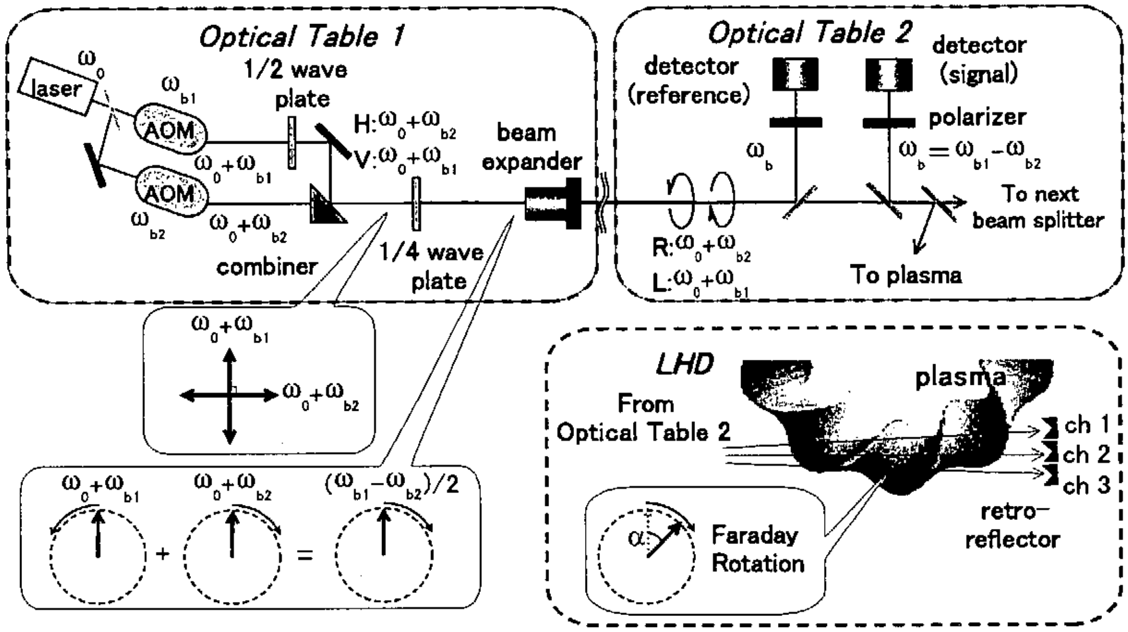

Fig. 1: Schematic of the optical setup and polarimetric method. Probing beam is split into three by beam splitters and the one of three channels is shown in optical table 2.

the modulated frequency difference. The probing beam is split into three by beam splitters on Optical Table 2. They are injected into the LHD plasma tangentially and return with vertical displacements around 40 mm with retro-reflectors installed inside the vacuum vessel. The beat frequency of detected signals is 90 kHz and the rotation angle by the plasma is measured as the phase difference between reference and probing signals. Since the magnetic strength can be computed accurately at least in the case of low β operation of helical devices such as LHD, we can evaluate the electron density from the Faraday rotation angle.

3. Experimental results

To extract the phase difference with a high angle resolution we adopted the digital complex demodulation [2] combined with digital band-pass filtering. Therefore the time response depends on the band-width, Δf. Figure 2 shows the Faraday rotation angle resolution that is defined as the standard deviation of the 2-s long phase difference signal without plasma as a function of the response time. The resolution of the Faraday rotation angle was 0.01 deg. , which corresponds to 5.0×10^{17} m^{-3} at $\boldsymbol{B}$ = 3 T with a response time of 3 ms was achieved. The SN ratio of the phase difference signal mainly depends on noises at low frequencies lower than 500 Hz. We presume that small movement of the detector against the laser beam by mechanical vibrations caused such phase noises because it is difficult to align the counter-rotating circularly polarized beams completely collinearly along all the beam path, whose length is about 30 m. Although mechanical vibrations do not affect the polarimeter seriously like an interferometer, the reduction of vibrations would work well for better

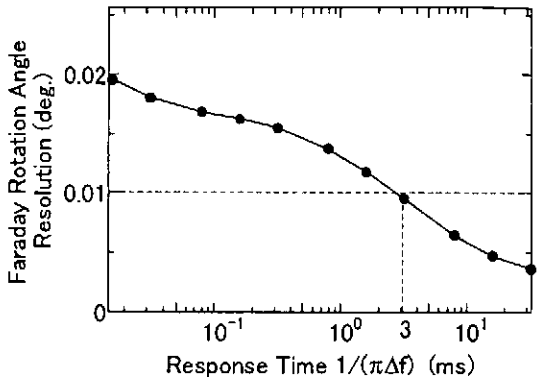

Fig. 2: The Faraday rotation angle as a function of the response time determined by the band-width of the digital filter Δf

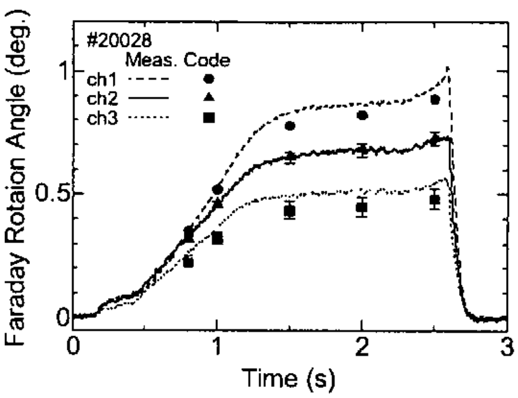

Fig. 3: Comparison with the calculated rotation angle using the density profile by the Able inversion of the FIR interferometer data

resolution. The base line of the rotation angle fluctuates with amplitudes up to 0.05 deg. in several seconds and this is a problem in the case of the low density plasma. We speculate that the incompleteness of the beam alignment also leads to the fluctuations.

The elliplization of circularly polarized beams due to the Cotton-Mouton effect and the incompletely polarization-insensitive characteristics of optical components break the linearity between the Faraday rotation angle and the measured phase difference. The Cotton-Mouton effect along the beam path is negligibly small, so that we did calibration by adding a half-wave plate in front of polarizers to simulate the Faraday rotation.

To evaluate the accuracy of measured Faraday rotation angle, we compared it with the calculated one using the density profile from the 13-ch FIR interferometer data and the magnetic strength whose the β value is close to the one from diamagnetic measurement (Fig. 3). Since the tangent radius of each channel was calculated from the manually measured length between the probing beam and weight hanged from the upper port whose coordinate was known, it contains errors. The constructional error is about a few centimeters, so that we assumed the error of the tangent radius is ±3cm and computed the rotation angle within error bars. As a result, the rotation angle of each channel was found to be consistent with the interferometer data. The reason why the error bars of ch 3 is larger than other ones is that the probing beam of ch 3 passes the region where the path length in the plasma sharply declines against the tangent radius of the probing beam because of the helical shape of the LHD plasma.

Even in the case of pellet injected plasmas, where FIR interferometers often suffer from fringe jumps, it was demonstrated that the polarimeter could measure the time evolution of the Faraday rotation successfully as shown in Fig. 4. The rapid change in the Faraday

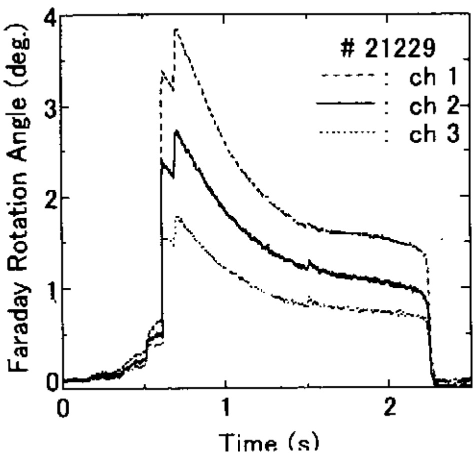

Fig. 4: The measured Faraday rotation angle of a pellet injected plasma

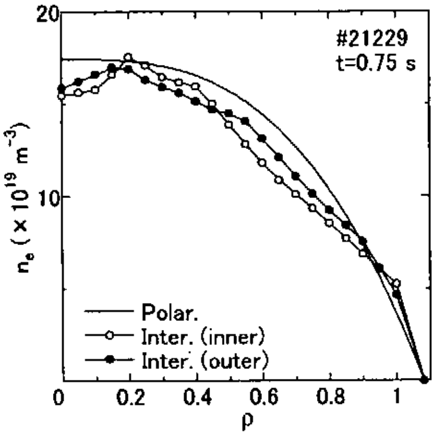

Fig. 5: The density profile estimated from the Faraday rotation angle

rotation angle could be measured with enough resolution and reliability. Figure 5 shows the electron density profile after the pellet injection in the shot of Fig. 4 estimated from the polarimeter data. Here, we used the β value, which affects the rotation angle, from diamagnetic measurement and calculated iteratively assuming the profile is parameterized as:

$$n_e(\rho) = a(\rho^2 - \rho_{BC}^2) + b(\rho^3 - \rho_{BC}^3)$$

where ρ is the normalized magnetic flux radius and ρ_{BC} is the plasma boundary radius. Open marks and closed marks are result of the Abel inversion of the FIR interferometer inner and outer channel data that is corrected the fringe jump error manually. The profile from the polarimeter is almost consistent with the FIR interferometer. This result substantiates polarimeters have the feasibility of the electron density profile measurements.

4. Conclusions

The reliability of a CO_2 laser polarimeter was demonstrated even during the pellet injected plasma operation and an angle resolution of 0.01 deg. with a response time of 3 ms was achieved. Considering errors in the tangent radius, all the channels were consistent with the FIR interferometer. We estimated the density profile after pellet injection from the polarimeter data and it was consistent with the density profile from the interferometer data, which fringe jump error was corrected.

Reference

[1] F. C. Jobes, D. K. Mansfield: Rev. Sci. Instrum. **63**, 5154 (1992).

[2] Yasunori Kawano, Shin-ichi Chiba, Akira Inoue: Rev. Sci. Instrum. **72**, 1068 (2001).

[3] T. Akiyama, E. Sato, T. Nozawa *et al*: Rev. Sci. Instrum. **72**, 1073 (2001).

[4] Y. Jiang, D. L. Brower, L.Zeng, and J. Howard: Rev. Sci. Instrum. **68**, 902 (1997).

Impurity Behavior in LHD Long Pulse Discharges

Y. Nakamura, Y. Takeiri, B. J. Peterson, S. Muto, K. Ida, H. Funaba, M. Yokoyama,
K. Narihara, Y. Nagayama, S. Inagaki, T. Tokuzawa, S. Morita, M. Goto, K. Sato,
M. Osakabe, S. Masuzaki, H. Suzuki, R. Kumazawa, T. Mutoh, T. Shimozuma, M. Sato,
N. Noda, K. Kawahata, N. Ohyabu, O. Motojima and LHD experimental groups

National Institute for Fusion Science, 322-6 Oroshi-cho, Toki 509-5292, Japan

Introduction

Impurity control is one of the important issues for realizing a fusion reactor. While many experiments on impurity transport have been performed in tokamaks and stellarators with short pulse discharges, few experiments have been done with long pulse discharges, in particular, on stellarators. Therefore, impurity behavior was investigated in long pulse discharges on LHD, which is a superconducting large helical device. In a variety of long pulse discharges [1-4], we found that metal impurity accumulation was observed in only hydrogen discharges in a narrow density window of around 2 x 10^{19} m^{-3}. Spectroscopic and soft x-ray measurements show an increase of radiation from metal impurities (mainly iron). A significant increase of core radiation was observed in radiation profiles from bolometry measurements. In this paper, the impurity behavior in NBI heated long pulse discharges will be reported and the density dependence will be discussed with neoclassical impurity transport in the core plasma.

Impurity behavior in long pulse discharges

Figure 1 shows a typical long pulse discharge with impurity accumulation and pump-out. A remarkable increase of central radiation (r = 0) is observed despite of almost constant radiation level at the peripheral region (r = 0.945) in the first half period of the discharge. Then the central radiation decreases gradually with time during the constant gas puffing. Clear evidence of impurity accumulation was observed in a peaked profile of radiated power density. Spectroscopic and soft x-ray measurements indicate that the main metallic impurity is iron, which is an element of the plasma wall material. In the high-density region ($\bar{n}_e > 3\times10^{19} m^{-3}$), the central radiation decreases despite of the density increase and the radiation profile tends to return to a hollow one. This implies that the metallic impurities accumulated in the core region are pumped out in the high-density region.

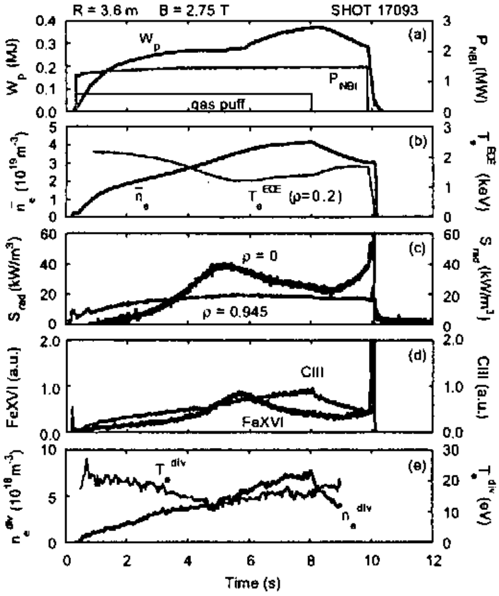

Fig. 1 A typical long pulse discharge with impurity accumulation and pump-out.

The accumulation behavior was also observed in long pulse discharges keeping the plasma density constant. Figure 2 shows the time evolutions of central radiated power density and the most prominent metallic emission (FeXXIII), which originates from the central region of the plasma, for the discharges with different plasma densities. Remarkable temporal increases of the central radiation and the iron line emission were found for only the discharge with $\bar{n}_e = 2.7 \times 10^{19} m^{-3}$. Strong core radiation was also observed.

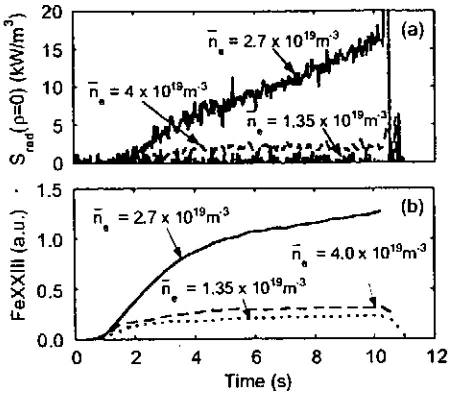

Fig. 2 Time evolutions of (a) central radiation and (b) FeXXIII emission for the discharges with constant densities.

Assuming that the corona equilibrium can be used for high-Z ions (Fe) in the plasma core, the total impurity density was estimated from the radiation emissivity $Q_{rad} = n_e n_I L_I(T_e)$, where n_I is the total density of impurities and $L_I(T_e)$ is the so-called cooling rate. Figure 3 shows the time evolution of central iron density obtained from the radiation emissivity (r = 0), together with a metallic impurity line emission (FeXVI) viewed along the central chord of the plasma. To estimate the radial profile of iron density, we investigated the intensity of the FeXVI emission using the profiles of electron temperature and density, coupled with the impurity transport code (MIST). The central concentration of iron is given by the iron density in Fig. 3(b). The radial profile of total impurity density and the charge state distribution can be calculated by giving the diffusivity and the convection velocity of impurities in the MIST code. In the initial stage of the discharge, the profile of iron density is supposed to be approximately flat. Therefore, we fixed a flat profile of iron density at t = 1.5 s and determined the density profiles at t = 5 and 7.3 s so that the FeXVI emission satisfied the ratio of the intensity measured at each time. Figure 4 shows the radial profiles of iron density at different times of the discharge. A remarkable peaked profile of iron density is observed at t = 5 s and the profile returns to a flat one at t = 7.3 s. This implies that the metallic impurities are accumulated in the density range of $\bar{n}_e = 1 \sim 2.5 \times 10^{19} m^{-3}$ and pumped out in the higher density region.

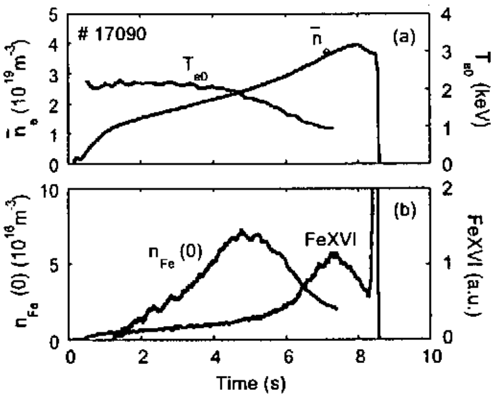

Fig. 3 Time evolutions of central iron density and the Fe XVI emission originating from the peripheral plasma.

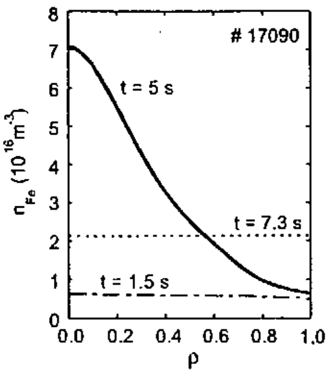

Fig. 4 Radial profiles of iron density at different times for the shot 17090.

Neoclassical analysis of impurity transport

The radial impurity flux was investigated for various collisionality regimes. For the case of low collisionality (low density and high temperature), the impurity flux is given by [5]

$$\Gamma_I = -D_S n_I (n_I'/n_I - Z_I E_r/T_I + \alpha T_I'/T_I) \qquad (1)$$

where D_S and E_r is the diffusivity and the radial electric field, respectively, and α is a collisionality dependent factor. If the impurities are in a regime of $1/\nu$ or collisionless detrapping, the flux is dominated by the term due to the electric field, in particular, for high-Z impurities. The formation of E_r is determined from an ambipolarity condition for the radial fluxes of electrons, ions and impurities. If the electron flux is the dominant flux in a very low collisionality regime, the ambipolar electric field becomes positive (electron root). In this case, the impurity flux tends to go outward. When the collisionality increases, the ion flux becomes dominant and the electric field turns to be negative (ion root). Then the impurity flux tends to go inward. For the case where the impurities are in the plateau regime and the ions in the banana regime, the impurity flux is given by

$$\Gamma_I = -D_{BP} n_I (n_I'/n_I + 3T_I'/2T_I - Z_I n_i'/n_i - 3Z_I T_i'/2T_i) \qquad (2)$$

based on neoclassical transport for axisymmetric devices [6]. For high-Z impurities, the flux is dominated by the last two terms, which drive the impurities inward because n_i' and T_i' are generally negative. When the plasma density increases, the impurities enter in the Pfirsch-schlüter regime with high collisionality. If only the interaction of heavy impurities with the background ions is important, the impurity flux is written as

$$\Gamma_I = -D_{PS} n_I (n_I'/n_I - T_I'/2T_I - Z_I n_i'/n_i + Z_I T_i'/2T_i) \qquad (3)$$

In this regime, the last two terms also dominate the impurity behavior. The density term is directed towards the plasma axis and is responsible for peaking of the impurity density. The temperature term is of the opposite sign and prevents such a peaking, i.e. is responsible for the so-called 'temperature screening'. In LHD, since the density profile is flat or hollow in the discharges with gas puffing and the temperature profile is nearly parabolic, the impurity flux tends to go outward in the plasma core and it leads to a flat profile of the impurity density.

By taking into account the various impurity transport regimes described above, one can see the impurity behavior in a n-T diagram as shown in Fig. 5, where the plasmas with impurity accumulation (closed circles) are distinguished from those without accumulation and with pump-out (squares). The solid line represents the transition between the plateau regime and the Pfirsch-schlüter regime for iron impurity. This boundary is calculated in consideration of the collision with light impurities (C, O), whose concentrations are determined so that Z_{eff} has the value of about 2.5 obtained in the experiments on LHD. The broken line represents the transition between the electron root and the ion root for background plasma. This indicates a critical point of the specific space where the plasma has multiple solutions for the ambipolar electric field. The point was calculated by an analytical model [7] with the typical profiles of temperature and density measured in long pulse discharges at $\rho = 0.2$. On the whole, the impurity behavior obtained in long pulse discharges is qualitatively in agreement with the neoclassical impurity transport. In the low density and high temperature region, the high-Z impurities may be expelled by the positive electric field or diffused out because of nearly zero electric field. As indicated in Fig. 5, it is not so easy to obtain the electron root in the plasma core, but it is possible to obtain in the peripheral region [8]. Furthermore, small positive electric fields were observed even in the density range of ion root near the transition to electron root [8]. The boundary of impurity accumulation in the low collisionality regime may be shifted to higher collisionality regime. In the intermediate regime with negative electric field (ion root), the high-Z impurities are accumulated in the central plasma due to the electric field in the 1/ν regime or the temperature gradient in the plateau regime. When the impurities enter in the PS regime, the accumulated impurities are pumped out by the dominant contribution of the temperature gradient term on account of the flat density profile and the parabolic temperature profile. If the plasma density is raised up quickly, impurity accumulation does not occur because of the temperature screening effect in the PS regime.

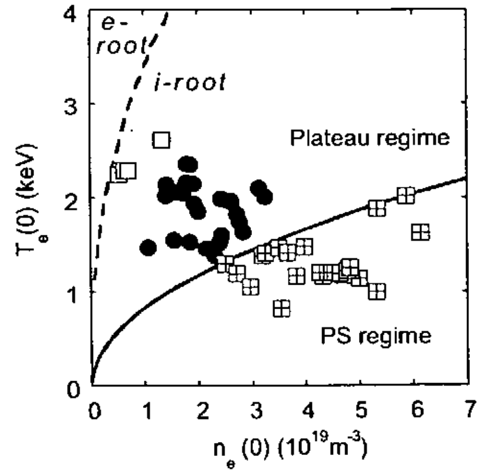

Fig. 5 A n-T diagram for impurity behavior in long pulse discharges. The closed circles indicate the plasmas with impurity accumulation and the open squares indicate the plasmas without accumulation. The squares with a cross indicate the plasmas with pump-out or without accumulation.

Conclusions

Accumulation behavior of high-Z impurities has been observed in NBI heated long pulse discharges with constant density on LHD. The intrinsic metallic impurities (mainly iron) were accumulated in a specific range of the operational plasma density. For density ramp-up discharges, impurity accumulation and pump-out were observed during the discharge and a clear density window for accumulation was found. Neoclassical analysis shows that the radial impurity flux is dominated by the convection component, which changes the sign (inward or outward) for different transport regimes. The observed impurity behavior is in qualitative agreement with the neoclassical impurity transport.

References

[1] Y. Takeiri, Y. Nakamura et al., Plasma Phys. Control. Fusion **42** (2000) 147.
[2] Y. Nakamura et al., J. Nucl. Mater. **290-293** (2001) 1040.
[3] N. Noda, Y. Nakamura et al., Nucl. Fusion **41** (2001) 779.
[4] B. J. Peterson, Y. Nakamura et al., Nucl. Fusion **41** (2001) 519.
[5] K. C. Shaing, Phys. Fluids **26** (1983) 3164.
[6] S. P. Hirshman and D. J. Sigmar, Nucl. Fusion **21** (1981) 1079.
[7] M. Yokoyama et al., submitted to Nucl. Fusion.
[8] K. Ida et al., Phys. Rev. Lett. **86** (2001) 5297.

MEASUREMENT OF SHAFRANOV SHIFT WITH SOFT X-RAY CCD CAMERA ON LHD

Y. Liang, K. Ida, S. Kado[1], K.Y. Watanabe, S. Sakakibara, M. Yokoyama, H. Yamada,
and LHD experimental group
National Institute for Fusion Science, Toki 509-5292, Japan
[1]The University of Tokyo, Tokyo 113-8656, Japan

The major radius of the plasma magnetic axis was derived from the two-dimensional profile of x-ray intensity measured with soft x-ray CCD camera in Large Helical Device (LHD). The measured Shafranov shift increases linearly up to 28cm, which is 47% of minor radius of LHD as the averaged beta $<\beta_{dia}>$ (measured with diamagnetic loop) is increased up to 2.6%. The Shafranov shift measured in plasmas with vacuum magnetic axis R_{ax}^{v}=3.75m are larger than those in plasmas with R_{ax}^{v}=3.5m in LHD where the $<\beta_{dia}>$ less than 1.5% as predicted by VMEC calculation based on measured $<\beta_{dia}>$.

LHD is Heliotron type device, which has superconducting coil with poloidal and toroidal period numbers of *l*/*m*=2/10, and the major and minor radii of R/a=3.9m/0.6m [1]. The various heating methods, electron cyclotron heating (ECH), neutral beam injection (NBI), and ion cyclotron resonance heating (ICRH) are available in LHD experiments. Five gyrotrons with the frequency of 82.6GHz (2) and 168GHz (3) are used for plasma production and electron heating, and the main heating devices for LHD plasmas are two NBI injectors with beam energy of 130-150keV.

The x-ray imaging system with soft x-ray back-illumination CCD detector sensitive to the energy range of 1keV to 10keV has been applied to measure magnetic axis in LHD [2]. Although the time resolution determined by mechanical shutter is poor (0.25s), the system has good spatial resolution (1024x512 pixels in image area). By choosing appropriate combinations of size of pinholes and thickness of Be filters, the x-ray image can be measured for the plasmas in the wide range of electron temperature and density. Since the total x-ray emission is considered to be constant on the magnetic-flux surface, the x-ray image represents the magnetic-flux surface. The Shafranov shift of the plasma magnetic axis is derived from x-ray image measured with soft x-ray CCD camera [3].

The inversion of integrated x-ray intensity along the line of sight to the local x-ray emission is not possible, without the equilibrium calculation based on the measured pressure profile, because the inversion needs the shape of magnetic flux surface. The x-ray emission are integrated by using the database of magnetic flux surface which has been calculated for various pressure profiles in LHD, using the three-dimensional free boundary equilibrium code VMEC [4]. The major radius of magnetic axis, R_{ax}, is derived by choosing the magnetic flux surface from databases, which is consistent with the two-dimensional x-ray profile measured [3].

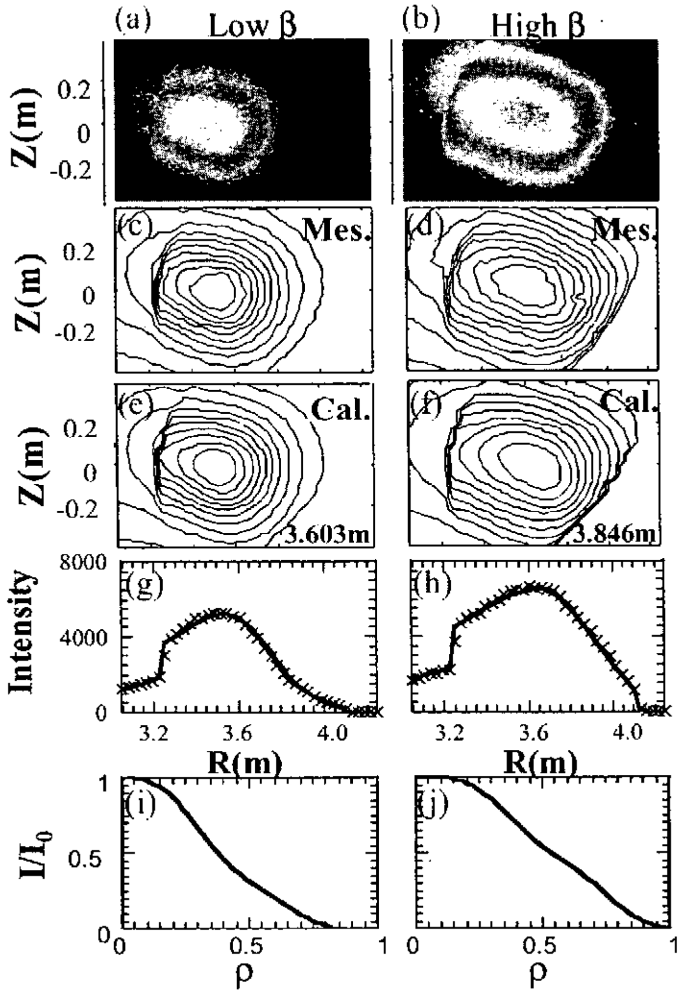

Fig. 1 (a) (b) Images and (c) (d) contour plots of Soft x-ray intensity measured with soft x-ray CCD camera with 190μm and 100μm Be filter, respectively. (e) (f) The best fit contour plots calculated with VMEC code (R_{ax}=3.603 and 3.846m). (g)(h) The horizontal cross-section profiles and (i) (j) normalized x-ray emission profiles.

Figure 1 (a) and (b) show the soft x-ray images measured with soft x-ray CCD camera for a low β plasma (R_{ax}^{v}= 3.6 m; B_t = 2.65 T; $<n_e>$ = $1.4\mathrm{x}10^{19}\,\mathrm{m}^{-3}$) and for a high β plasma (R_{ax}^{v}= 3.6 m; B_t = 0.75 T; $<n_e>$ = $4.9\mathrm{x}10^{19}\,\mathrm{m}^{-3}$), respectively, in LHD. The low β plasma is sustained by ICRH while the high β plasma is heated by NBI. The steep gradients of the x-ray intensity at the left-hand side and lower right-hand side are due to the shadows of inner wall and outer wall, respectively, which give excellent references for the position The clear outward shift of the peak of soft x-ray intensity is observed in the plasma with high β. The Shafranov shift of the plasma magnetic axis is derived by choosing the magnetic flux surface, which gives the best fit to the soft x-ray intensity measured. Fig.1 (c) and (d) show the contour plots of soft x-ray images measured with soft x-ray CCD camera. The magnetic axis of best fit contour plot of soft x-ray image is 3.603m for low beta plasma and 3.846m for high beta plasma. Figure 1 (g) and (h) show a good agreement in the radial profile of x-ray intensity at Z=0 between the best fit of x-ray intensity (solid line) and measured one (cross point). The normalized soft x-ray emission profile for the best fit for low beta plasma is more peaked than that for high beta plasmas.

Figure 2 shows the Shafranov shift measured with soft x-ray CCD camera as a function of averaged-beta $<\beta_{dia}>$ measured with diamagnetic loop. The accuracy determining the major radius of magnetic axis depends on the radial profile of soft x-ray intensity, and is typically few mm and 10mm for the plasma with peaked and flat profile of soft x-ray intensity, respectively. The measured Shafranov shift increases linearly as the averaged beta $<\beta_{dia}>$ is increased up to 2.6%. The Shafranov shift calculated with VMEC code for different plasma pressure profiles of $\alpha 1=2$, 8 and $\alpha 2=2$, 8, where the plasma pressure profile is simplified as $P=P_0(1-\rho^{\alpha 1})(1-\rho^{\alpha 2})$. Here ρ is normalized averaged minor radius. For the high beta discharge with low magnetic field of 0.5T, the Shafranov shift increases up to 28cm (47% of minor radius), and approaching to the calculation with more flat profile as indicated in the magnetic flux surface in Fig. 2.

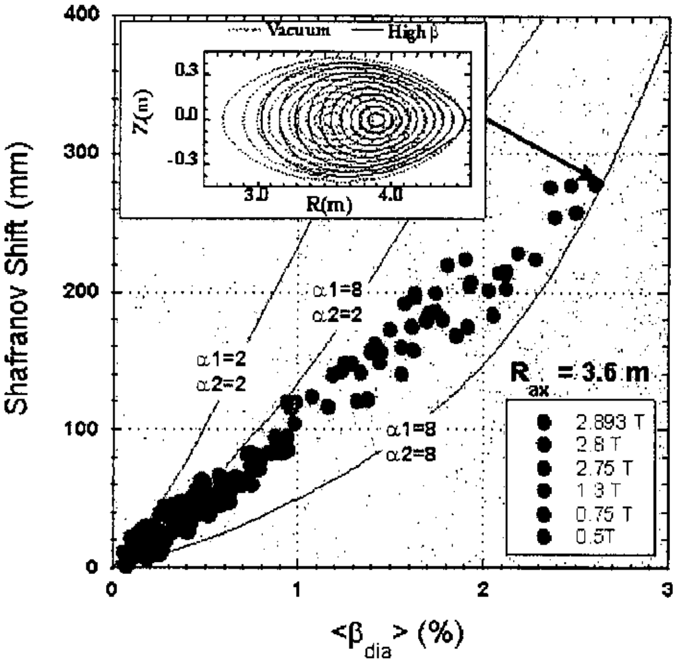

Fig. 2 The Shafranov shift as a function of the averaged-β $<\beta_{dia}>$ for the plasmas with $R_{ax}^{v}=3.6$m. The horizontal elongated magnetic flux surfaces are plotted for high β plasma and vacuum condition, respectively.

The Shafranov shift of magnetic axis due to the Pfirsch-Schlüter current for the low β limit can be expressed as

$$\Delta \cong \frac{aA_p^2\beta_0}{\iota(1)}\int_0^1 \frac{\delta_{1,0}(\rho)}{\iota(\rho)}d\rho,$$

where β_0 is the central β, A_p is the aspect ratio, $\iota(\rho)$ is the rotational transform, and $\delta_{m,n}$ is Fourier component of $1/B^2$ as

$$\frac{1}{B^2}=\frac{1}{\bar{B}^2}\left(1+\sum_{m,n}\delta_{m,n}(\rho)\cos(m\theta-n\zeta)\right)$$

with m (n) and θ (ζ) being the poloidal (toroidal) mode number and angels, respectively [5, 6]. The Pfirsch-Schlüter current is generated by (m,n)=(1,0) component of magnetic filed. Figure 3 shows radial profiles of $\delta_{1,0}/\iota$ for plasmas with a finite $<\beta_{dia}>$ of 0.5% and different vacuum magnetic axes of 3.5 and 3.75m, respectively, in LHD. The value of $\delta_{1,0}$ represent the magnitude of toroidal effect ($\delta_{1,0}$ ~$2\varepsilon_t$ in tokamak plasma). The toroidal effect can be reduced by a large inward shift (ΔR) of magnetic axis from the helical coil center (R_{coil}=3.9m), because the high harmonics of Fourier component of magnetic field, (m, n)=(3, 10), can be large enough to cancel the toroidal effect in some extend.

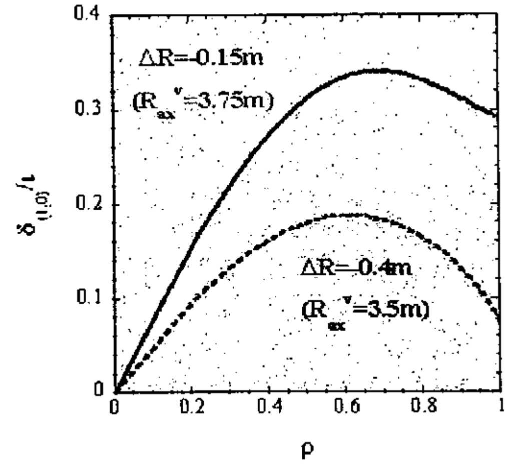

Fig. 3 Radial profiles of $\delta_{(1,0)}/\iota$ for plasmas with different shift ΔR of vacuum magnetic axes of −0.15m (solid) and −0.4m (dashed), where ΔR=(R_{ax}^{V}-R_{coil}) and R_{coil}=3.9m.

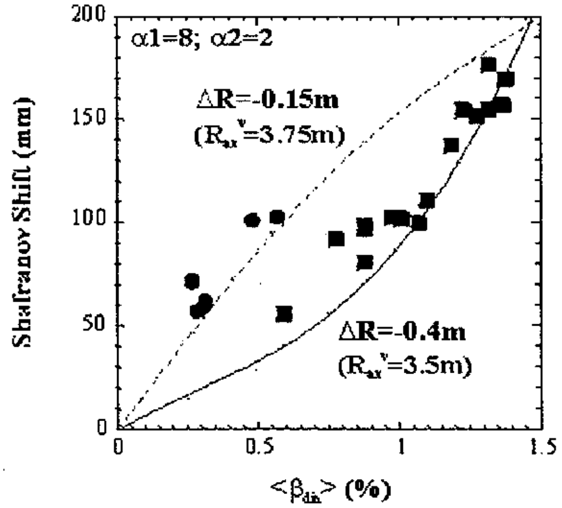

Fig. 4 The Shafranov shift measured with soft x-ray CCD camera as a function of the averaged-β <β_{dia}> for the plasmas with R_{ax}^{v}=3.75m (circle) and R_{ax}^{v}=3.5m (square), respectively. The Shafranov shifts calculated with VMEC code are also plotted for R_{ax}^{v}=3.75m (Solid line) and 3.5m (dashed).

Figure 4 shows the Shafranov shift measured with a soft x-ray CCD camera as a function of averaged beta for R_{ax}^{v}=3.5m and 3.75m in LHD. The electron densities in these discharges are larger than 2x$10^{-19}$$m^{-3}$. The Shafranov shifts measured with soft x-ray CCD camera show that the shift of magnetic axis in the plasma with R_{ax}^{v} =3.75m is larger than those measured in plasmas with R_{ax}^{v}=3.5m in a range of <β_{dia}> <1.5%. The Shafranov shift measured with CCD camera agrees with that calculated using VMEC code with reasonable pressure profile both for the plasmas with R_{ax}^{v}=3.5m and 3.75m.

References

[1] A. Iiyoshi, et al. Fus. Technol., 17, 169 (1990).

[2] Y. Liang, K. Ida, et al., Rev. Sci. Instrum. 71, 3711 (2000).

[3] Y. Liang, K. Ida, S. Kado, et al., Rev. Sci. Instrum. 72, 717 (2001).

[4] S. P. Hirshman and J. C. Whitson, Phys. Fluids, 26, 3553 (1983).

[5]. L. S. Solovev and V. D. Shafranov: Rev. of Plasma Physics Vol. 5 p.1, (1970)

[6] M. Yokoyama, K. Itoh, et al., Nucl. Fusion 40, 1909, (2000).

EFFECTIVE CHARGE DEPENDENCE OF CONFINEMENT IMPROVEMENT FACTOR IN LHD

J. Miyazawa, H. Yamada, S. Morita, K. Tanaka, S. Sakakibara, M. Osakabe, Y. Xu,
B.J. Peterson, S. Murakami, K. Narihara, H. Funaba, M. Goto, O. Kaneko,
K. Kawahata, A. Komori, N. Ohyabu, and LHD experimental Group
National Institute for Fusion Science, Oroshi-cho 322-6, Toki, Gifu 509-5292, Japan

The Large Helical Device (LHD) experiment has demonstrated an energy confinement time exceeding the conventional energy confinement scaling such as the international stellarator scaling 95 (ISS95) with the improvement factor F_{ISS95} of 1.6±0.2 in an average [1], where $F_{\mathrm{ISS95}} = \tau_{\mathrm{E}}^{\mathrm{EXP}} / \tau_{\mathrm{E}}^{\mathrm{ISS95}}$, $\tau_{\mathrm{E}}^{\mathrm{EXP}}$ is the experimental energy confinement time, and $\tau_{\mathrm{E}}^{\mathrm{ISS95}}$ is that expected from the international stellerator scaling 95 (ISS95) as follows [2];

$$\tau_{\mathrm{E}}^{\mathrm{ISS95}} = 0.079 a^{2.21} R^{0.65} P^{-0.59} n_{\mathrm{e}}^{0.51} B^{0.83} \bar{\iota}_{2/3}^{\,0.4}, \tag{1}$$

with energy confinement time, τ_{E}, in s, absorbed heating power, P, in MW, line-averaged electron density, n_{e}, in 10^{19} m^{-3}, volume averaged magnetic field strength, B, in T, and $\bar{\iota}_{2/3}$ is the normalized rotational transform ($\bar{\iota} = \iota/(2\pi) = 1/q$; q is the safety factor) at the two-thirds radius. The scatter of F_{ISS95} suggests a hidden parameter dependence of confinement, although it still has the gyro-Bohm property. Considering simple two-component plasmas that contain electrons and ions of charge Z, the confinement property is a function of the ion gyro radius ρ_{i}, as long as the gyro-Bohm model is applicable to these plasmas. As for three-component plasmas that contain electrons and two kinds of ions, the effective charge, Z_{eff}, and an effective mass, A_{eff}, give the averaged ion gyro radius. At this point, usual scalings do not include Z_{eff} distributing from 1 to 6 in LHD plasmas. In this paper, we compare the experimental results of LHD and the gyro-Bohm model with/without considering Z_{eff} and A_{eff} to show the importance of them in the confinement scaling.

The picture of the gyro-Bohm model gives a thermal diffusivity χ in proportion to $\omega^{*} \rho_{\mathrm{i}}^{2}$ (where ω^{*} is the drift frequency) [3]. Then the energy confinement time predicted by this model $\tau_{\mathrm{E}}^{\mathrm{GB}} \sim a^{2}/\chi$ scales as below;

$$\tau_{\mathrm{E}}^{\mathrm{GB}} = C_0 \, a^{2.4} R^{0.6} B^{0.8} P^{-0.6} n_{\mathrm{e}}^{0.6}. \tag{2}$$

Note that the indices (of a, R, B, P, and n_{e}) in Eq. (2) are almost identical to that of ISS95 scaling in Eq. (1), except for the $\bar{\iota}_{2/3}$ term. An adjustment factor C_0 is determined by the

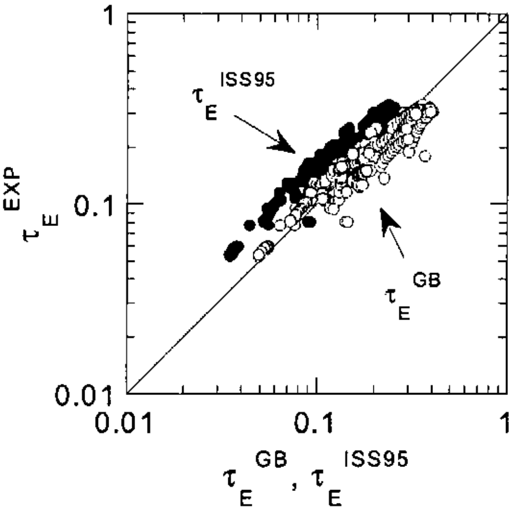

Fig. 1. Comparison of $\tau_{\mathrm{E}}^{\mathrm{GB}}$ and $\tau_{\mathrm{E}}^{\mathrm{EXP}}$ (blue open circles), $\tau_{\mathrm{E}}^{\mathrm{ISS95}}$ and $\tau_{\mathrm{E}}^{\mathrm{EXP}}$ (black closed circles).

experimental data to give the ratio $F_{\mathrm{GB}} = \tau_{\mathrm{E}}^{\mathrm{EXP}}/\tau_{\mathrm{E}}^{\mathrm{GB}} = 1$. Here, $C_0 = 0.105$ and $F_{\mathrm{GB}} = 1.00\pm0.16$ are obtained. Comparison of $\tau_{\mathrm{E}}^{\mathrm{EXP}}$ with $\tau_{\mathrm{E}}^{\mathrm{GB}}$ (or, $\tau_{\mathrm{E}}^{\mathrm{ISS95}}$) is depicted in Fig. 1. The scatter of F_{GB} is almost the same as that of F_{ISS95} (= 1.44±0.21, in this data set). The data set used here consists of 359 data points extracted from 32 shots of hydrogen or helium gas-puff discharges heated by the neutral beam (NB) injection only. The magnetic configuration is fixed to $R_{\mathrm{ax}} = 3.6$ m (R_{ax} is the vacuum magnetic axis), and in consequence, $R \sim 3.69$ m, $a \sim 0.63$ m, and $\iota\!\!\!-_{2/3} \sim 0.64$ are almost unchanged. Each data point is extracted according to some criteria, *i.e.* the ratio of $|\mathrm{d}W_{\mathrm{p}}/\mathrm{d}t|$ to P (= P_{NB}), where W_{p} is the plasma stored energy and P_{NB} is the NB heating power, is lower than 3% and therefore negligible, the changing rate of electron density ($n_{\mathrm{e}}/(\mathrm{d}n_{\mathrm{e}}/\mathrm{d}t)$) is less than 1 s, and $n_{\mathrm{e}} > 1\times10^{19}\,\mathrm{m}^{-3}$. Meanwhile, the gyro-Bohm model in Eq. (2) is incomplete since it does not include the terms of Z_{eff} and A_{eff}. Another energy confinement time $\tau_{\mathrm{E}}^{\mathrm{GBZ}}$ predicted by the gyro-Bohm model consisting of Z_{eff} dependence is given as below;

$$\begin{aligned}\tau_{\mathrm{E}}^{\mathrm{GBZ}} &\propto a^{2.4}R^{0.6}B^{0.8}P^{-0.6}n_{\mathrm{e}}^{0.6}A^{-0.2}(Z^4+3Z^3+3Z^2+Z)^{0.2},\\ &= F_{\mathrm{Z}}\tau_{\mathrm{E}}^{\mathrm{GB}}, \qquad (3)\end{aligned}$$

where $F_{\mathrm{Z}} = C_1A^{-0.2}(Z^4+3Z^3+3Z^2+Z)^{0.2}$ and if Eq. (2) is valid in pure hydrogen plasmas, $C_1 = 8^{-0.2}$. Non-linear term of Z comes from a relation $P\tau_{\mathrm{E}}^{\mathrm{GBZ}} \propto (1 + 1/Z)n_{\mathrm{e}}Ta^2R$ used to obtain Eq. (3). If this model well describes LHD plasmas ($\tau_{\mathrm{E}}^{\mathrm{EXP}} = \tau_{\mathrm{E}}^{\mathrm{GBZ}}$), F_{GB} will be equivalent to F_{Z} and have a strong dependence on Z.

A correlation study of F_{GB} is carried out with various plasma parameters to find out the hidden parameter dependence. The typical ten global parameters are examined, *i.e.* B, P_{NB}, Z_{eff}, n_{e} and its peaking factor $n_{\mathrm{e0}}/n_{\mathrm{e}}$ (n_{e0} is the electron density at the plasma center), the electron temperature T_{e0} (at the plasma center) and $T_{\mathrm{e\_ped}}$ (at the pedestal around $\rho = r/a \sim 0.9$), the peaking factor of the electron temperature $T_{\mathrm{e0}}/T_{\mathrm{e\_ped}}$, the radiation loss P_{rad} and its ratio to the heating power $P_{\mathrm{rad}}/P_{\mathrm{NB}}$. Table 1 is a list of correlation coefficients $\mathrm{R_c}$ obtained in the full data set consisting of 359 data points and the partial data set consisting of 86 data points (see below about the partial data set). The largest $\mathrm{R_c}$ of 0.84 is obtained between Z_{eff} and F_{GB}, as depicted in Fig. 2(a). The second (third) candidate is T_{e0} (n_{e}) that has $\mathrm{R_c}$ of 0.77 (0.56) (see Figs. 2(b) and (c)). Other parameters have low $\mathrm{R_c}$ less than 0.5, and therefore these are less influential. One should be careful to note that T_{e0} might depend on n_{e} when the heating power is fixed, and Z_{eff} is also

Table 1. Correlation coefficients $\mathrm{R_c}$ between ten global plasma parameters and F_{GB} in the full and the partial data sets.

Parameter	$\mathrm{R_c}$ (full)	$\mathrm{R_c}$ (partial)
Z_{eff}	0.84	0.60
T_{e0}	0.77	0.12
n_{e}	0.56	0.22
$T_{\mathrm{e\_ped}}$	0.43	0.22
$T_{\mathrm{e0}}/T_{\mathrm{e\_ped}}$	0.40	0.15
B	0.30	0.31
$P_{\mathrm{NB}}-\mathrm{d}W_{\mathrm{p}}/\mathrm{d}t$	0.14	0.14
$P_{\mathrm{rad}}/(P_{\mathrm{NB}}-\mathrm{d}W_{\mathrm{p}}/\mathrm{d}t)$	0.11	0.04
P_{rad}	0.08	0.04
$n_{\mathrm{e0}}/n_{\mathrm{e}}$	0.01	0.01

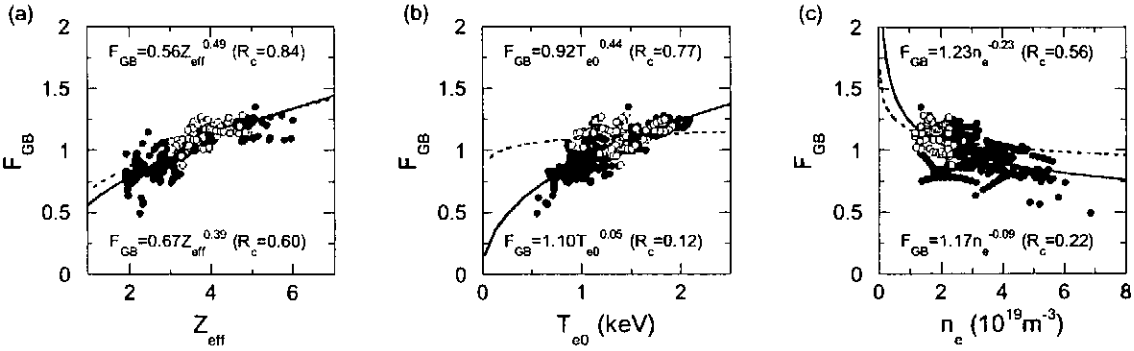

Fig. 2. Linear correlations between (a) Z_{eff} and F_{GB}, (b) T_{e0} and F_{GB}, (c) n_e and F_{GB}. Closed and open circles denote the full data set of 359 points and the partial data set of 86 points, respectively. The correlation coefficient R_c in the full (partial) data set is indicated on the top (bottom) of each figure together with the best-fit curve of solid (broken) line.

dependent on n_e if the impurity influx is constant. In this data set, Z_{eff} weakly correlates with n_e as shown in Fig. 3(a), where Z_{eff} tends to become smaller in the high-density region. This suggests that the influx of impurities is limited and the purity increases in the high-density range where plenty of fuelling gas is puffed. Nevertheless, R_c between n_e and Z_{eff} (or, T_{e0}) is as small as 0.45 (0.31), and therefore negligible. On the other hand, the correlation between Z_{eff} and T_{e0} is not negligible (R_c = 0.72, Fig. 3(c)). It is possible to eliminate this dependence by limiting the boundary of the data set as $1 < n_e$ (10^{19}m^{-3}) < 2.5, $3 < Z_{eff} < 5$, and P_{NB} (MW) < 2. Open circles in Figs. 2 and 3 denote the partial data set obtained after this limitation. Then Z_{eff} and T_{e0} are completely decorrelated (R_c = 0.11). Returning to Fig. 2(b), it can be seen that the correlation between T_{e0} and F_{GB} disappears (R_c = 0.12) in the partial data set, while the strong correlation of R_c = 0.60 still exists between Z_{eff} and F_{GB}. Correlations between F_{GB} and other eight plasma parameters become weaker after the limitation and the correlation coefficients of them are less than 0.31 (see Table 1).

According to these results, Z_{eff} has the largest influence on F_{GB} and therefore the regression analysis considering Z_{eff} together with P, n_e, B will give a strong dependence of the

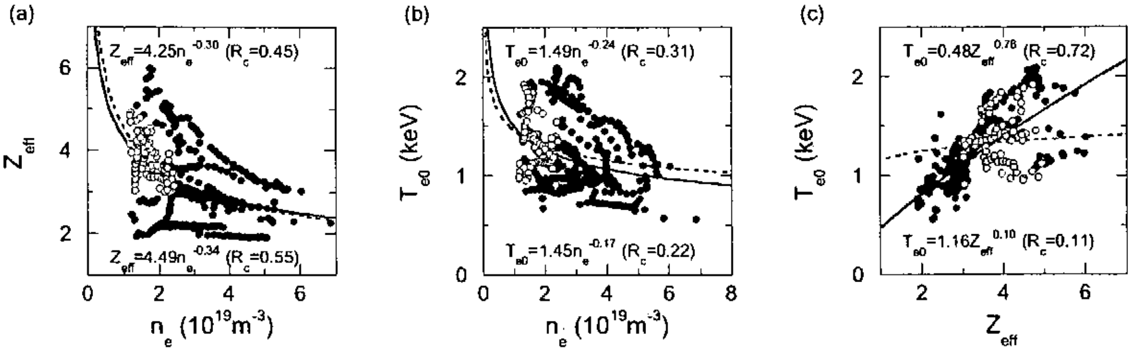

Fig. 3. Linear correlations between (a) n_e and Z_{eff}, (b) n_e and T_{e0}, (c) Z_{eff} and T_{e0}. Closed and open circles denote the full data set of 359 points and the partial data set of 86 points, respectively. The correlation coefficient R_c in the full (partial) data set is indicated on the top (bottom) of each figure.

data set on Z_{eff}. In our data set, all correlations between any two of P, n_e, B and Z_{eff} are less than 0.5 and therefore these parameters are independent. The result of regression analysis is;

$$\tau_E^{\mathrm{FIT}} = 0.041 P^{-0.70\pm0.01} n_e^{0.54\pm0.02} B^{0.91\pm0.02} Z_{\mathrm{eff}}^{0.55\pm0.02}. \tag{4}$$

A strong dependence on Z_{eff} appears as expected and all indices are almost the same as Eq. (3). Therefore, τ_E^{GBZ} can be a nice model to describe τ_E^{EXP}, and F_{GB} will have the same dependence on Z_{eff} and A_{eff} as F_Z. To examine this, A_{eff} is uniquely determined from Z_{eff} assuming three-component plasmas with the majority ions of $A = 2.5$ and $Z = 1.67$ (since the data set consists of hydrogen and helium discharges), and impurity ions of $A = 15$ and $Z = 7$. Exponential fit of F_{GB} with a parameter $(Z_{\mathrm{eff}}^4+3Z_{\mathrm{eff}}^3+3Z_{\mathrm{eff}}^2+Z_{\mathrm{eff}})/A_{\mathrm{eff}}$ then gives

$$F_{\mathrm{GB}} = 0.42((Z_{\mathrm{eff}}^4+3Z_{\mathrm{eff}}^3+3Z_{\mathrm{eff}}^2+Z_{\mathrm{eff}})/A_{\mathrm{eff}})^{0.20\pm0.01}, \tag{5}$$

with a large correlation coefficient of 0.83. The exponent is exactly equal to that of F_Z, assuring the validity of Eq. (3). Therefore, a better prediction of τ_E^{EXP} can be given by $\tau_E^{\mathrm{GBZ}} = F_Z \tau_E^{\mathrm{GB}}$, which consists of the Z_{eff} dependence. Substituting Eq. (5) for F_Z in Eq. (3) ($C_1 = 0.42$), we finally obtain

$$\tau_E^{\mathrm{GBZ}} = 0.044 a^{2.4} R^{0.6} B^{0.8} P^{-0.6} n_e^{0.6} A^{-0.2} (Z_{\mathrm{eff}}^4+3Z_{\mathrm{eff}}^3+3Z_{\mathrm{eff}}^2+Z_{\mathrm{eff}})^{0.2}. \tag{6}$$

In Fig. 5, compared are the distributions of $\tau_E^{\mathrm{EXP}}/\tau_E^{\mathrm{GBZ}}$ (= 1.03±0.09), $\tau_E^{\mathrm{EXP}}/\tau_E^{\mathrm{GB}}$ (= F_{GB} = 1.00±0.16) and $\tau_E^{\mathrm{EXP}}/\tau_E^{\mathrm{ISS95}}$ (= F_{ISS95} = 1.44±0.21). The scatter of the prediction has been almost halved by this revision. The standard deviation of $\tau_E^{\mathrm{EXP}}/\tau_E^{\mathrm{GBZ}}$ is 8.8% and much smaller than that of F_{GB} (15.9%) or F_{ISS95} (14.4%). These results indicate the importance of Z_{eff} on the confinement scaling.

In conclusion, it is possible to increase the accuracy of an energy confinement scaling of high-temperature plasmas, which can be well described by the gyro-Bohm model, after introducing the Z_{eff} terms. This comes from a simple assumption that the energy confinement is a function of the averaged ion gyro radius determined by Z_{eff}.

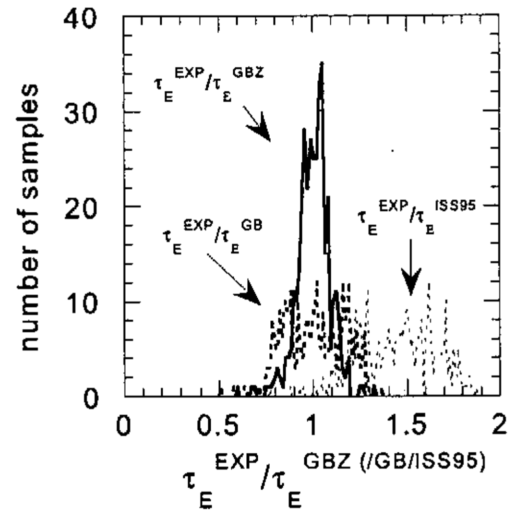

Fig. 4. Distributions of $\tau_E^{\mathrm{EXP}}/\tau_E^{\mathrm{GBZ}}$ (red solid line), $\tau_E^{\mathrm{EXP}}/\tau_E^{\mathrm{GB}}$ (blue broken line), and $\tau_E^{\mathrm{EXP}}/\tau_E^{\mathrm{ISS95}}$ (black broken line).

References

[1] H. Yamada, *et al.*, Nucl. Fusion (in press).

[2] U. Stroth *et al.*, Nucl. Fusion **36**, 1063 (1996).

[3] J.G. Cordey, *et al.*, Nucl. Fusion **39** (1999) 301-308.

Role of Changing Transport in 'Breathing' Oscillations in LHD

B.J. Peterson, H. Funaba, K. Itoh, J. E. Rice[1], K. Yamazaki, Y. Nakamura, N. Noda,
Y. Takeiri, Yuhong Xu, N. Ashikawa[2], K. Narihara, K. Tanaka, S. Masuzaki,
T. Tokuzawa, K. Sato, M. Goto, K. Ida, S. Sakakibara, J. Miyazawa, M. Osakabe,
A. Kostrioukov, K. Tsumori, K. Ikeda, S. Kubo, H. Idei, K. Kawahata, H. Yamada, O.
Kaneko, N. Ohyabu, K. Komori, S. Sudo, O. Motojima and the LHD Experimental Group

National Institute for Fusion Science, Toki-shi, Gifu-ken 509-5292, Japan
[1]Plasma Science and Fusion Center, Mass. Inst. of Tech., Cambridge, MA 02139 USA
[2]Graduate University for Advanced Studies, Toki-shi, Gifu-ken 509-5292, Japan

1. Introduction

In the Large Helical Device a slow oscillation of plasma parameters known as 'breathing' plasma has been observed [1] which limited the density [2] and has been linked to the transport in and out of the plasma of iron impurities [3]. Modelling of the sputtering of the stainless steel from the divertor plates during this oscillation using the electron temperature at the divertor shows the core iron density starts to increase 20 – 60 ms after the initiation of sputtering. This indicates that the stainless steel from the divertor may be a periodic source of the iron impurity [3]. Several theoretical models have been suggested to explain this phenomenon [4-6], however none of them fully address the changes in transport observed during this oscillation. In this paper the evidence for the changes in transport is described and the source of this change in transport and the role that this might be playing in the oscillation are discussed.

2. Observations of changing transport

Changes in transport manifest themselves in two different ways during the 'breathing' oscillation. The first of these is a variation of its frequency during the oscillation. The second is a modification of the electron and iron density profiles during the oscillation. The variation of the frequency can be seen most clearly in Fig. 1(a) in the comparison of the iron density calculated in Ref. [3] with local measurements of electron density, temperature, and radiation emissivity using an average-ion, corona-equilibrium model (ADPAK) for the iron cooling rate and that modeled using the MIST impurity transport code [7]. In this modeling the

MIST code is operated in time dependent mode and the sputtered iron is treated as a series of iron impurity injections with the amount of injected material being modulated by the calculated sputtering yield shown in Fig. 1(c). The MIST model uses a flat diffusion coefficient profile with a value of D = 0.15 m^2/s going to zero at the edge and a flat convection velocity profile v = 0 m/s. The comparison is qualitative in that the amplitude and offset are arbitrarily adjusted to match the ADPAK result to take into account the residual iron content and the effective area of the sputtered divertor plate, both of which are not know. Comparing the shapes of these curves one notes that the rise and decay of the ADPAK iron density is much faster than that from the MIST model while the period where the iron density peaks is rather well matched. This indicates that the diffusion coefficient is approximately correct, but that it varies during the oscillation being much higher in the beginning and end of the cycle. Closer examination reveals that the results of the ADPAK modeling diverge quickly from the MIST model at t = 5.5 and 6.5 sec indicating a sharp transitions in the impurity diffusion. This is also clearly seen in Fig. 1(b) in the fast transition from the rising phase to the falling phase and the difference in the rising and falling times in the radiation emissivity at r/a=0.4. This indicates that the change in source resulting from the on/off behavior of the sputtering cannot alone account for the changes in the core iron density, but that a change in transport is also playing a role in this oscillation.

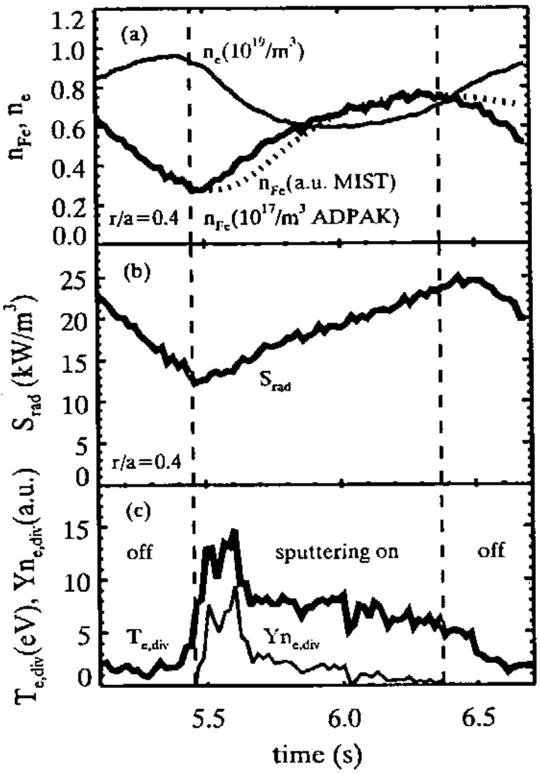

Figure 1 (a) measured electron density(blue), iron density calculated using the ADPAK model(black) and using MIST modeling (red, broken) at r/a = 0.4. (b) Measured radiation emissivity at r/a = 0.4. (c) Electron temperature at the divertor(black) and resulting model of sputtering yield (red).

Other evidence of this change in the frequency is the dependence of the oscillation frequency on density, which is shown in Fig. 2. This data is taken from the original 'breathing' discharges observed in the divertor configuration during LHD's 2nd campaign (1998) as well as from discharges in the wall limiter configuration from the 3rd (1999-2000) and 4th (2000-2001) campaigns and discharges in the divertor configuration from the 4th campaign. These wall limiter discharges were formed by adjusting the helical coil current distribution to fatten the plasma cross-section in plane of the helical coil to scrape off the plasma on the inboard stainless steel wall. These wall limiter discharges show properties similar to the original 'breathing' oscillations with the exception of a lack of electron density oscillation in some cases. Therefore it is thought that this is the same phenomenon, with the source of iron being the stainless steel wall limiter instead of the divertor. The frequency dependence on density seen in Fig. 2 is consistent with the change in frequency of the iron density relative to the electron density level observed in Fig. 1 (a). However it does not explain the rapid changes observed.

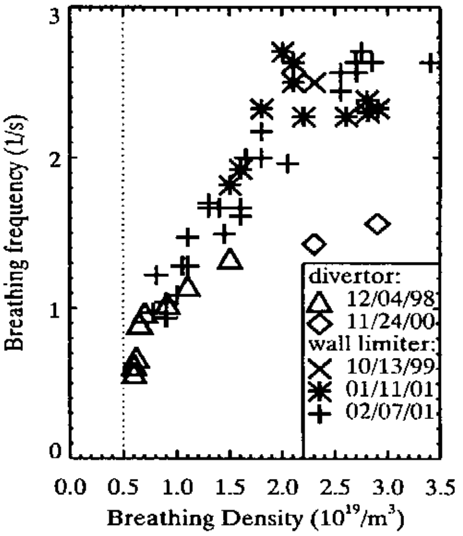

Figure 2 Frequency dependence of 'breathing' oscillation on line averaged density.

The second way in which a variation in transport is observed during the oscillation is in the change of the electron and iron density radial profiles during the oscillation as was pointed out in Figs. 2 (c) and (g) of Ref. [3]. This can be seen clearly in the plot of the positive density gradients shown in Fig. 3. It is interesting to note the temporal and spatial coincidence in the peaks of the gradients with that of the iron impurities slightly preceding that of the electrons. The dramatic changes in these profiles also indicate that transport is changing during this oscillation.

3. Discussion

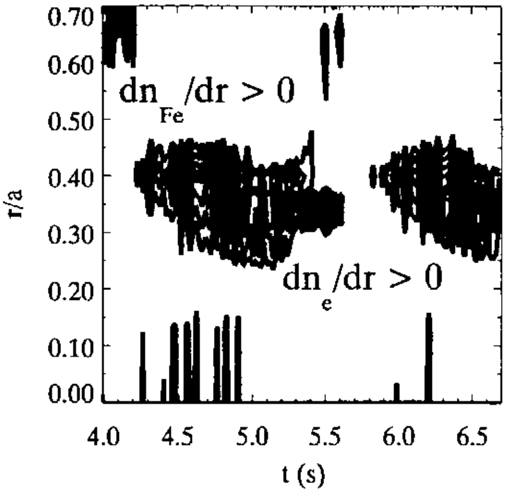

Figure 3 Evolution of positive iron (red) and electron (blue) density gradients during the 'breathing' oscillation.

In seeking a recipe for the 'breathing' oscillation, analysis has made clear that the transport in and out of the core plasma of iron impurities from plasma facing components is the key ingredient. What is not yet clear is the relative importance of the competing ideas of changing source and changing transport. Modeling and experimental observation indicate the source of iron is most likely the plasma facing components (divertor tiles in the divertor case, wall plates in the wall limiter case), and that this source is changing during the oscillation. However, further modeling has shown that a change in transport is necessary to explain the time evolution of the core iron density. In addition changes in the iron and electron density profiles indicate a change in bulk particle and impurity transport during this oscillation.

The results shown raise several interesting questions. First of all, why is the oscillation frequency a function of the electron density? One simple explanation is that at higher density the impurities radiate proportionately higher and the cooling necessary to detach from the divertor/wall occurs more quickly. Also there seems to be a density threshold below which the oscillation does not occur. In this case perhaps the radiated power loss relative to the power absorbed from the beam is not adequate to cool the plasma to the point of thermal collapse. This is related to the radiative density limit in LHD which is currently being studied. Probably the most important question to be answered is what is the root cause of the changing transport that is observed in the time evolution of the core iron density and the iron and electron density profiles in general. A related question is why the iron impurities and electrons are accumulating at r/a = 0.4. A possible answer to these two questions lies in the radial electric field profile. Preliminary measurements of the radial electric field show it changing sign at r/a = 0.4 from positive to negative with increasing minor radius. This is coincident with the accumulation of iron impurity ions at r/a = 0.4. Also, at the edge of the plasma, the density regime at which the oscillation takes place is characterized by multiple roots (positive and negative) of the neoclassical E_r [8]. Therefore we propose to investigate in the future the possibilities that a fast sign transition of the radial electric field may be responsible for the observed change in transport and the periodic accumulation of iron impurities at r/a = 0.4.

References

[1] Y. Takeiri et al., Plasma Phys. and Control. Fusion **42** (2000) 147.

[2] Y. Nakamura et al., J. Nucl. Mater. **290-293** (2001) 1040.

[3] B.J. Peterson et al., Nuclear Fusion **41** (2001) 519.

[4] K. Itoh, S.-I. Itoh, and L. Giannone, Research Report NIFS-627.

[5] H. Wobig, Plasma Phys. Control. Fusion **42** (2000) 931.

[6] M. Tokar, et al., Phys. of Plasmas **7** (2000) 4357.

[7] R. A. Hulse, Nucl. Tech./Fus. **3** (1983) 259.

[8] K. Ida et al., Phys. Rev. Letters **86** (2001) 5297.

5-D Simulation Study of Energetic Tail Ion Transport during ICRF Heating in LHD

S. Murakami, H. Yamada, M. Isobe, M. Sasao, K.Y. Watanabe, K. Ida, R. Kumazawa,
S. Morita, T. Mutoh, K. Narihara, T. Ozaki, T. Seki, K. Tanaka, T. Watari, K. Itoh, A. Komori,
O. Motojima, and LHD Experimental Group
National Institute for Fusion Science,
Toki 509-5292, Japan

1. Introduction

The behaviors of trapped particles are complicated and have relatively large orbit size in the radial direction in heliotrons. These radial motions of trapped particle would enhance the radial transport of energetic ions. Also, because of fast drift motion of energetic ions, the direct convective transport by grad-B drift of ripple trapped particle would be important in the energetic ions confinement in addition to the diffusive (neoclassical) transport, which plays dominant role in the thermal plasma. Thus, the ripple induced transport of energetic ions is an important issue for the energetic ion confinement.

ICRF heating experiments[1-3] have been successfully done and have shown significant performance of this heating method in LHD. Up to 400keV of energetic tail ions have been observed by fast neutral analysis. However, the measured information is obtained as an integrated value along a line of sight and we need the theoretical model for the energetic tail ion distribution to discuss the role of ripple induced transport.

In this paper we study the transport of energetic tail ions during ICRF heating in LHD using a global transport simulation code in 5-D phase space (GNET)[4,5]. We make clear the characteristics of minority ion distribution in the phase space and show the role of ripple-induced transport in the energetic tail ion confinement in LHD.

2. Simulation Model

Many efforts have been made to analyze the energetic particle distribution and the transport during ICRF heating, analytically and numerically (Fokker-Planck model and etc.), but most of the analyses using local approximation. A simple Orbit following Monte Carlo simulation has been used to take into account the non-local effect due to finite orbit size of energetic ions. However, the energetic particle distribution changes in time and we can not obtain a correct steady state by this type of Monte Carlo simulation. To obtain a steady state we should consider the balanced state between particle source and sink correctly in a global simulation.

We solve the drift kinetic equation of minority ion during ICRF heating in 5D phase-space

$$\frac{\partial f}{\partial t}+(\mathbf{v}_{//}+\mathbf{v}_D)\cdot\nabla f+\mathbf{a}\cdot\nabla_v f=C(f)+Q_{ICRF}(f)+S_{particle}+L_{particle}$$

where $C(f)$ and Q_{ICRF} are the linear Clulomb Collision operator and the ICRF heating term by the wave-particle interaction. $S_{particle}$ is the particle source term by ionization of neutral particle [Fig. 1; $n_0=1\times10^{19}m^{-3}$ (dashed line) and $2\times10^{19}m^{-3}$ (solid line)] and the radial profile of the source is evaluated using AURORA code. $L_{particle}$ is the particle sink (loss) term consists of two parts; one is the loss by the charge exchange loss assuming the same neutral particle profile as the source term calculation and the other is the loss by the orbit loss escaping outside of outermost flux surface. In GNET code the minority ion distribution f is evaluated through a convolution of $S_{particle}$ with a characteristic time dependent Green function evaluated using test particle Monte Carlo method.

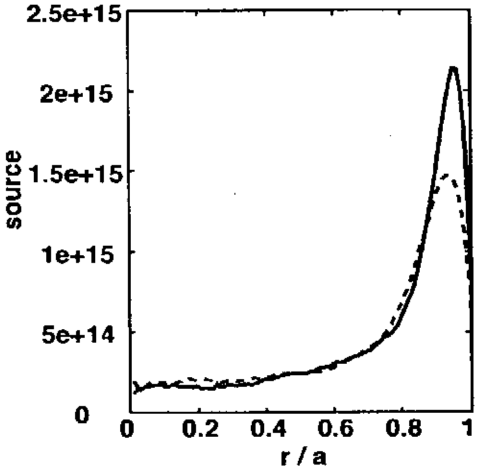

Fig.1 : Source profile of minority ions

3. Simulation Results

We, here, consider two LHD configurations with different values of the magnetic axis shift in the major radius direction; one is the "standard" configuration (R_{ax} = 3.75m) satisfying the requirements for highly balanced plasma performance (i.e. a high plasma beta, relatively good particle confinement, and creating a divertor configuration) and the other is the "inward shifted" configuration (R_{ax} = 3.6m) where the confinement of ripple trapped particle is improved drastically and the good confinement of energetic ions would be expected.

Figure 2 shows the steady state distribution of the minority ions during ICRF heating obtained by GNET code for the two configurations of LHD (R_{ax}= 3.6m and 3.75m). We plot the flux surface averaged tail ion distribution in the three dimensional space (r/a, $v_{//}$, v_{perp}), where a/r, $v_{//}$ and v_{perp} are the normalized averaged minor radius, the parallel and perpendicular velocities normalized by the thermal velocity at the plasma center, respectively. We assume the same heating and plasma parameters as the experimental ones, where the RF heating power of about 2.5MW, the magnetic field strength at R=3.6m is

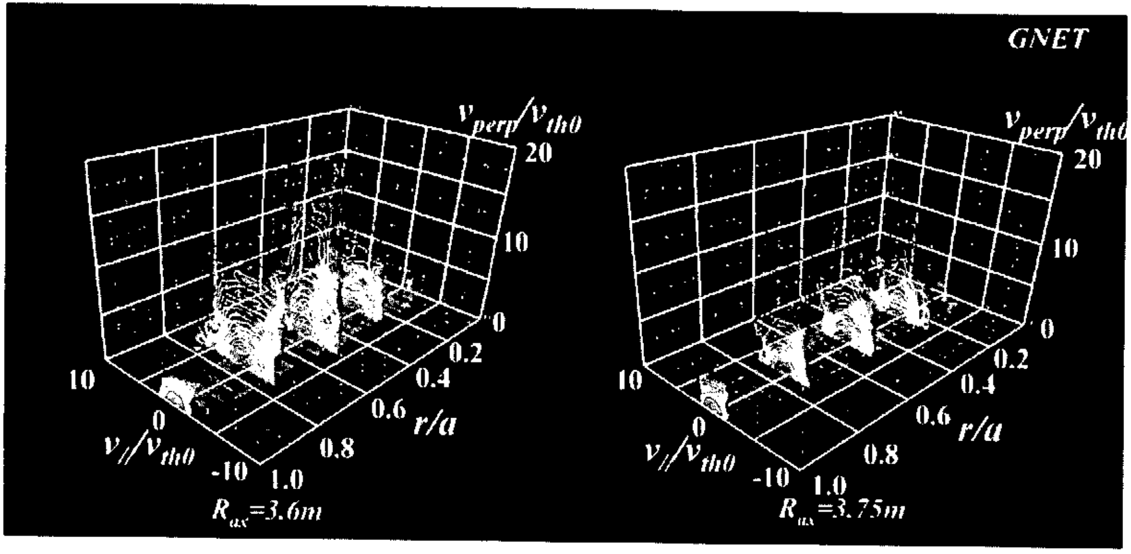

Fig. 2: Energetic tail ion distribution in the (r/a, $v_{//}$, v_{perp}) coordinates in the LHD plasma for two different configurations; R_{ax}= 3.6m (left) and R_{ax}= 3.75m (right).

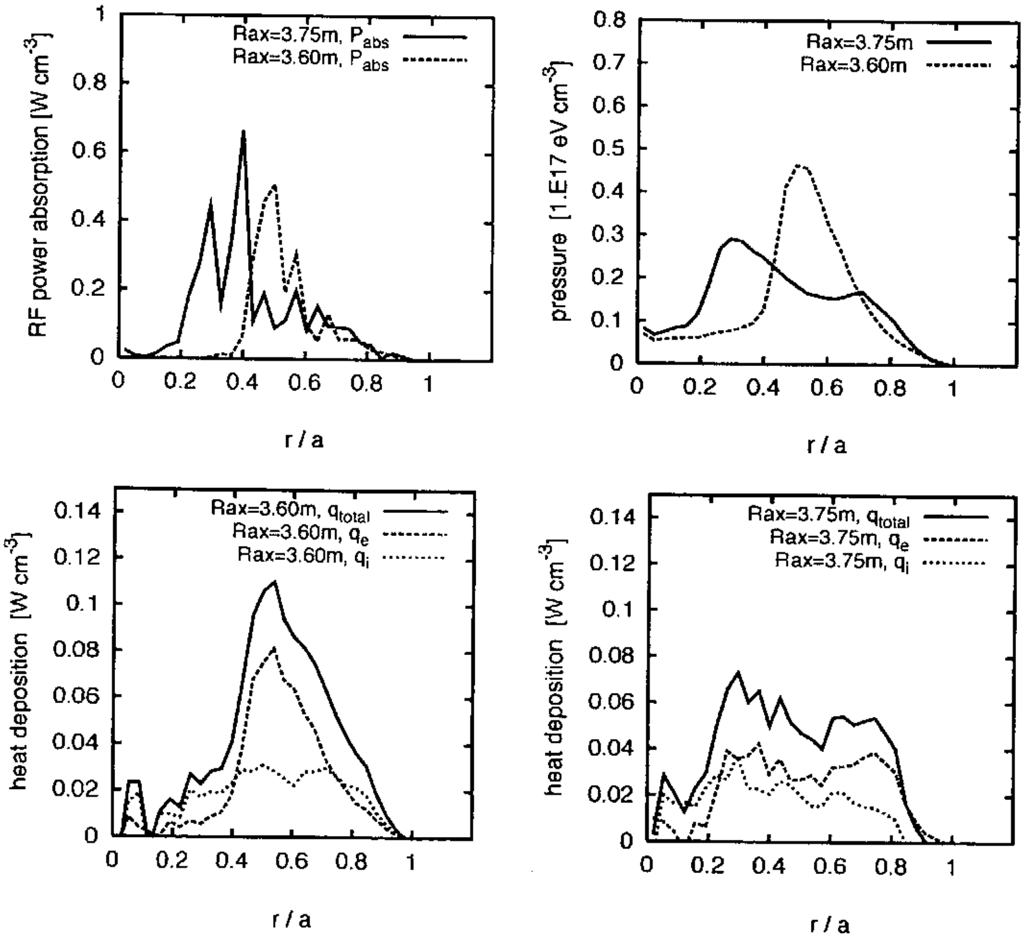

Fig. 3: Radial profiles of RF power absorption (left top), energetic ion pressure (right top), heat deposition (left bottom; R_{ax}= 3.6m and right bottom of R_{ax}= 3.75m).

2.75T and the resonance region only exists $r/a>0.5$ in the R_{ax} = 3.6m configuration. The density, n, and temperature, T, are assumed to be $n=n_0(1-(r/a)^8)$ and $T=T_0(1-(r/a)^2)$ where $n_0=1\times10^{19}\mathrm{m}^{-3}$ and T_0=1.6keV.

The RF wave accelerates minority ions perpendicularly in the velocity space and we can see perpendicularly elongated minority ion distributions in both cases. Also we find a peaked energetic tail ion distribution near r/a~0.5 in the R_{ax} = 3.6m case, while a broader distribution of energetic tail ions can be seen in the R_{ax} = 3.75m case. This is due to the larger trapped particle orbit size. The energetic particle would be localized more in the R_{ax} = 3.6m case.

Figure 3 (left top and right top) shows the radial profiles of RF power absorbed by minority ions and pressure profile of minority ions. The peak of RF power absorption appears at r/a ~0.5 in the R_{ax} = 3.6m case and is at r/a ~0.4 in the R_{ax} = 3.75m case. Then, we can see the peak of pressure profile also at r/a ~0.5 in the R_{ax} = 3.6m case. On the other hand we can see a broader pressure profile in the R_{ax} = 3.75m case. This shows that the larger ripple induced transport occurs in the R_{ax} = 3.75m case. The heat deposition profile (Fig.3: bottom) also shows the broader profile in the R_{ax} = 3.75m case than that in the R_{ax} = 3.6m case and the obtained heating efficiency is 40% higher in the R_{ax} = 3.6m case.

4. Conclusions

We have developed a 5D (3D+2D) phase space simulation code, GNET, for studying the global collisional transport in non-axisymmetric configurations. The GNET code has been applied to the analysis of energetic tail ion transport during ICRF heating in the LHD plasma. A steady state distribution of energetic tail ion has been obtained and the characteristics of distribution in the phase space are clarified. The configuration dependency on the distribution have been shown and higher heating efficiency have been obtained in the R_{ax}=3.6m.

References

1. T. Mutoh, et al., Plasma Phys. Control. Fusion **42** (2000) 265.
2. T. Watari, et al., Nuclear Fusion **41** (2001) 325.
3. R. Kumazawa, et al., Phys. Plasmas **8** (2001) 2139.
4. S. Murakami, et al., Nuclear Fusion **40** (2000) 693.
5. S. Murakami, et al, "Neoclassical Transport of Energetic Beam Ions in the Large Helical Device" in 6th IAEA-TCM on "Energetic Particle in Magnetic Confinement Systems" 1999, JAERI, Naka, JAERI-Conf 2000-004 (2000) 97-100.

Investigation of Symmetric Thermal Decay and Asymmetric Radiative Collapse of NBI Heated Plasma on LHD

Yuhong Xu, B. J. Peterson, S. Sudo, T. Tokuzawa, K. Narihara, M.Osakabe, M.Goto,
S. Sakakibara, K. Tanaka, K. Kawahata, K. Tsumori, K. Ikeda, S. Kubo, H. Idei,
J. Miyazawa, K. Y. Watanabe, K. Nishimura, A. Kostrioukov, H. Yamada,
O. Kaneko, N. Ohyabu, K. Komori and the LHD Experimental Group
National Institute for Fusion Science, Toki-shi, Gifu-ken 509-5292, Japan

1. Introduction

In both tokamak and helical plasmas the maximum achievable density is limited[1,2]. Increasing the density induces an increase in impurity radiation and thus a radiative collapse via a thermal instability[3]. In tokamaks, both the poloidally symmetric radiation belt and the asymmetric MARFE(multifaceted asymmetric radiation from the edge) have been observed[1,4]. In helical devices, the issues regarding the density limit and radiative collapse have also been studied intensively [2,5-7]. On LHD, a MARFE-like radiation profile has been observed[7]. In this paper, the basic features, including the radiation structures, in the decay and collapse discharges on LHD are compared. The time evolutions of the radiation profile in the collapse discharges are investigated.

2. Experimental setup and diagnostics

The Large Helical Device(LHD) is a large superconducting heliotron system with a set of *l*/*m*=2/10 helical coils. The experiments subjected to this work were conducted under conditions of R/a=3.6~3.75m/0.6m, B_t=1.5~2.75T, n_e=0.6~7.0×$10^{19}$$m^{-3}$ and $T_e(T_i)$ = 0.5~2 keV. The total plasma radiation profile is measured by a multi-channel bolometer array viewing the vertically elongated cross-section of the plasma[7].

3. Basic features of the decay and collapse of NBI heated plasmas on LHD

In LHD, the NBI heated discharges are terminated in two ways: (a) thermal decay(TD) after the termination of NBI; (b)radiative collapse(RC) during the NBI. The typical discharge waveforms of the TD and RC shots are displayed in Fig. 1. The figure shows that the plasma is initially produced by ECH and then expanded with increasing stored energy W_p due to NBI heating. For the TD plasma, the line-averaged electron density $\overline{n}_e$ reaches its maximum shortly after the termination of the gas puffing, and the OV/CIII emission and P_{rad} are roughly proportional to $\overline{n}_e$ up to 0.88s. Then, with further decrease in temperature, a sharp increase is shown in OV/CIII radiation. But their amount is small, having little contribution to P_{rad}. In the RC shot, the strong gas puffing results in a continuous increasing of $\bar{n}_e$ and thus increases in OV/CIII emission and P_{rad}. After 0.86s, the highly increased $\bar{n}_e$ induces a dramatic nonlinear increase of P_{rad} with $\bar{n}_e$, implying the occurrence of a thermal instability(TI). In Fig.1, we can also see that the P_{rad} in the TD plasma is smaller than P_{dep} (deposited NBI power) during the NBI phase, while for the RC plasma, P_{rad} is increased rapidly after the TI onset and exceeds P_{dep} soon, leading to a collapse of the discharge. The above results reveal a crucial role of the density level in dominating the decay and collapse of the discharge. On LHD, another clear difference between the TD and RC plasmas lies in their total radiation structures. Fig. 2 displays the contour plots of the time evolution of the chord-integrated radiation brightness for the TD and RC shots shown in Fig. 1. In Fig. 2(a), the TD plasma shows a symmetric radiation profile on the inboard-outboard side throughout the discharge, while in Fig. 2(b) the RC plasma shows a symmetric radiation profile at the first stage and then an asymmetric profile with high radiation located on the inner side of the torus before the end of the discharge. As seen in the expanded time trace,

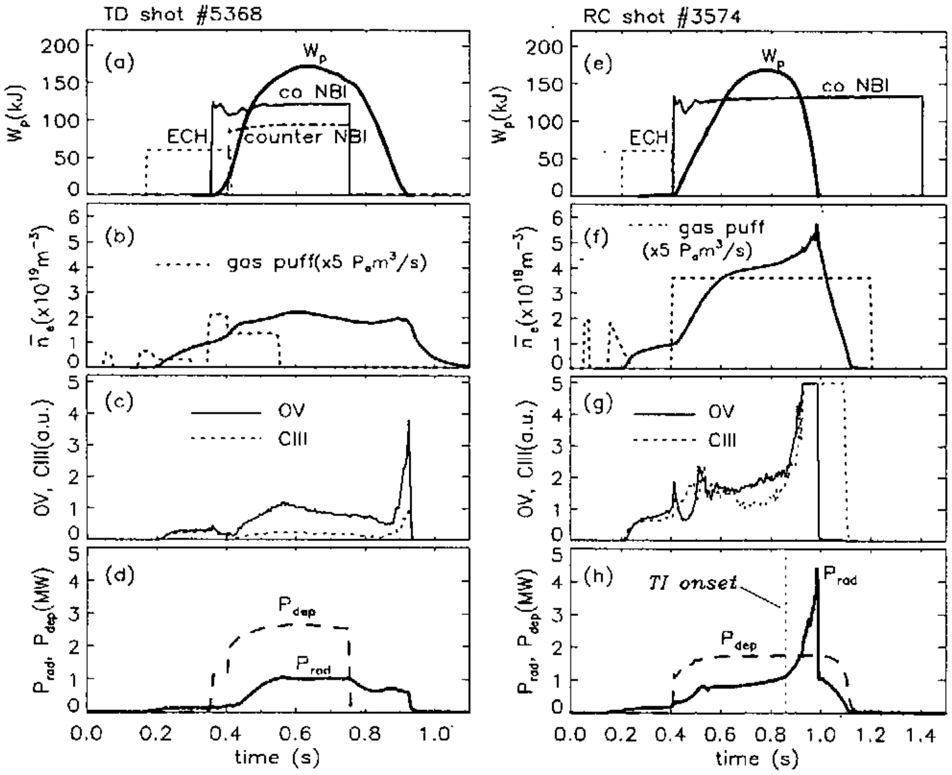

Fig. 1. Typical discharge waveforms of a thermal decay(TD) (left column) and a radiative collapse(RC) (right column) discharge. (a) and (e) Total plasma stored energy, ECH and NBI timing, (b) and (f) line-averaged density and gas puff, (c) and (g) emission intensity of OV and CIII and (d) and (h)total radiated power and deposited NBI power. The dashed line in (h) indicates a TI onset.

instability(TI).

the asymmetric radiation(AR) occurs at about 0.935s, roughly 80ms later than the TI onset, as shown by the dashed line in Fig. 1(h).

4. Characterization of the poloidally asymmetric radiation in RC discharges

As seen in Fig. 2(b), the basic property of the AR on LHD resembles that of MARFE observed in tokamaks, which also radiates stronger on the inner side. But unlike MARFE, the AR on LHD is transient and only appears before the end of the RC discharge. A similar time evolution in the density profile has been observed[7]. Here we focus on the comparisons of the time evolutions of the radiation profile with those of the temperature and temperature profile. shown in Fig. 3 is another RC shot summary. In Fig. 3(a), the sudden nonlinear increase of P_{rad} with $\bar{n}_e$ at 1.64s indicates a TI onset. Fig. 3(b) displays that the initial drop of central temperature T_{e0} occurs at ~1.3s, considerably earlier than the TI onset time. In Figs. 3(c) and (d), an expanded time trace of T_{e0} is shown together with the radiation brightness contour plot, where the AR is observed beginning at 1.75s. Thus, the collapse of T_{e0} can be divided into three phases: phase I before TI onset, phase II between TI and AR and phase III after AR formation. In Fig. 4, the electron temperature T_e profiles

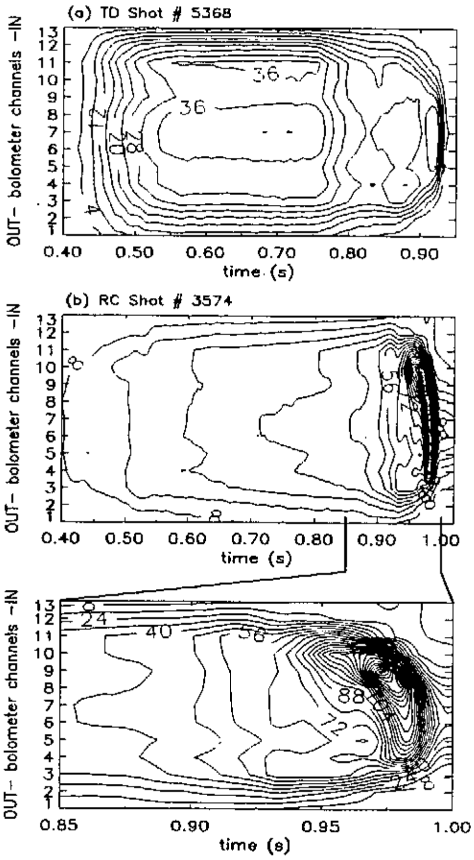

Fig. 2 Contour plots of the time evolution of the chord-integrated radiation brightness for the TD and RC shots shown in Fig. 1

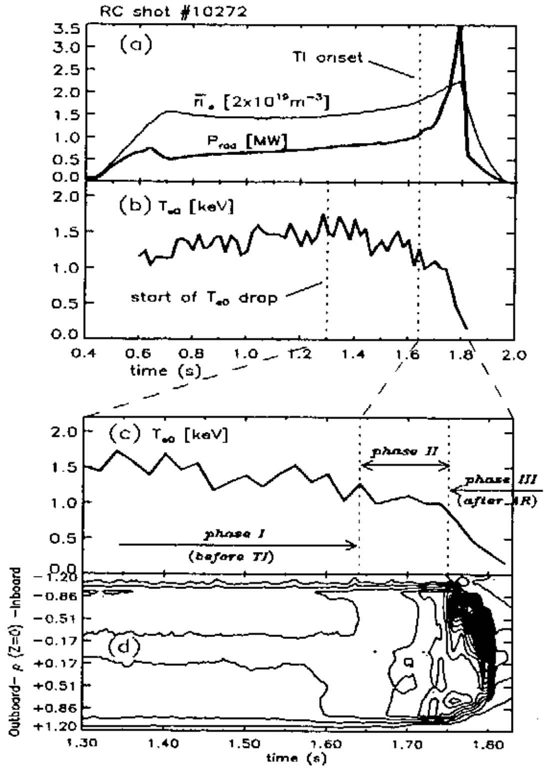

Fig. 3. Time traces of (a) line-averaged density $\bar{n}_e$ and total radiated power P_{rad} and (b)central electron temperature T_{e0} during a RC shot. Shown in (c) is the expanded time trace of T_{e0} and (d) the contour plot of the chord-integrated radiation brightness.

measured at four times(t1 ,t2, t3, t4) across the above three phases are plotted in terms of the normalized radius ρ. From this figure, we can see that in phase I (t1-t2) the overall T_e profile is reduced to a low level. From the beginning of phase II (t2-t3), a clear shrinking of the plasma radius can be observed, indicating that a substantial contraction of the plasma is initiated after the trigger of TI. But unlike that in tokamaks, this shrinkage of plasma does not result in any sudden dramatic termination of the discharge. In phase III (t3-t4), with the plasma column further contracting, the differences between the inboard and outboard T_e profiles at the edge zone are rather clear. On the outer periphery (below dashed line, $T_e \leq 50$eV), the T_e on the inner side is lower than outside, consistent with the asymmetric radiation profile, i. e., low temperature, high radiation on the inner side and high temperature, low radiation on the outer side. The results indicate a good coincidence of the development of the radiation profile with the temperature and density profiles.

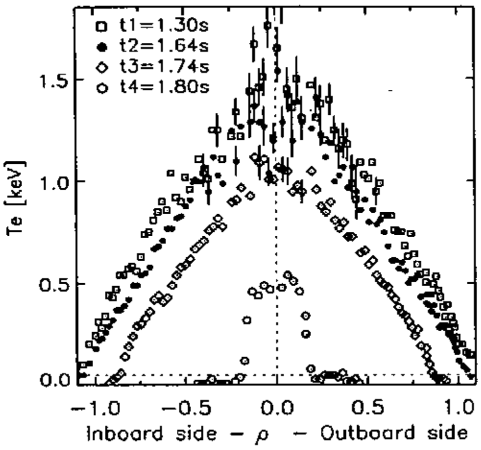

Fig. 4. Electron temperature T_e profiles measured at four times across the three temperature collapse phases I, II and III, as shown in Fig.3

5. Summary

In this paper, the TD(thermal decay) and RC(radiative collapse) discharges on LHD have been reported. Comparisons between them indicate that the density limit processes play a crucial role in dominating the decay and collapse of the discharge. The different features in their radiation profiles are also shown. In the RC discharges, the total radiation profile develops in several phases, consistent with the time evolutions of temperature and density profiles. A shrinkage of the plasma column is observed just after the onset of TI.

References:

[1] Rapp, J., et al., Nucl. Fusion **39** (1999) 765.

[2] Sudo, S., et al., Nucl. Fusion **30** (1990) 11.

[3] Ohyabu, N., Nucl. Fusion **9** (1979) 1491; Stacey, W. M., Phys. Plasmas **4** (1997) 1069.

[4] Lipschultz, B., J. Nucl. Mater. **145-147** (1987) 15.

[5] Giannone, L., et al., Plasma Phys. Control. Fusion **42** (2000) 603.

[6] Itoh, K., Itoh, S.-I., Giannone, L., Research Report NIFS-627(2000).

[7] Peterson, B.J., et al., submitted to Phys. Plasmas.

Effect of Magnetic Islands on LHD Plasma Performance

A. Komori, R. Sakamoto, T. Morisaki, J. Miyazawa, K. Narihara, B. J. Peterson, S. Masuzaki,
S. Sakakibara, H. Suzuki, M. Shoji, S. Inagaki, H. Yamada, N. Ohyabu, H. Idei, K. Ikeda,
S. Kubo, S. Morita, S. Murakami, T. Mutoh, Y. Narushima, S. Ohdachi, T. Seki,
K. Tanaka, K. Tsumori, K. Y. Watanabe, O. Kaneko, K. Kawahata, O. Motojima
and the LHD Experimental Group

National Institute for Fusion Science, Toki 509-5292, Japan

1. Introduction

Plasmas heated by neutral beam injection (NBI) have indicated the favorable density dependence of energy confinement in the Large Helical Device (LHD) [1]. The energy confinement time τ_E is scaled by $\tau_E \propto P_{abs}^{-0.60}\, \bar{n}_e^{0.47}\, B_t^{0.75}$ in the configuration with a magnetic axis position R_{ax} of 3.6m [2]. Here P_{abs}, $\bar{n}_e$ and B_t are absorbed heating power, line-averaged density, and magnetic field, respectively. Therefore, an increase in $\bar{n}_e$ is a key issue in maximizing stored energy W_p., and pellet injection has a great impact on expanding the operational regime toward a high-density regime [3].

Recently, the plasma performance has been examined by controlling the widths of intrinsic magnetic islands, which seem to be generated by an error field. A remarkable improvement was observed in plasma parameters in the high-density plasmas produced by pellet injection. When the intrinsic islands were minimized, the increment of W_p amounted to about 25% and the maximum W_p of 1.03 MJ was achieved in the last experimental campaign. This paper is intended to describe this improved plasma performance, realized by minimizing the intrinsic islands and represented by the maximum W_p of 1.03 MJ.

2. Magnetic islands

In helical systems, well-nested vacuum magnetic surfaces play an essential role for plasma performance. However, the flux mapping, carried out at R_{ax} = 3.6 m and B_t = 2.75 T, showed that there were an m/n = 1/1 island and 2/1 islands in the LHD. The maximum widths of these islands are about 8 cm and 5 cm, respectively [4]. The cause of the error field is not clear, but there are a variety of possibilities, for example, ferromagnetic material located around the LHD, the large misalignment of the coils and so on.

The intrinsic islands were demonstrated experimentally to be almost simultaneously eliminated, that is, to be minimized by a perturbation coil system [4]. The perturbation coil system was installed to the LHD for the local island divertor (LID), which has been proposed for remarkable improvement of plasma confinement like H-mode in tokamaks. Thus it can also widen the widths of the vacuum magnetic islands [5].

2. Experimental Results and Discussion

The effect of the intrinsic islands on plasma performance was studied at $R_{ax} = 3.6$ m and $B_t = 2.8$ T. The port-through power of NBI and launching power of ion cyclotron range of frequency are 5 MW and 2 MW, respectively. Plasma discharges with a methane puff were conducted before this experimental series of high-density pellet plasmas, relevant to the intrinsic islands.

A carbonization effect was expected from methane puffing, but its effect on our experiments was not clarified.

Figure 1 shows temporal evolutions of typical LHD discharges. Five pellets were injected from 0.5 s to 0.7 s, which increased $\bar{n}_e$ beyond the 1×10^{20} m^{-3} in this short time. While W_p behaves in an adiabatic condition at the pellet injection, it rises slowly due to confinement improvement by a density increase [6]. It was found by minimizing the intrinsic islands that W_p was improved, compared with W_p in the configuration with the intrinsic islands, and reached the maximum value of 1.03 MJ. The increment of W_p amounted to about 25 %. A large difference was also observed between $\bar{n}_e$ in the two discharges in Fig. 1(b), and this causes the difference in W_p, as predicted by the scaling law. The relation of $\bar{n}_e$ versus W_p is plotted in Fig. 2. The solid and dotted lines represent those relations predicted by the International Stellarator Scaling 95 (ISS95) [7] and one improved by a factor of 1.5, respectively. The confinement enhancement factor from the ISS95 is about 1.4 for these discharges. Therefore, the effect of minimization of the intrinsic

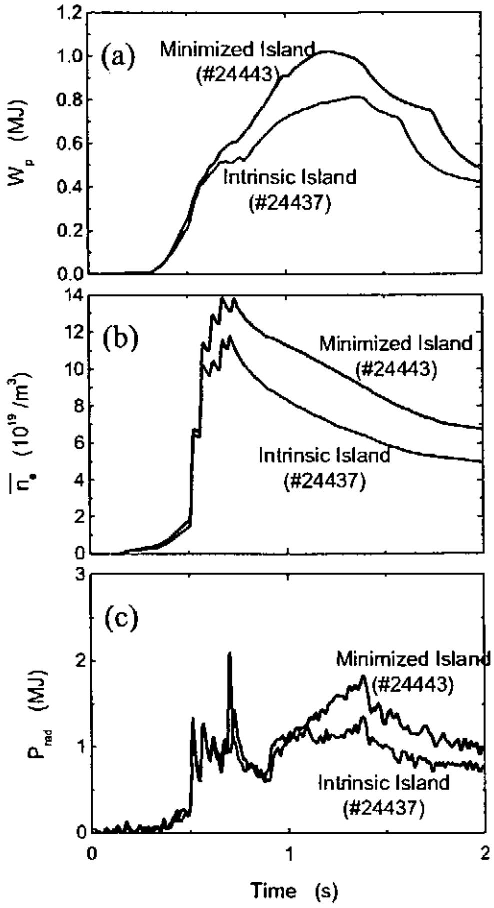

Fig. 1. Temporal behaviors of W_p, n_e and radiation power in the configurations with and without correction by a perturbation coil system.

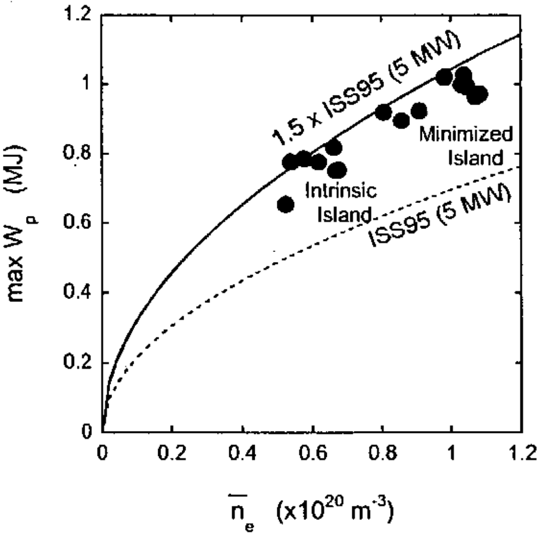

Fig. 2. Relations of n_e versus W_p in the configurations with and without correction by a perturbation coil system.

islands should be recognized as the extension of preferable confinement in the higher density regime. It also should be noted that the limitation of W_p is not caused by the deterioration of confinement, but by the density limit arising from the existence of the intrinsic islands. In Fig. 1(c), the radiation power, measured by a bolometer, shows little difference between the two discharges before $t \sim 1.2$ sec. At this time, the five pellets are already injected and W_p's begin to be saturated. The emissivity profile evolutions also indicate that the intense-radiation areas are located at $\rho \sim \pm 1.0$ in both cases, and the radial radiation profiles are almost the same in this period. Thus, the reason for the density increase is not attributed to impurity behavior.

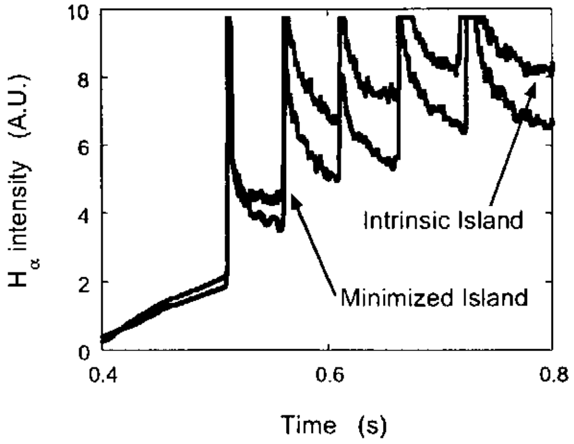

Fig. 3. H_α radiation in the discharges in the configurations with and without correction by a perturbation coil system.

A large difference was observed between the H_α radiation in the discharges with and without the minimization of the islands, as shown in Fig. 3. After the pellet injection, the H_α radiation in the discharge with the minimized islands was found to be smaller than that with the intrinsic islands, indicating that the former particle flux towards the wall is smaller than the latter particle flux. This was also demonstrated by the divertor fluxes, which were measured with Langmuir probes located on the divertor plates. Figure 4 shows the radial n_e profiles measured before and after the first and second pellet injections and those during the second pellet injections, together with the normalized rotational transform angles. An important point is that n_e in the configuration with the intrinsic islands is higher in the edge region of $4.2 \text{ m} < R < 4.5 \text{ m}$ than that with the minimized islands. Especially, the high n_e values near the last closed flux surface of $R \sim 4.5$ m coincide well with the high particle fluxes towards the wall when the intrinsic islands exist. In this case, the ablation of the second pellet occurs mainly in the edge region, and an increase in n_e near the plasma center becomes small. The high density in the edge region is considered to promote the ablation of the pellet, although the dependence of the ablation on n_e is weaker than that on T_e. In the case of the magnetic configuration with the minimized islands, the ablation of the second pellet occurs mainly near the plasma center, and a large increase in n_e is observed there. This is proved by the fact that n_e around $R = 4$ m during the ablation with the minimized islands is much higher than that with the intrinsic islands, indicating that the size of the pellet passing there is larger in the former case than that in the latter case. It should be noted that n_e around the $m/n = 1/1$ island is high, although the reason is not clear at this stage. The reason why the ablation is quickened in the presence of the islands is not clear either.

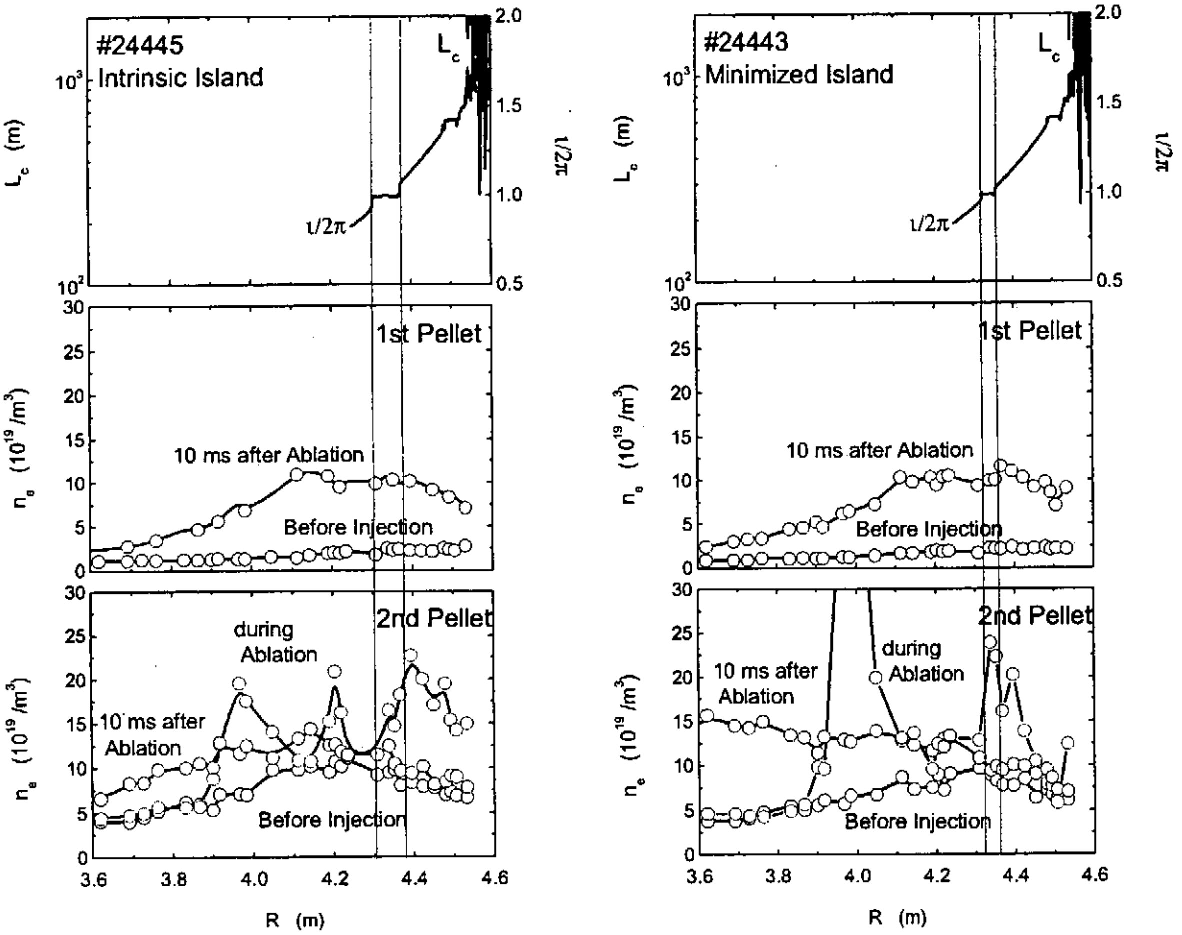

Fig. 4. Radial n_e profiles measured before and after the first and second pellet injections and those during the second pellet injections, together with the normalized rotational transform angles, in the configurations with and without correction by a perturbation coil system.

Summary

The maximum stored energy of 1.03 MJ was achieved by minimizing the intrinsic magnetic islands. When the intrinsic islands exist, the pellet ablation occurs mainly in the edge region, and a large amount of plasma flows to the wall quickly, leading to a decrease in the density, and hence, a decrease in the stored energy.

References

[1] Iiyoshi A et al 1999 Nucl. Fusion 39,1245.
[2] Yamada H et al 2000 Phys. Rev. Lett. 84, 1216.
[3] Sakamoto R et al 2001 Nucl. Fusion 41, 381.
[4] Komori A et al 2001 Phys. Plasmas 8, 2002.
[5] Komori A et al 1997 Fusion Energy 2, 3.
[6] Murakami S et al 1995 Trans. Fusion Technol. 27, 256.
[7] Stroth U et al 1996 Nucl. Fusion 36,1063.

CONFINEMENT OF FAST IONS PRODUCED BY NBI ON LHD

M.Osakabe, Y. Takeiri, T.Mutoh, Y.Nakamura, R.Kumazawa, T.Shimozuma, K.Tsumori,
K.Ikeda, O.Kaneko, Y.Oka, M.Isobe, M.Sasao, A.Krasilnikov*1, T.Ozaki, Y.Nagayama,
K.Narihara, T.Tokusawa, S.Morita, K.Kawahata, N.Ohyabu, O.Motojima, and
LHD-Experimental Group

National Institute for Fusion Science, Toki 509-5292, Japan
*1 *Troitsk Institute for Innovating and Fusion Research, TRINITI, Toroitsk 142092, Russia*

1.Introduction

The Neutral Beam (NB) heating campaign has been started on LHD since 1998.[1,2] The confinement of fast ions is one of the most important issues on helical devices since the large helical ripple plays an important role on the topology of the fast ion orbit. Concerning on the fast ion studies on LHD, (a) the confinement of NB-particles during their slowing-down processes, (b) interactions between fast ions and instabilities and/or ICRF-induced-waves, and (c) the confinement property of fast ions in the presence of electric fields are the important topics to be studied.

During the 3rd-cycle of LHD, NB short-pulse injection experiments, so called NB-blip experiments, were performed for ICH sustained plasmas to examine the confinement of NB-particles on LHD. In this experiment, a strong enhancement of pitch angle scattering was observed for ctr.-NB blip injection at a fast neutral analyzer whose line of sight is perpendicular to the magnetic field of lines, while no significant responses are observed for co.-NB blip injection. In this paper, we will show the result of the NB-blip experiments done in 3rd- and 4th- cycle of LHD, and show the analysis of this phenomenon.

2. Experimental Set-Up

On LHD, two of negative-ion based Neutral Beams (NB's) are injected tangentially. One is injected to co.-direction and another is to ctr.-direction.[3] Each beam line has two ion sources. These two ion sources are placed horizontally and have different tangency radii(R_t) of NB-injection. One of the advantage of the negative-ion based NB is that it consists of single energy component. Thus, the analysis on the NB particle confinement and on the heating characteristics become simple compared to positive-ion based NB's.

Two of electrically cooled Silicon diodes were adopted as Fast Neutral Analyzers (Si-FNA).[4] One is installed on the tangential-port for co.-NB detection. Another is installed on the lower-port of LHD, whose line of sight is perpendicular to magnetic field lines. The advantage of Si-FNA is simple, compact and economical compared to the conventional neutral particle analyzer. Thus, it makes easier to have measurements from various locations.

During the experiment shown in this paper, the magnetic axis of LHD was set to 3.6m, which is the standard configuration of LHD. The magnetic field strength was 2.75T at the axis. Two of ICRF-antennas were used to sustain the plasmas and launched the ICRF-wave of 38.46MHz in the experiment shown here.

3. Experimental results and discussions

Figure 1 shows the result of NB-blip experiment done in 3^{rd}-cycle. The short-pulse (20msec) NB is injected to ICH (P_{ICH}=~1MW) sustained plasmas with a cycle of 300msec. The electron density ($\bar{n}_e$) was about 1.0×10^{19} [m^{-3}] and stayed almost constant during the NB-injection. As is seen on Fig.1, big spikes were observed for perpendicular Si-FNA signals for ctr.-NB injection, while no significant response was observed to the co.-NB injection. Due to the ion source trouble of ctr.-NB injector, the NB-power of ctr.-NB was about the third of the co.-NB power. In the 4^{th}-cycel of LHD, similar experiments were performed for NB-sustained plasmas and low power ICRF-sustained plasmas (P_{ICH}=~0.4MW). During these experiments, no significant responses of perpendicular Si-FNA were observed in conjunction with NB-injection. These results indicate the phenomenon shown at the NB-blip experiment during the 3^{rd}-cycle is the enhancement of pitch angle scattering which correlates to ICH induced wave and has a dependence on the ICH-power. Figure 2 shows the change of Si-FNA spectra during the NB-blip experiments at 3^{rd}-cycle. The red curves in the contour plot show the slowing-down curve of the NB particles at various plasma locations. Temporal behavior of the tangential Si-FNA spectra at co.-blip injection is well described by the classical slowing-down theory. The temporal behaviors of Si-FNA spectra

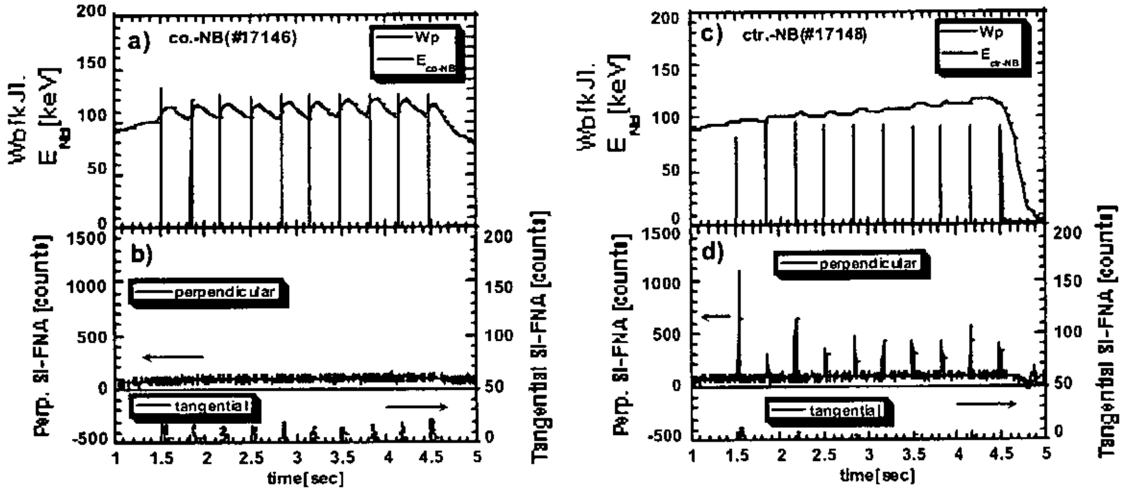

Fig.1 a) Stored Energy and NB injection energy, and b)signals of perpendicular and tangential Si-FNA at co.-NB blip experiments. c) and d) shows these at ctr.-NB blip experiments, respectively.

at ctr.-blip injection show that the enhancement of the pitch angle scattering occured at the edge of plasmas where ρ≥0.7. The enhancement was significant at the energy around 50-keV.

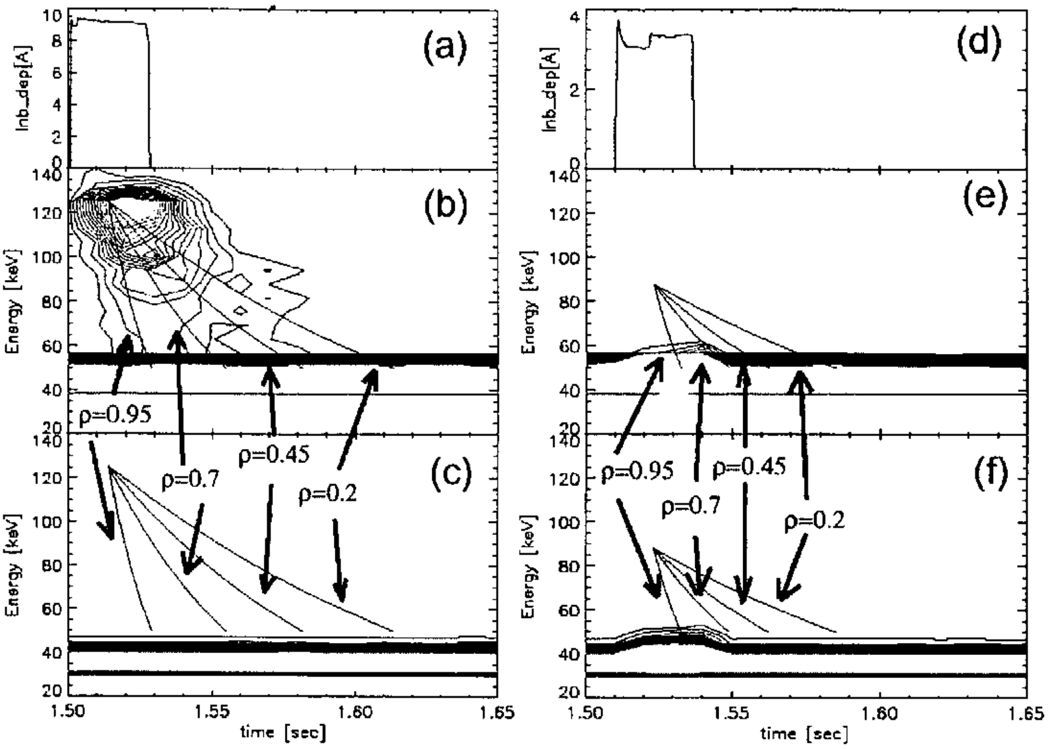

Fig. 2 a) NB deposition current to plasmas, b) contour plot for tangential Si-FNA spectra and c) contour plot for perpendicular Si-FNA for co.-NB blip injection. (d),(e) and (f) are these for ctr.-NB blip injection. Red curves in contour plots show the slowing-down curves of NB-particles at various location of plasmas.

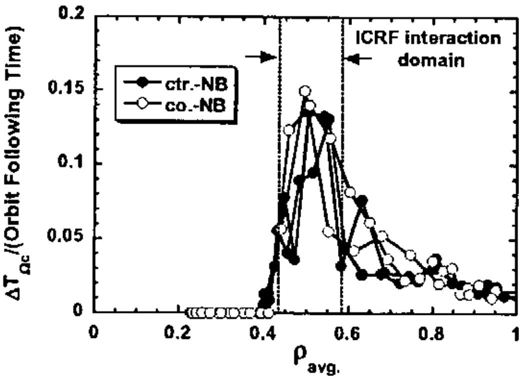

Fig.3 Normalized time of particles staying in the ICH resonance region. The time is normalized by the orbit following time of the calculation.

The orbit topology difference of co.- and ctr.-passing particles is one of the candidates as the explanations for this phenomenon. To examine these effects on the ICH induced pitch-angle scattering enhancement, the first orbit calculations were performed by taking launching-points of orbit calculations on the center lines of ion sources of NB-injectors. Figure 3 shows the length of time that the particles are staying in the ICRF resonance region. The x-axis of the figure denotes the averaged ρ along the particle orbit. The Doppler effect is taken into an account as the width of the resonance layer and the $k_{//}$ is assumed to be $0.5[m^{-1}]$. For both co.- and ctr.-passing particles, the ions traveling around the edge of the plasmas are passing

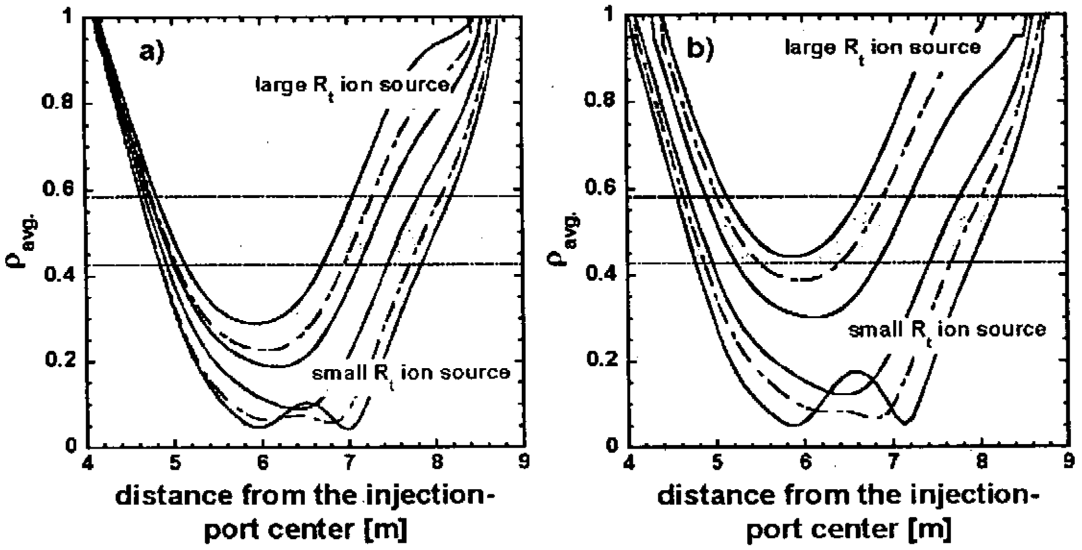

Fig.4 The $\rho_{avg.}$-distribution along NB flight paths for (a)co.-NB and (b) ctr.-NB injectors. The yellow regions show the ICRF interacting domains where the particle launched from the sight line of ion sources enters ICRF-resonance region, frequently.

through the ICRF resonance region ($\rho_{avg.} \geq 0.4$). Especially, particles traveling between $\rho_{avg.} = 0.43$ and 0.58 stay longer in the resonance region than other particles. In figure 4, the $\rho_{avg.}$-distribution along NB flight paths for co.- and ctr.-NB injectors are shown, the beam width is taken into an account in the figure. Due to the difference of the orbit topology between the co.- and ctr.- passing particles, the ctr.-NB injector has larger area of ICRF interacting domain. This is consistent with the results observed at NB-blip experiment. Farther analysis and experiments are necessary to get an agreement between experiments and analysis about the location of ICRF interacting domain.

References

[1] O.Motojima *et al.*, Phy **6**,143 (1999).

[2] M. Fujiwara *et al.*, Plasma Phys. Controlled Fusion **41**, B157(1999).

[3] O.Kaneko *et al*, Proceedings of 16th IAEA Fusion Energy Conference, Motreal, Canada, 7-11 October 1996, Vol.3, p.539.

[4] M.Osakabe *et al*, Rev. Sci. Instrum. **72**, 788(2001)

CHARACTERISTICS OF REHEAT-MODE DISCHARGES IN LARGE HELICAL DEVICE

S.Morita, M.Goto, T.Morisaki, S.Masuzaki, K.Tanaka, K.Narihara, S.Sakakibara, S.Ohdachi, K.Toi, S.Inagaki, K.Ikeda, O.Kaneko, K.Kawahata, A.Komori, J.Miyazawa, O.Motojima, S.Muto, Y.Nagayama, K.Nishimura, N.Ohyabu, Y.Oka, M.Osakabe, B.J.Peterson, R.Sakamoto, H.Suzuki, Y.Takeiri, T.Tokuzawa, K.Tsumori, H.Yamada and LHD experimental group

National Institute for Fusion Science, Toki 509-5292, Gifu, Japan

1. Introduction

Improvement of plasma performance after turning off gas puffing ("reheat-mode") has been widely observed in relatively small-scale helical devices such as CHS [1], ATF [2] W7-AS [3]. A large increment of plasma stored energy and an improvement of energy confinement are observed in the reheat-mode discharges. The reheat-mode appeared not only in NBI case but also in ECH and ICRF cases. It is strongly suggested that the cause of the reheat-mode is not simply related to a recovery of the input power and originates in the transport phenomenon due to a change of the edge parameters. Neutral particle effects, however, were so big in such devices. For example, the density profile was largely affected by the edge neutral behavior [4]. Then, unclear points remained for understanding the physical mechanism of the reheat-mode in addition to a lack of temporal and spatial information.

In LHD [5] the LCFS is surrounded by an ergodic layer of which the thickness ranges between 1 and 7cm at the O-point and depends on magnetic axis position (see

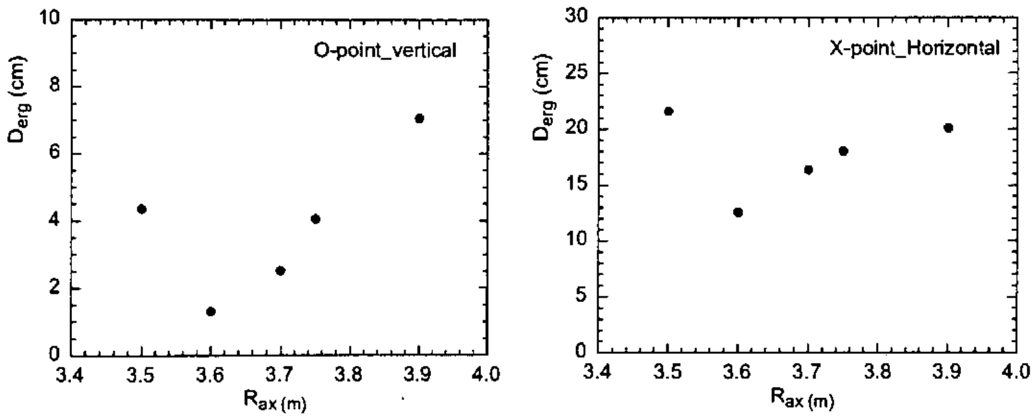

Fig.1 Thickness of ergodic layer averaged between inside and outside points (left: O-point at vertically elongated position, right: X-point at horizontally elongated position.)

Fig.1). Here, the D_{erg} is taken at a region with connection length, Lc>100m. The edge temperature of the main plasma ($\rho=1$) normally exceeds 100eV. Then, hydrogen neutrals and radiation from light impurities are located in the ergodic layer surrounding the main plasma. Inserting a limiter, density profiles did not change in LHD, whereas those in CHS changed from hollow to peaked by an increase in reflected particles from the limiter [4]. The direct effect on the neutrals was completely removed from the plasma core of LHD. Therefore, it has been thought unlikely that the reheat-mode appears in LHD.

2. Reheat-mode discharges in LHD

After starting NBI experiments the reheat-mode operation was tried, and magnetic axis (R_{ax}) dependence was investigated in order to make clear the response to the ergodic layer thickness. A clear increment of W_p was observed after switching off the gas puffing at the R_{ax}=3.70m position. Typical results are shown in Fig.2. The increment of W_p in the R_{ax}=3.60m position is very small. In the R_{ax}=3.75m position the operation related to density control becomes considerably difficult because of the thick ergodic layer. The edge temperature at ρ=1 in the R_{ax}=3.60m position is higher than the case of R_{ax}=3.70m [6]. Then, the recovery of the edge temperature in R_{ax}=3.60m is relatively small (In LHD the best confinement is obtained in the R_{ax}=3.60m position). These results indicate that the existence of the ergodic layer plays an important role for the reheat-mode discharge. A direct reason is a recovery from a large drop of the edge temperature at high-density region due to the low τ_p in the ergodic layer.

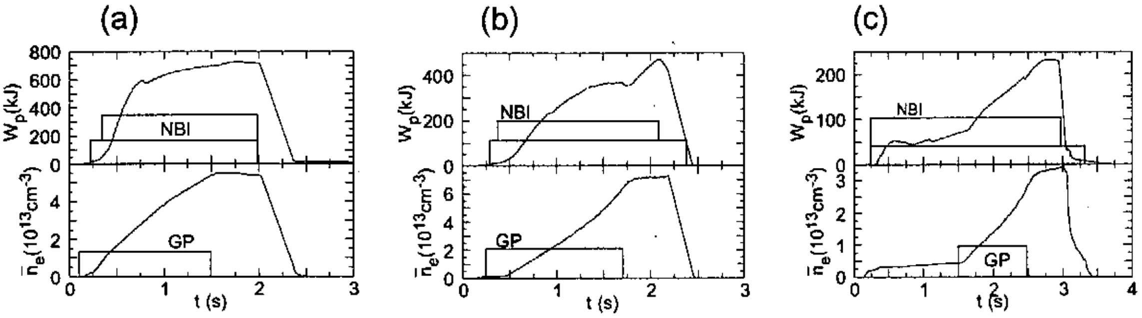

Fig.2 Reheat-mode operation during NBI discharge (upper: plasma stored energy W_p, lower: line-averaged density $<n_e>$). (a) R_{ax}=3.60m, (b) R_{ax}=3.70m, (c) R_{ax}=3.75m.

3. Behavior of the electron temperature

A typical result of the electron temperature behavior in R_{ax}=3.70m position is shown in Fig.3(a). Constant gas puffing is switched off at t=1.7s. After switching off the gas puffing the W_p increases from 370kW (t=1.7s) to 480kJ (t=2.1s). The peak W_p at t=2.1s gives a confinement improvement of 30% against ISS-95 scaling, although the gas puffing phase just behaves as the ISS-95 scaling. Unfortunately in this discharge the ICRF pulse is applied during 0.3s from t=2.0 to 2.3s and the NBI#1 pulse is turned off at t=2.1s. Then, the linear increase of the W_p is suddenly stopped at t=2.1s. The temporal behavior of electron temperature measured from Thomson scattering is shown in the bottom trace. The edge temperature at $\rho=0.95$ increases with a time delay of 40ms after switching off the gas puffing. At this moment, however, the central temperature at $\rho=0$ is still drops. The temperature rise at the edge region propagates toward the plasma center with the same time scale as energy confinement time (=140ms). After 170ms (t=1.87s) the electron temperature goes up with edge and core regions until t=2.1s at which the NBI#1 is turned off. From these results we can clearly understand that the reheat-mode is a pure transport phenomenon accompanied with confinement improvement. The electron temperature profiles are traced in Fig.3(b). The profiles are taken at times of t=1.7s (gas puffing off), 1.86s (end of the heat propagation) and 2.10s (end of reheat-mode). It is understood that the temperature recovers in the whole region of the plasma. The main part of the increase in W_p, of course, originates in the edge temperature rise.

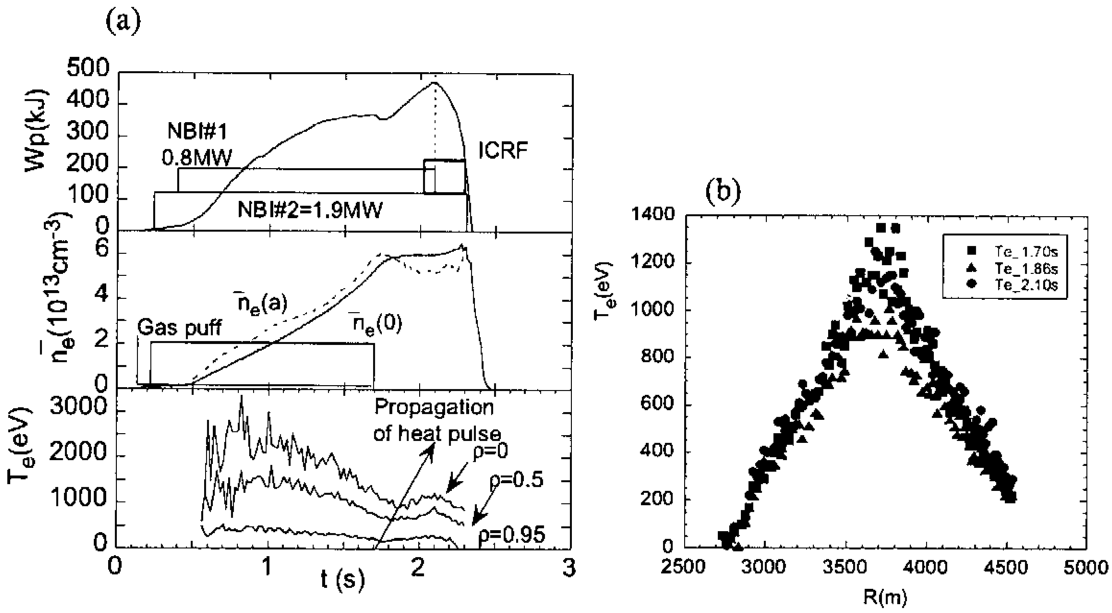

Fig.3(a) Temporal behaviors of W_p, $<n_e>$ and T_e. Gas puffing is switched off at t=1.7s.

(b) Electron temperature profiles measured from Thomson scattering at t=1.7, 1.86 and 2.1s.

4. Behavior of the electron density

It was reported that density profiles become peaked during the reheat-mode [1], although the mechanism was unclear at the moment. In LHD an 11-channel interferometer is installed to get the density profile with a good time resolution. Results from LHD are shown in Fig.4 (the discharge is the same as before). We can see from Fig.4(a) that the density profile becomes peaked after switching off the gas puffing, and we can understand the reason seeing the temporal density behavior (see Fig.4(b)). An important issue for the mechanism can be pointed out to be an existence of the inward flow of particles supplied from the gas puffing and a difference between particle confinement times of core (0.3s) and plasma edge (0.01s). After switching off the strong gas puffing the supplied particle still moves toward the plasma center. The density in ρ=0 and 0.45 continuously goes up at t=1.8s, whereas the edge density in ρ=1.05, 1.00 and 0.90 begins to drop. This change in the density profile continues until t=2.1s, and finally such a peaked density profile is performed. The improvement of the energy confinement also continues until t=2.1s with the formation of the peaked density profile.

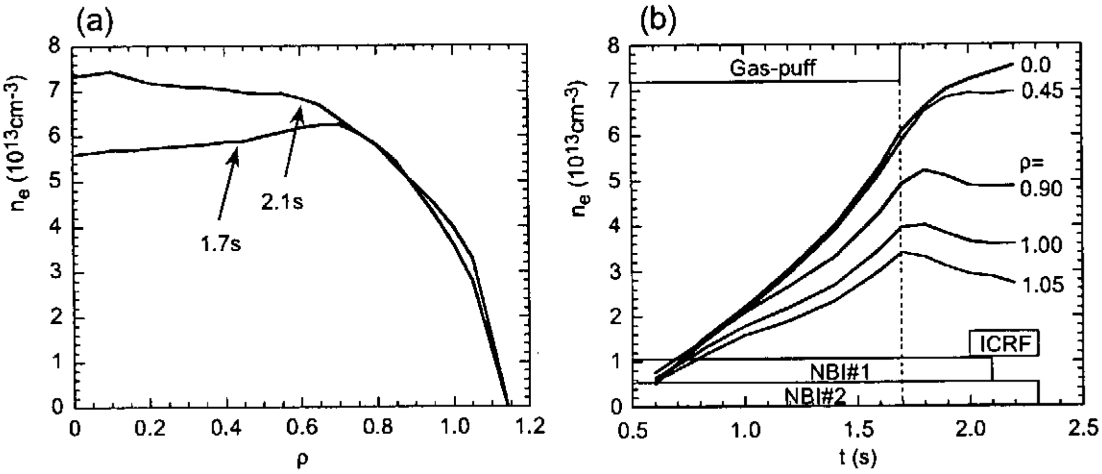

Fig.4(a) Electron density profiles after Abel inversion at t=1.7s and 2.1s. (b) Temporal behavior of electron density as a parameter of ρ (=<r>/<a>).

5. Conclusions

1) Reheat-mode was observed also in LHD. Thickness of the ergodic layer is strongly related to the confinement improvement during reheat-mode.

2) Heat propagation from edge to core was observed. The core temperature is strongly correlated to the edge temperature.

3) Peaked density profile was observed. It can be explained in combination with the inward flux from gas-puffed particles and a difference in the particle confinement time between core and edge region.

4) There possibly exists a relation between density peaking and confinement improvement.

References

[1] S.Morita et al., Proc. 14th IAEA conf., (IAEA, Vienna, 1993) IAEA-CN-56/C-2-5.
[2] S.Morita et al., ORNL report, ORNL/TM-11737 (1991)
[3] S.Morita et al., IPP-report (Garching, Germany), no.199 (1995)
[4] S.Morita et al., 16th IAEA conf., (IAEA, Vienna, 1997) IAEA-CN-64/CP-3.
[5] O.Motojima et al., Phys. Plasma 6, 1843 (1999).
[6] N.Ohyabu et al., Phys.Rev.Lett. 84, 103 (2000).

Characteristics of MHD Instabilities Excited in Edge and Core Regions of the LHD Plasmas

K. Toi, S. Ohdachi, S. Yamamoto[1], S. Sakakibara, H.Yamada, A. Weller[2],
K.Y. Watanabe, Y. Narushima, K. Narihara, K. Tanaka, I. Yamada,
T. Tokuzawa, S. Masuzaki, S.Morita, M. Goto, J. Li[3],
K. Kawahata, N. Ohyabu and LHD Experimental Group

National Institute for Fusion Science, Toki 509-5292, Japan
[1] Dep. of Energy Engineering Science, Nagoya Univ., Nagoya 464, Japan
[2] Max-Planck-Institute fur Plasmaphysik, D-85748 Garching, Germany
[3]Academia Sinica, Institute of Plasma Physics, Hefei 230031, China

1. Introduction

The LHD experimental campaign in 1999 demonstrated that the plasma was fairly stable and did not suffer from serious plasma collapse caused by pressure driven modes such as ideal/resistive interchange modes and ballooning modes. The global plasma beta $<\beta_t>$ was increased more than 2 % [1]. Observations of magnetic fluctuations appeared to be consistent with the linear stability against Mercier modes and low n (n: toroidal mode number) interchange modes. These pressure driven modes saturated at a relatively low fluctuation level. However, in the experimental campaign in 2000 where high heating power was injected up to 6 MW, they sometimes exhibited peculiar nonlinear evolutions and appreciably affected the plasma confinement on a certain discharge condition . It is important to perform detailed studies of nonlinear behaviours of the pressure driven modes excited near the edge and core plasma regions, because their suppression and excitation are closely linked to local energy transport around the mode location. This paper reports the nonlinear behaviours of pressure driven modes observed in LHD plasmas and their effects on global plasma confinement.

2. Edge MHD modes with several satellites (Edge Harmonic Modes)

In the edge region of LHD plasmas where the steep pressure gradient zone is often generated, pressure driven modes accompanying several satellites are excited there[2, 3]. Mode structures depend on the toroidal plasma beta $<\beta_t>$ and the magnetic axis position. When one NBI pulse is occasionally turned off or the electron density is linearly increased up to relatively high value ($\approx$5-6 $\times 10^{19}$m^{-3}) by gas puffing, they rapidly grow and suddenly saturate within 1-2 ms, of which time scale is much shorter than the global energy confinement time and magnetic diffusion time. A typical discharge where the edge localized harmonic modes (EHM) are excited is shown in Fig.1. A typical frequency spectrum of magnetic fluctuations is shown in Fig.2. At least, 5th harmonics are clearly

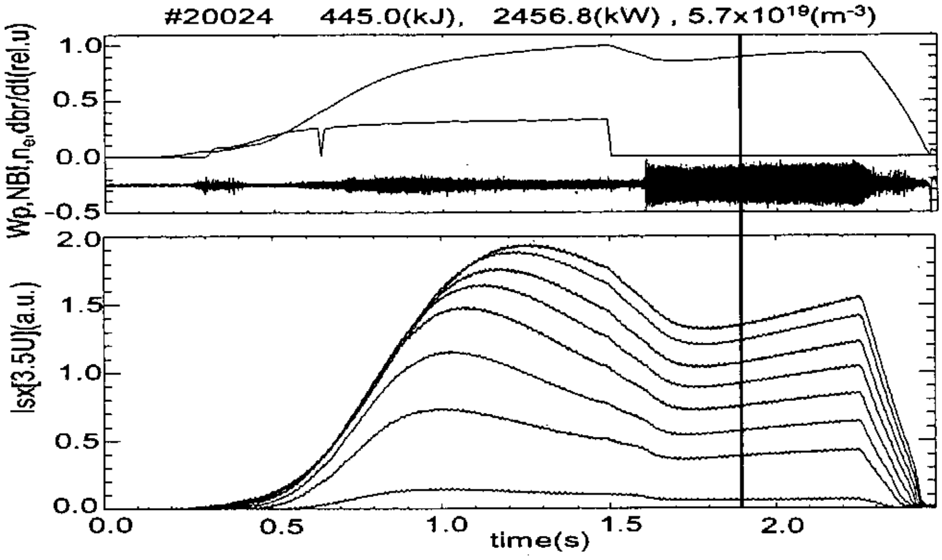

Fig.1 Discharge waveform with EHM-fluctuations where the total NBI heating power is ~3.2 MW. SX-signals from r/a~0.5 to ≈1 are shown.

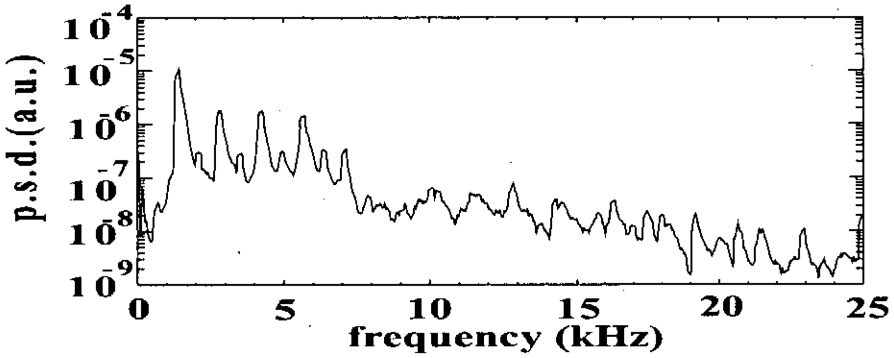

Fig.2 Frequency spectrum of magnetic fluctuations in the time window of 1.894~1.896 s.

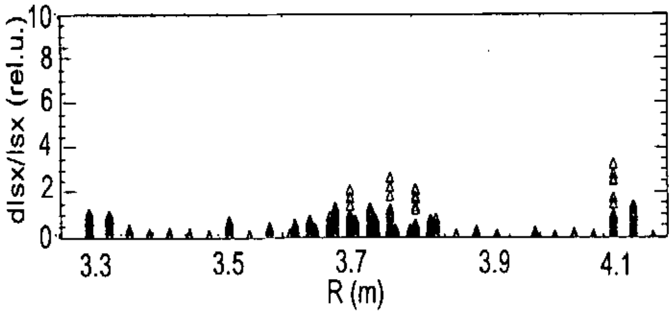

Fig.3 Relative amplitude of SX-fluctuations along the major radius.

seen in the frequency range less than 10 kHz. The toroidal (n) and poloidal (m) mode numbers for the fundamental mode with the lowest frequency ($f=f_0\approx1.2$ kHz at t=1.89 s) are evaluated to be n=3 and m=2 using a magnetic probe array. Soft X-ray (SX-) detector array also detects the fluctuations and provides the information of m=2. Moreover, the SX- fluctuations are localized near the plasma edge (R > 4.1 m and R < 3.3 m) (Fig.3). According to VMEC calculation, the rational surface of the rotational transform 1/q=3/2 is located just outside the last closed flux surface(LCFS) , which means it is inside the ergodic layer. In the ergodic layer just outside LCFS, the pressure gradient seems to still be finite. The EHMs slightly but clearly decrease the plasma stored energy by ≈3 % (Fig.1). In the phase that EHMs persist, the other satellites having the frequencies of $f_0/2$, $3f_0/2$, $5f_0/2$ and so on are often excited(Fig.2). Note that these modes are very similar to the so-called edge harmonic oscillations(EHO) observed during so-called quiescent double barrier(QDB-) regime in DIII-D[4].

3. Edge harmonic modes with bursting character

As mentioned above, the edge harmonic modes EHMs are usually excited rapidly and persist continuously after quick saturation. In some cases with high heating power up to 6 MW where $<\beta_t>$ is only ≈0.6%, the EHMs exhibit bursting character and transiently depress the SX-signals from <r>/<a> ≈0.5 to ≈1 (Fig.4). It should be noted that the SX signals indicate the effect of the bursting EHMs reaches around half of the averaged minor radius <a>. The bursting EHMs appreciably decrease the stored energy Wp and transiently degrade the energy confinement time by up to 20% (Fig.5). The toroidal and poloidal mode numbers of the bursting EHMs at the lowest frequency (f≈6 kHz) are n=4 and m=3. Again, the rational surface is located very close to LCFS or just outside LCFS. When resonant helical field perturbations dominated by the m=1/n=1 Fourier component is externally applied using so-called Local Island Divertor (LID) coils so that an existing m=1/n=1 island should be suppressed, the bursting character of EHMs are

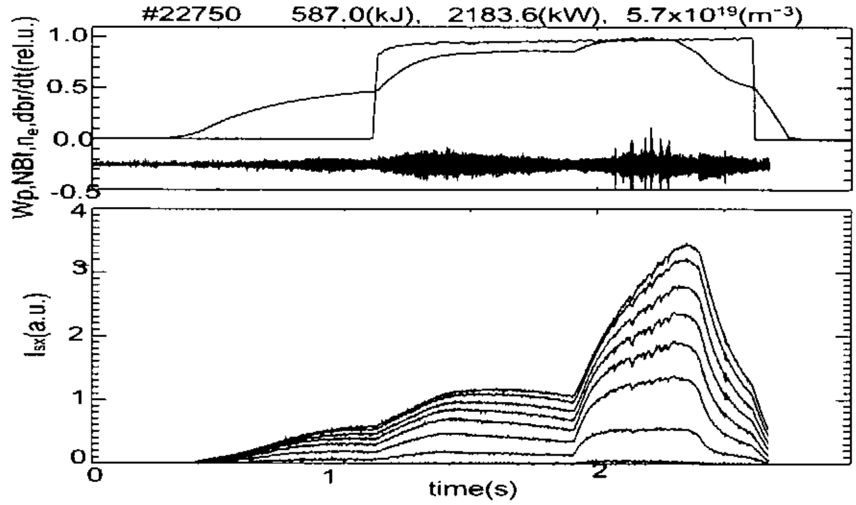

Fig.4 High power heating plasma with bursting EHMs, where ICRF power of 1.9 MW is injected in an NBI heated phase and total heating power is 5.6 MW. SX-signals from <r>/<a>≈0.5 to≈ 1 are shown.

clearly suppressed and Wp is smoothly increased(Fig.4). This might be caused by slight reduction in the pressure gradient near 1/q=3/2 surface through suppression of m=1/n=1 island. Also for the high temperature plasmas in the range of $<\beta_t> \approx 1\text{-}1.5$ %, the bursting modes sometimes affect the plasma confinement.

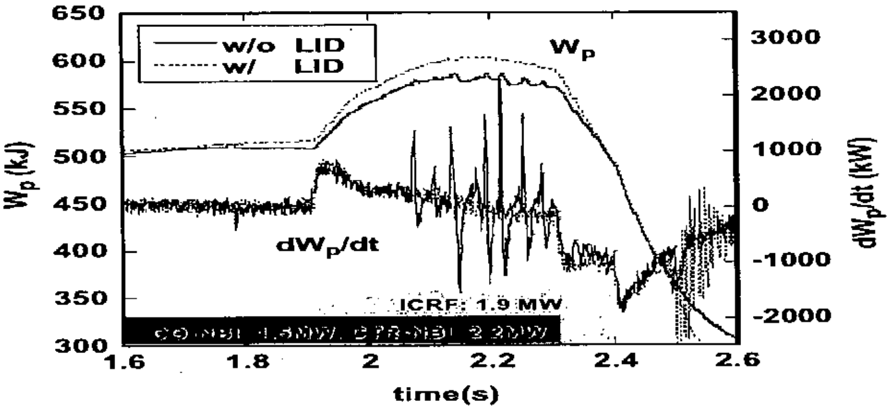

Fig.5 Time evolution of the stored energy and its time-derivative for two discharges without and with externally applied m=/n=1 resonant helical field perturbations.

4. MHD modes excited in the core region after ice pellet injection

After ice pellet injection, steep pressure gradient in the core region is transiently produced typically around the 1/q=1/2 rational surface. The magnetic shear at the rational surface tends to become small due to the increased in $<\beta_t>$. Indeed, m=2/n=1 pressure driven modes are often excited, inducing sawtooth like internal collapses. The effect of the internal collapse on plasma confinement is fairly small.

4. Summary

In LHD plasmas heated by a total power of about 6MW (NBI and ICRF), continuous and bursting MHD modes often having many satellites (in this paper, dubbed EHMs) are exited near the plasma edge. The bursting modes degrade the plasma confinement transiently but appreciably. The bursting character of EHMs with m=3/n=4 was successfully suppressed by resonant helical field perturbation when the field was applied to reduce the size of existing m=1/n=1 island. The continuous EHMs are sometimes rapidly destabilized and then quickly saturate, accompanying a lot of satellites. Just after the ice pellet injection, m=2/n=1 modes are often excited in the plasma core region and lead to internal collapse, of which effect on the plasma confinement is small.

Referrences

[1] S. Sakakibara et al. Nucl. Fusion 2001 (in press).

[2] M.Takechi et al., J. Plasma Fusion Res. SERIES **3**, 113 (2000).

[3] S. Ohdachi et al., Rev. Sci. Instrum. **72**, 727 (2001).

[4] C.M. Greenfield et al., Phys. Rev. Lett. 86, 4544 (2001)].

Pellet-Induced Low Frequency Oscillations on the Large Helical Device

S.Ohdachi, S.Yamamoto[1], K.Toi, A. Weller[2], R.Sakamoto, H.Yamada,
K.Tanaka, T.Tokuzawa, K.Kawahata, S.Morita, M.Goto, S.Sakakibara
and LHD Experimental Group

National Institute for Fusion Science, Toki 509–5292, Japan
[1]*Dep. of Energy Engineering Science, Nagoya Univ., Nagoya 464–8603, Japan*
[2]*Max-Planck-Institut für Plasmaphysik D-857p48 Garching, Germany*

1 Introduction

Hydrogen ice pellet injection has been successfully utilized for particle fueling of the Large Helical Device (LHD)[1]. With the help of sequential injection of pellets, typically five in sequence, we can reach an operational regime with fairly high electron density, in excess of $1 \times 10^{20}\mathrm{m}^{-3}$. The highest performance of the LHD plasma is achieved in this regime, where the density is being slowly decreased from its maximum value and the density profile is being transiently peaked. It is important to study the pellet-plasma interaction in order to optimize the ice pellet injection scheme.

Low frequency oscillations immediately following the pellet injection into NBI-heated plasma have been found on LHD. Those are similar to the Snake[2]-like oscillations found in tokamaks, e.g., ALCATOR C-mod[3], JET[2], RTP[4] and TEXTOR[5]. The characteristics of the oscillations in tokamaks are summarized as follows; (1) mode frequency is very low (several hundreds of Hz ~ several kHz) with a poloidal mode number m = 1. (2) Oscillations appear in the SX radiations (SXR) and in the electron density fluctuations [2, 4, 5] and in the electron temperature fluctuations[5] using ECE measurement. (3) Oscillations are usually localized on the q = 1 rational surface. In RTP [4], formation of magnetic islands during ablation process has been found using Thomson scattering measurement with high space resolution. This observation supports the idea that oscillations are explained by the rotation of magnetic islands localized on the q = 1 magnetic surfaces. On the other hand, in the ALCATOR C-mod[3] tokamak, the peak of the oscillation are well outside the q = 1 surface. And m = 1 oscillations have been found in the Wendelstein 7-AS stellarator[6] where there is no q = 1 rational surface. Understanding of mechanism of this oscillations are in the still in the early stage. Here we present characteristics of pellet-induced low frequency oscillations found in LHD in detail.

2 Experiments

LHD is a Heriotron type device (l=2 / m=10) with the major radius R = 3.9 m and the minor radius $\bar{a}$ = 0.6 m. Pneumatic pipe-gun type injector is used to refuel the LHD plasma. Hydrogen ice pellets with a velocity of ~ 1 km/s (from outboard side) and ~ 0.2 km/s (from inboard side) can be injected with this.

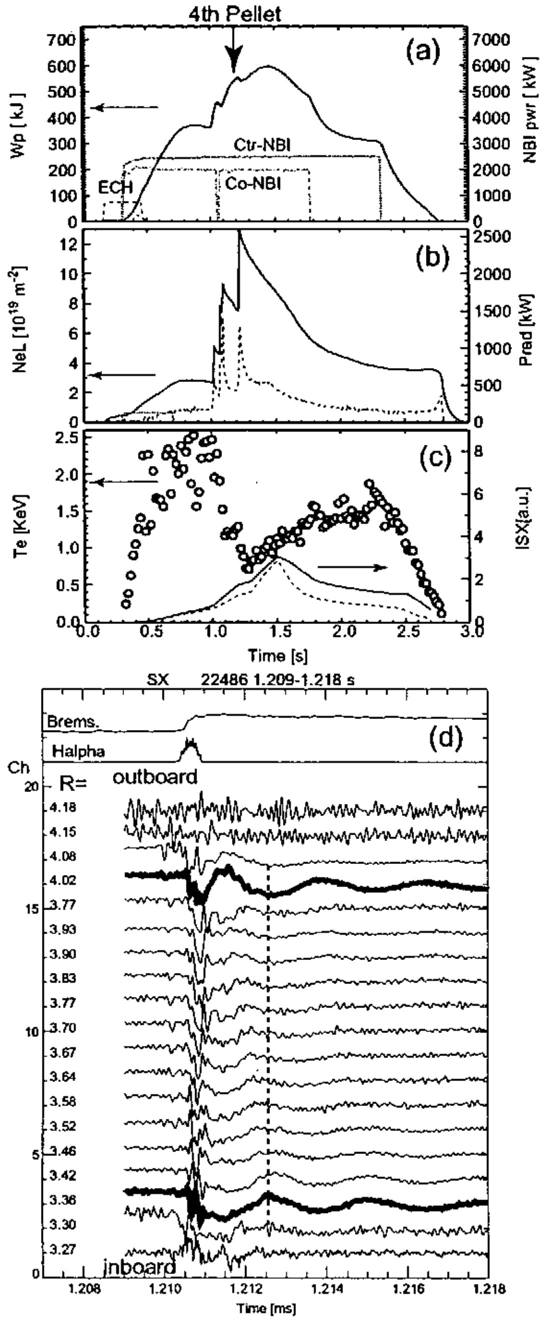

Fig.1: Time evolutions of the stored energy (a), the line density and the radiated power(b), the electron temperature T_{e0} and SXR at the center and the edge (c) are shown together. Fourth pellet(indicated by an arrow) make the oscillation at about 1.21 s. Extended view of H_α and SXR are shown in (d).

Time evolution of plasma parameters is shown in Fig.1(a)–(c) when oscillations are observed. Expanded view of signals from a soft X-ray (SX) detector array system[7] which views the plasma at a vertically elongated section of LHD is shown in Fig.1(d). Fast H_α measurement and the visible bremsstrahlung measurement are also shown to compare the timing of the pellet injection. After the ablation phase indicated by H_α peak, slow ($f \sim 400$ Hz) and dumping oscillation can be seen. Comparing the phase between inboard sight-line with outboard one (broad lines in Fig.1(d)), we find that poloidal mode number $m = 1$. Measurements at a different toroidal position, where the plasma is horizontally elongated, also show that $m = 1$ structure. Phase difference between two arrays is consistent with toroidal mode number $n = 1$, though measurements at only two toroidal positions are not conclusive. The oscillations persist for about 10 ms typically.

The fluctuation amplitude and the relative phase of the oscillations as a function of major radius R are shown in Fig. 2. Two peaks in the amplitude (Fig.2(a)) are located slightly inside the $1/q = 1$ surface ($\rho = 0.7 \sim 0.9$). The position is independent of the conditions of pellets, e.g., size or speed or penetration depth of them. However, in the low magnetic field experiments ($B_t = 0.75$ T, dashed lines in Fig. 2), where the magnetic surfaces are shifted outboard by Shafranov Shift in high beta plasma, inner peak also moves outboard. The disagreement with the position of $q = 1$ surface is larger than that in the low beta ($B_t = 2.8$T) case. Estimation of the rotational transform profile and the averaged radius ρ are shown in Fig.2(a) and its axes above. This movement can be explained better by deeper penetration of pellets with low temperature plasma in high beta experiments than by movement of the $q = 1$ rational surface. It is possible the oscillation is not localized on the q = 1 surface in LHD.

3 Discussion

3.1 Density fluctuations or Temperature fluctuations?

While the pellet is being ablated, modulation of the H_α radiation, which suggests inhomogeneous ablation, are also observed (Fig.1(d)).

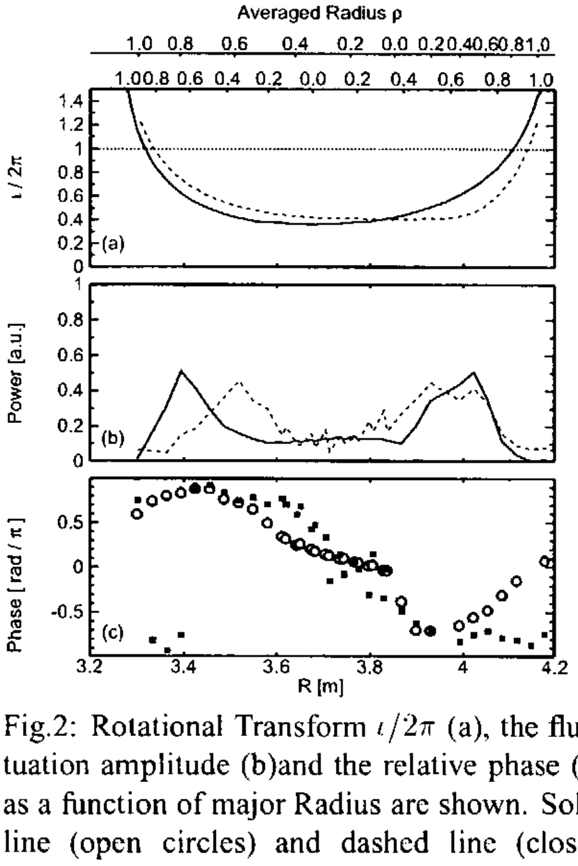

Fig.2: Rotational Transform $\iota/2\pi$ (a), the fluctuation amplitude (b)and the relative phase (c) as a function of major Radius are shown. Solid line (open circles) and dashed line (closed square) are high beta (β_t = 0.5%, #22486) and low beta (β_t = 1.4%, #23154) case, respectively. Estimation of the averaged radii assuming standard pressure profile are also shown in (a) for reference.

Simultaneously, faster fluctuations (~ 10 kHz) propagate or rotate from the outboard side to the inboard side are also observed. Since this modulations are correlated well with the density fluctuations measured by FIR interferometer, these can be explained by density fluctuations. However, slower waves, we are discussing, whose amplitude is as large as the fast oscillations, are not detected neither by the density measurement nor by the visible Bremsstrahlung measurement(Fig.1(d)). The SXRs depend on the electron density and temperature and the impurity density. Because fluctuations in the density and the impurity radiation are not large enough to account for the SXR fluctuations, the fluctuations are may be caused by the fluctuations in the electron temperature. However, We can not make a conclusive answer for this, because ECE measurements after the sequentially injected pellets are not available due to cutoff. Therefore, filter absorption method has been tested using two SX arrays equipped with beryllium foil of different thickness. Relative fluctuation levels are 25% and 20% with 15μm foil and 30 μm foil, respectively. It is not consistent with the idea – the electron temperature fluctuations cause the SXR fluctuations – since channels with thicker foil are more sensitive to the electron temperature. The origin of the SXR oscillations has not been understood yet.

3.2 When do the oscillations appear?

These oscillations are not always observed with pellet injections. We have found about 40 cases from 320 pellet injected discharges we checked. The criterion for their appearance will be key to understanding of this phenomena, however, no clear conditions, e.g. the size or the speed of pellets, the conditions of target plasma and so on, has been found. And this oscillations can be seen both in the hydrogen and the helium target plasmas.

In tokamak case, the appearance of the oscillations can be related to the pellets penetrating length and the position of the q = 1 rational surfaces. It is not the case with the LHD. Because the rotational transform profile of LHD is different from tokamaks; q = 1 surface is located in the relatively outer region (Fig.2 (a)). Thereby, almost every pellet can reach there including pellet injected from inboard side whose velocity is low (~ 200 m/s) due to the curved guiding tube. This slow pellet also make the oscillations sometimes.

3.3 Parameter dependence

Characteristics of the oscillations, i.e. the frequency, the decaying rate, etc. are compared with the experimental conditions. Unfortunately, no clear correlation has been found again; the frequency of the oscillations does not depend on B_t and depends weakly on the line averaged target plasma density (Shown in Fig. 3).

In summary, pellet induced sawtooth oscillations has been found in LHD. The frequency range, m/n = 1/1 mode structure is similar to Snakes found in tokamaks. Radial profile of amplitude of the mode suggests that they are not localized on q = 1 surface. The physical mechanism behind the oscillations has not been well understood. Further investigations are needed.

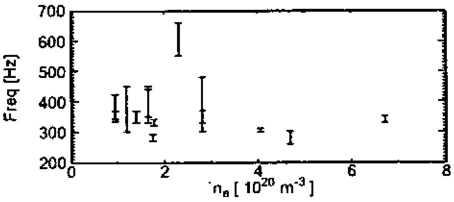

Fig.3: The frequency of the oscillations as a function of line averaged electron density. Error bars indicate the change of the frequency while decaying.

References

[1] R. Sakamoto *et al.*, Nucl. Fusion **41**, 381 (2001).

[2] A. Weller *et al.*, Phys. Rev. Lett. **59**, 2303 (1987).

[3] J. Parker *et al.*, Nucl. Fusion **27**, 853 (1987).

[4] D. Cruz *et al.*, Phys. Rev. Lett. **75**, 3685 (1995).

[5] K. Finken *et al.*, Plasma Phys. Control. Fusion **39**, 351 (1997).

[6] J. Lyon *et al.*, Proc. of 24th European Physical Society Conference on Controlled Fusion and Plasma Physics **21**, 1629 (1997).

[7] S. Ohdachi, K. Toi, M. Takechi, and S. Yamamoto, Rev. Sci. Instrum. **72**, 727 (2001).

PLASMA AND IMPURITY TRANSPORT MODELING OF NBI-HEATED LHD AND HELICAL REACTOR SYSTEMS

K. Yamazaki, M. Tokar[1], H. Funaba, B.J. Peterson, N. Noda,
A. Cooper[2], Y. Narushima, S. Sakakibara, K.Y. Watanabe, H. Yamada,
K. Tanaka, K. Ida, K. Narihara and the LHD Experimental Group

National Institute for Fusion Science, 322-6 Oroshi-cho, Toki, 509-5292, Japan
[1]Institut fuer Plsamaphysik, Forschungszentrum Jelich, D-52425 Juelich, Germany
[2]*Centre de Researches en Physique des Plasma, Ecole Polytechnique Federale de Lausanne, CH-1015 Lausanne, Switzerland*

Abstract

For the precise analysis of toroidal confinement systems, the Toroidal Transport Analysis Code "TOTAL" has been developed and applied to the Large Helical Device (LHD) plasmas and related reactor systems. The new LHD confinement scaling law is derived, which can extrapolate the present data to the reactor regime without confinement improvement.

Slow Relaxation oscillations called "breathing" have been analyzed using the TOTAL code and the physics simulation modeling with impurity sputtering process. The slight change in transport coefficient during oscillation is experimentally found, and roles of high-Z and low-Z impurities are clarified. The breathing waveform and the oscillation period are reproduced depending on plasma density by this modeling.

1. Introduction

Plasma confinement and related impurity behaviors are keys to getting high temperature plasmas and starting reactor plasma operations. In the Large Helical Device (LHD) the confinement times higher than the conventional scaling laws are achieved, which makes it possible to extrapolate the present database to the reactor regime [1]. So-called "breathing" phenomena [2,3] are found in LHD as a result of impurity dynamics. For the explanation and prediction of LHD and reactor plasma confinement, precise transport analysis is required. In this paper, "breathing" plasma analysis and reactor plasma projections are carried out.

2. LHD Transport Analysis Using TOTAL Code

2-1 TOTAL Code Development

For predictive simulation and experimental analysis of toroidal plasmas, a simulation code TOTAL (Toroidal Transport Analysis Linkage) has been developed as an extension of HSTR code [5]. This consists of a 3-dimensional equilibrium with ohmic and bootstrap currents and a 1-dimensional transport with neoclassical loss determined by ambipolar radial electric field as well as anomalous transport (empirical or drift turbulence theory).

2-2 Global Confinement Scaling and Reactor Plasma Projection

NBI-heated plasmas on LHD are analyzed using the TOTAL code. Different from the previous scaling laws, a new global confinement scaling law (New LHD scaling) by regression analysis has been obtained [1] based on heliotron-type experiments:

$$\tau_{NLHD\#1} = 0.263 P^{-0.58} \bar{n}_e^{0.51} B^{1.01} R^{0.64} a^{2.59}.$$

Units used here are $\tau_E(s)$, $P(MW)$, $\bar{n}_e(10^{20}m^{-3})$, $B(T)$, $R(m)$, $a(m)$, respectively. This scaling law suggested the strong gyro-Bohm like feature, which is different from previous scaling laws. This feature is also verified by local transport analysis near the edge region. Using this scaling low, Modular Heliotron Reactor plasma [1] can be predicted without confinement improvement.

2-3 Impurity Transport Analysis Using TOTAL Code

Consideration of the transport of impurities and their influence on plasma performance is one of important elements in a consistent predictive modeling. In particular, the development of "breathing" oscillations in LHD [2,3] gives an interesting example of impurity effects in helical devices.

The impurity dynamics is calculated using measured electron temperature and electron density. Figure 1 shows the breathing oscillation of measure input profiles and calculated radial electric field, radiation power and effective Z values. The initial total impurity density was assumed by the percentage of main plasma density. Here the recycling rates of all impurity ions are assumed to be unity. In this analysis, carbon, oxygen, and iron densities are assumed as 1%, 1% and 0.2 %, respectively. Their initial profiles are determined using coronal equilibrium model, and the time-variation of each charge-state impurity ions

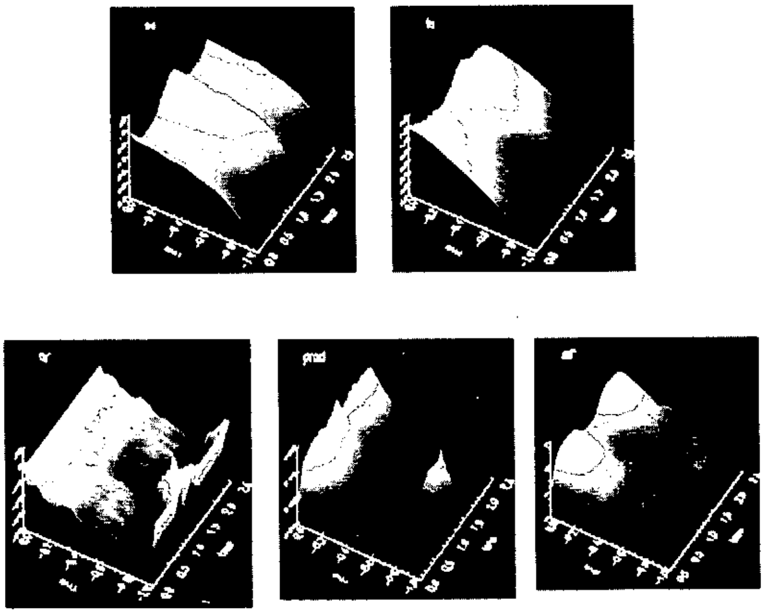

Fig. 1 Transport analysis on LHD plasma.
Upper raw: experimental data (n_e and T_e),
Lower raw: analyzed output (E_r, P_{rad} and Z_{eff})

is dynamically solved by the rate equation of each charge-state and the diffusion equation with the transport coefficient D of 1 m^2/s and without the inward flow (v = 0 m/s). The ambipolar electric field calculated from bulk plasma is negative (ion root), which contradicts with experimental observations. For precise determination of electric field, we might include impurity effects on the ambipolar flux calculation. The radiation profile has two peaks (central and near edge) corresponding to iron and low-Z (carbon and oxygen) impurities, which qualitatively agrees with experimental data.

Typical radial profiles of effective thermal diffusivity are shown in Fig. 2.

$$\chi_{eff} = -(Q_{NBI} + Q_{RF} - \frac{dW_P}{dt})/(n_e \frac{d(T_e + T_i)}{dr})$$

In higher density, detached small plasma and low-Z impurity radiation dominant phase, the thermal diffusivity is rather low. On the other hand, in the temperature increase, low radiation and larger attached plasma phase, the diffusivity is slightly high. This transport change might also contribute to the appearance of periodic relaxation oscillations.

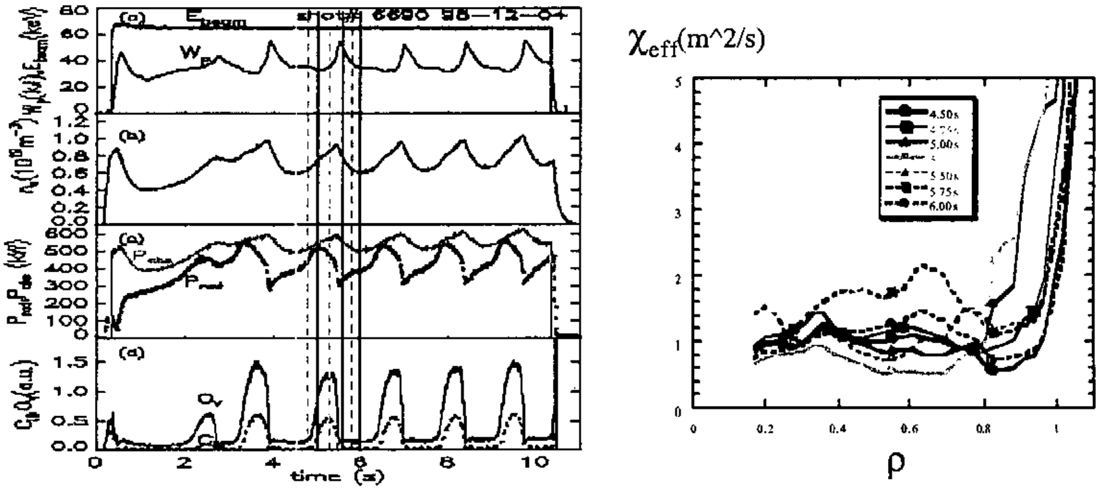

Fig.2 Breathing plasma waveforms and effective thermal diffusivity

3. Physics Modeling on Impurity-Induced Relaxation Oscillation in LHD

In discharges where the plasma touched wall elements of iron, an increase of the electron density in excess of a critical level led to slow with a period of a second oscillations in diverse plasma parameters, e.g., central and edge plasma temperature, integrated radiation losses and intensities of selected spectral lines, line averaged density, etc. A physical picture of this phenomenon proposed recently [5] implies the importance of radiation from both Fe ions in the plasma core and light impurities of C and O at the edge. In phases with a hot edge the sputtered iron particles penetrate into the plasma core and increase the central radiation losses. This leads to reduction of the heat outflow to the edge and detachment due to radiation of C and O. As a result the iron-sputtering source disappears and Fe ions diffuse out of the plasma. The growing heat flow to the edge causes its reattachment.

With an ultimate goal to perform a self-consistent 1-D time-dependent modeling of "breathing" oscillations by the code TOTAL this has been first run in its interpretive option to reconstruct the behavior of transport coefficients. The results for the effective heat conductivity are shown in Fig.2. A modeling of Fe ion transport gives a diffusivity of 0.15-0.25 m^2/s in agreement with that obtained by the code MIST [4]. These coefficients have been used in a simple numerical model elaborated to check the mechanism of "breathing" proposed in Ref.[5]. The model includes a heat balance for the plasma edge and core, the balance of the main particles and a 1-D time dependent description of the total density of Fe ions with a self-consistently computed source of iron neutrals due to physical sputtering of the divertor. As a result the time evolution of the plasma temperature at the last closed magnetic surface and at the device axis, of the line averaged density, total radiation losses and luminosity of light impurities can be simulated. Figure 3 shows an example of such calculations for an NBI power of 1MW. These results are in agreement with measurements including peculiarities of their time phasing. The observed increase of the oscillation frequency with plasma density n can be reproduced firmly in computations if one assumes that the impurity diffusivity varies proportionally to n as it is predicted by neoclassical theory.

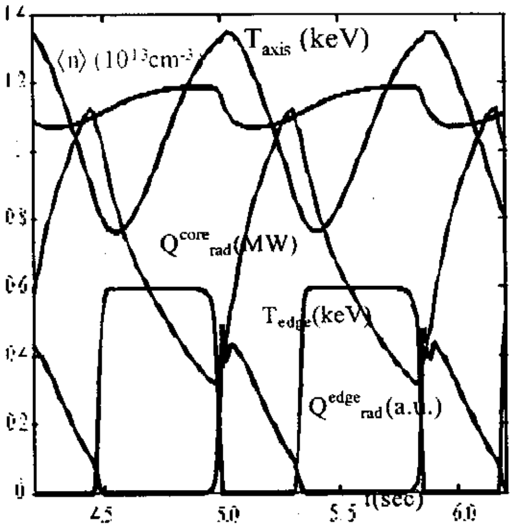

Fig.3 Results of Numerical Modeling

References

[1] K. Yamazaki et al., 18th IAEA Fusion Energy Conference (Sorrento, Italy, 2000) FTP2/12

[2] Y. Takeiri et al., Plasma Phys. Control. Fusion 42 (2000) 147.

[3] B.J. Peterson et al., Nucl. Fusion 41 (2001) 519.

[4] K. Yamazaki and T. Amano, Nucl. Fusion 32, 633 (1992).

[5] M.Z. Tokar et al., Physics of Plasmas 7 (2000) 4357.

Recent Issues of NIFS Series

NIFS-683 K. Saito, R. Kumazawa, T. Mutoh, T. Seki, T. Watari, Y. Torii, D.A. Hartmann, Y. Zhao, A. Fukuyama, F. Shimpo, G. Nomura, M. Yokota, M. Sasao, M. Isobe, M. Osakabe, T. Ozaki, K. Narihara, Y. Nagayama, S. Inagaki, K. Itoh, S. Morita, A.V. Krasilnikov, K. Ohkubo, M. Sato, S. Kubo, T. Shimozuma, H. Idei, Y. Yoshimura, O. Kaneko, Y. Takeiri, Y. Oka, K. Tsumori, K. Ikeda, A. Komori, H. Yamada, H. Funaba, K.Y. Watanabe, S. Sakakibara, M. Shoji, R. Sakamoto, J. Miyazawa, K. Tanaka, B.J. Peterson, N. Ashikawa, S. Murakami, T. Minami, S. Ohakachi, S. Yamamoto, S. Kado, H. Sasao, H. Suzuki, K. Kawahata, P. deVries, M. Emoto, H. Nakanishi, T. Kobuchi, N. Inoue, N. Ohyabu, Y. Nakamura, S. Masuzaki, S. Muto, K. Sato, T. Morisaki, M. Yokoyama, T. Watanabe, M. Goto, I. Yamada, K. Ida T. Tokuzawa, , N. Noda, S. Yamaguchi, K. Akaishi, A. Sagara, K. Toi, K. Nishimura, K. Yamazaki, S. Sudo Y. Hamada, O. Motojima, M. Fujiwara,
Ion and Electron Heating in ICRF Heating Experiments on LHD: Mar. 2001

NIFS-684 S. Kida and S. Goto,
Line Statistics:Stretching Rate of Passive Lines in Turbulence: Mar. 2001

NIFS-685 R. Tanaka, T. Nakamura and T. Yabe,
Exactly Conservative Semi-Lagrangian Scheme (CIP-CSL) in One-Dimension : Mar. 2001

NIFS-686 S. Toda and K. Itoh,
Analysis of Structure and Transition of Radial Electric Field in Helical Systems : Mar. 2001

NIFS-687 T. Kuroda and H. Sugama,
Effects of Multiple-Helicity Fields on Ion Temperature Gradient Modes: Apr. 2001

NIFS-688 M. Tanaka,
The Origins of Elctrical Resistivity in Magnetic Reconnection: Studies by 2D and 3D Macro Particle Simulations: Apr. 2001

NIFS-689 A. Maluckov, N. Nakajima, M. Okamoto, S. Murakami and R. Kanno,
Statistical Properties of the Neoclassical Radial Diffusion in a Tokamak Equilibrium: Apr. 2001

NIFS-690 Y. Matsumoto, T. Nagaura, Y. Itoh, S-I .Oikawa and T. Watanabe,
LHD Type Proton-Boron Reactor and the Control of its Peripheral Potential Structure: Apr. 2001

NIFS-691 A. Yoshizawa, S.-I. Itoh, K. Itoh and N. Yokoi,
Turbulence Theories and Modelling of Fluids and Plasmas: Apr. 2001

NIFS-692 K. Ichiguchi, T. Nishimura, N. Nakajima, M. Okamoto, S.-i. Oikawa, M. Itagaki,
Effects of Net Toroidal Current Profile on Mercier Criterion in Heliotron Plasma: Apr. 2001

NIFS-693 W. Pei, R. Horiuchi and T. Sato,
Long Time Scale Evolution of Collisionless Driven Reconnection in a Two-Dimensional Open System: Apr. 2001

NIFS-694 L.N. Vyachenslavov, K. Tanaka, K. Kawahata,
CO2 Laser Diagnostics for Measurements of the Plasma Density Profile and Plasma Density Fluctuations on LHD Apr. 2001

NIFS-695 T. Ohkawa,
Spin Dependent Transport in Magnetically Confined Plasma: May 2001

NIFS-696 M. Yokoyama, K. Ida, H. Sanuki, K. Itoh, K. Narihara, K. Tanaka, K. Kawahata, N. Ohyabu and LHD experimental group
Analysis of Radial Electric Field in LHD towards Improved Confinement: May 2001

NIFS-697 M. Yokoyama, K. Itoh, S. Okamura, K. Matsuoka, S. -I. Itoh,
Maximum-J Capability in a Quasi-Axisymmetric Stellarator: May 2001

NIFS-698 S-I. Itoh and K. Itoh,
Transition in Multiple-scale-lengths Turbulence in Plasmas: May 2001

NIFS-699 K. Ohi, H. Naitou, Y. Tauchi, O. Fukumasa,
Bifurcation in Asymmetric Plasma Divided by a Magnetic Filter: May 2001

NIFS-700 H. Miura, T. Hayashi and T. Sato,
Nonlinear Simulation of Resistive Ballooning Modes in Large Helical Device: June 2001

NIFS-701 G. Kawahara and S. Kida,
A Periodic Motion Embedded in Plane Couette Turbulence: June 2001

NIFS-702 K. Ohkubo,
Hybrid Modes in a Square Corrugated Waveguide: June 2001

NIFS-703 S.-I. Itoh and K. Itoh,
Statistical Theory and Transition in Multiple-scale-lengths Turbulence in Plasmas: June 2001

NIFS-704 S. Toda and K. Itoh,
Theoretical Study of Structure of Electric Field in Helical Toroidal Plasmas: June 2001

NIFS-705 K. Itoh and S-I. Itoh,
Geometry Changes Transient Transport in Plasmas: June 2001

NIFS-706 M. Tanaka and A. Yu. Grosberg
Electrophoresis of Charge Inverted Macroion Complex: Molecular Dynamics Study: July 2001

NIFS-707 T-H Watanave, H. Sugama and T. Sato
A Nondissipative Simulation Method for the Drift Kinetic Equation: July 2001

NIFS-708 N. Ishihara and S. Kida,
Dynamo Mechanism in a Rotating Spherical Shell: Competition between Magnetic Field and Convection Vortices July 2001

NIFS-709 LHD Experimental Group,
Contributions to 28th European Physical Society Conference on Controlled Fusion and Plasma Physics (Madeira Tecnopolo, Funchal, Portugal, 18-22 June 2001) from LHD Experiment: July 2001